A Study on Lateral Displacement Behavior of Buried Pipe in Liquefied Soil

Ono, Kohei

(Degree)
博士（農学）

(Date of Degree)
2017-09-25

(Date of Publication)
2018-09-01

(Resource Type)
doctoral thesis

(Report Number)
甲第6990号

(URL)
https://hdl.handle.net/20.500.14094/D1006990

Doctoral Dissertation

A Study on Lateral Displacement Behavior of Buried Pipe in Liquefied Soil

液状化地盤内における埋設管の水平変位挙動に関する研究

July 2017

Graduate School of Agricultural Science,

Kobe University

Kohei ONO

The research reported in this dissertation was conducted at the Laboratory of Geotechnical Engineering for Agriculture, Field of Agricultural Engineering and Socio-Economics, Graduate School of Agricultural Science, Kobe University, Japan.

Acknowledgements

First of all, the author would like to express his heartfelt gratitude to Dr. Toshinori Kawabata, Professor of Graduate School of Agricultural Science, Kobe University, for his thoughtful guidance and encouragement. He has supported the author from the very beginning of his college life. He taught the author the foundations of study. He got quite a lot of opportunities and assistance over the last eight years. Dr. Kawabata has made him what he is today.

The author wishes to acknowledge to one of the members of his Dissertation Committee, Dr. Tsutomu Tanaka, Professor of Graduate School of Agricultural Science, Kobe University, for his reviews and invaluable comments for his dissertation. He wishes to extend his grateful thanks to the remaining member of his Dissertation Committee, Dr. Kazuya Inoue, Associate Professor of Graduate School of Agricultural Science, Kobe University, for his invaluable advice and encouragement.

He wishes to express his appreciation to Dr. Yutaka Sawada, Assistant Professor of Graduate School of Agricultural Science, Kobe University. The author has received much research guidance since the graduate school. He gained courage from his enthusiasm for research. He was also supported in many aspects other than research.

His thanks extend to Dr. Kazunori Uchida, Professor and Executive Vice President of Kobe University, for his warm encouragement words.

His sincere appreciation will go to Dr. Yoshiyuki Mohri, Professor of College of Agriculture, Ibaraki University, and Mr. Mitsuru Ariyoshi, researcher of NARO Institute for Rural Engineering. He has received a lot of their cooperation in collaborative research many times since he was an undergraduate student.

The author would like to express his gratitude to Dr. Takashi Kimata and Dr. Yosuke Kudo, Associate professor and Assistant Professor of Graduate School of Life and Environmental Sciences, Osaka Prefecture University. He got a lot of valuable advice from them through many seminars jointly held with Kobe University.

He would like to express his sincere gratitude to Dr. Akira Murakami and Dr. Kazunori

Fujisawa, Professor and Associate Professor of Graduate School of Agriculture, Kyoto University. They invited me to lecture on continuum mechanics at Kyoto University. They expanded the author's academic view.

The author wishes to extend his thanks to Dr. Mitsu Okamura, Professor of Graduate School of Science and Engineering, Ehime University, for his sincere consideration. He has also given the author a lot of inspiration of study on liquefaction.

He would like to express his appreciation to Dr. Yoshinori Itani, Kubota Corporation. He gave me great advices on how to proceed with this study. He also got a lot of support outside the laboratory.

The author's thanks extend to Dr. Johji Hinobayashi, Dainippon Plastics, Inc., for his support since the author was undergraduate. He wishes to express his appreciations for valuable experience in field experiments in Hokkaido.

He appreciates having opportunity to meet Dr. Hoe I. Ling and Dr. Liming Li, Professor and Associate Research Scientist of Department of Civil Engineering and Engineering Mechanics, Columbia University. He is deeply thankful for the collaborative research in New York during his master's course. This valuable experience in the foreign country had a positive influence on his academic life.

He would like to thank Dr. Mariko Suzuki, Assistant Professor of Department of Civil Engineering, National Institute of Technology, Kagawa College. As a senior in the same laboratory, she taught me many things for four years. Even now, he is instructed as a member of the same Shikoku branch.

His appreciations extend to Dr. Akira Izumi, researcher of NARO Institute for Rural Engineering. The author got a lot of support from him as a senior of his laboratory. He deeply respects his positive attitude and energy.

Special thanks are due to the laboratory members who spend the same time during his doctoral course. He is deeply grateful for their support from Mr. Taiki Miki, Mr. Kazuki Murai, Mr. Seita Kobayashi, Mr. Sho Takahara, Ms. Yu Yokota, Mr. Naoki Takegawa, Mr. Kenji Terada, Mr. Zenko Ueda, Mr. Rintaro Shigemoto, Mr. Takuya Ishikawa, Ms. Yoko Ohta, Ms. Yuka Horio, Mr. Riku Maki, and Mr. Noritake Miyazaki. His appreciations extend to all other teachers, seniors, and friends who have supported him.

Finally, the author wishes to express his profound gratitude to his parents, for their warm encouragement, trust, and support.

Contents

List of Tables

List of Figures

Notations

Chapter 3

i	Hydraulic gradient
K	Coefficient of subgrade reaction (kN/m^3)
P	Lateral resistive force (N)
δ	Lateral displacement (m)
A	Lateral projected area of pipe (m^2)
i_{cr}	Critical hydraulic gradient
G_s	Specific gravity of sand particle
e	Void ratio
I_r	Increment rate (%)

Chapter 4

P_t	Thrust force (kN)
P_w	Internal water pressure (kN/m^2)
A_c	Cross-sectional area of pipe (m^2)
θ	Angle of pipe bend (^{o})
R_e	Reynolds number
ρ	Density of saturated sand (kg/m^3)
V	Velocity of pipe (m/s)
D	Diameter of pipe (m)
η	Coefficient of viscosity (kPa s)
C_D	Drag coefficient
L	Length of pipe (m)
R_H	Resultant force of passive earth pressure behind pipe (kN)
K_p	Coefficient of passive earth pressure
B_p	Width of back side of pipe (m)
H_1	Depth to crown of pipe (m)

H_2 Depth to bottom of pipe (m)

Chapter 5

m Mass of element (kg)

u Relative displacement between both elements (m)

k_n Normal spring coefficient (N/m)

k_s Tangential spring coefficient (N/m)

c_n Normal viscosity coefficient (Pa s)

c_s Tangential viscosity coefficient (Pa s)

g Gravitational acceleration (m/s^2)

F Summation of external force (N)

N Total number of contact points

f^j Contact force of j-th element (N)

I_{zz} Moment of inertia in x-y plane (kg m^2)

ω Rotational velocity around center of element (rad/s)

L_z Summation of the moment by the external force from element surface (kg m^2)

l^j Vector component heading from the center of the element to the j-th contact point

δ_n Displacement in normal direction at contact point in local coordinate system (m)

δ_s Displacement in tangential direction at contact point in local coordinate system (m)

Δt Time step (s)

$\Delta v^{(i,j)}$ Pore volume change in cell (m^2)

$\Delta x^{(k)}$ Lateral displacement of k-th particle (m)

$v^{(k)}$ Volume of k-th particle (m^2)

$\Delta h^{(i,j)}$ Pore water pressure in cell (m)

$\Delta v^{(i,j)}$ Variation of pore volume in cell (m^2)

$S^{(i,j)}$ Storage coefficient of fluid (m^{-1})

dx Width of each cell (m)

dy Height of each cell (m)

$B_x^{(i,j)}$ Body force in x direction (N)

$B_y^{(i,j)}$ Body force in y direction (N)

γ_w Unit weight of water (N/m^2)

Q_k Volume of fluid entering into cell (m^2/s)

$h^{(i,j:t+\Delta t)}$ Pore water pressure at time $t+\Delta t$ (m).

k_1 Hydraulic conductivity in x direction (m/s)

$h^{(i,j:t')}$ Pore water pressure at time t' (m)

Chapter 6

P_u Ultimate lateral resistive force (kN)

Y Lateral displacement (m)

Y_u Ultimate lateral displacement (m)

a Hyperbolic parameter

b Hyperbolic parameter

H' Depth to center of pipe (m)

γ' Submerged unit weight of soil considering excess pore water pressure ratio (kN/m^3)

γ'_0 Initial submerged unit weight of soil (kN/m^3)

Δu Increment of excess pore water pressure (kN/m^2)

z Depth from ground surface (m)

E_j Elongation of joint (m)

L_s Length of straight pipe (m)

φ Bending angle of joint (^{o})

E_{max} Maximum elongation of joint (m)

Y_{max} Allowable lateral displacement of pipe bend (m)

CHAPTER 1

Chapter 1

Introduction

1.1 Background

1.1.1 Agricultural pipeline

Agricultural channels play a vital role in supplying a great amount of water to farmlands. In Japan, water consumption for agriculture is approximately 54.4 billion cubic meters on the basis of the intake volume; roughly equal to two-thirds of the total water consumption (M.L.I.T.T., 2014). The length of main agricultural and drainage channels extends approximately 49,900 km, and the total length involving distal channels reaches more than 400,000 km (M.A.F.F., 2012).

As shown in **Figure 1.1**, Japanese agricultural channels mainly consist of open channels and pipelines; approximately 30% (13,578 km) of the channels is pipelines. In comparison with conventional open channels, pipelines have several advantages: the flow loss during water supply is smaller, the efficiency of water supply is superior, and the management of water supply is easier. Furthermore, several accessory effects such as improvement of water quality, efficient development of the ground surface, and prevention of the drowning accident are expected. From these advantages, the length of the pipeline is gradually increasing year by year as one of the major channels since 1960s.

Agricultural pipelines often laid along complicated geography from water sources to agricultural fields, involving a variety of bends and branches. Due to the topographical undulations, irrigation water is supplied efficiently by pressurization. The internal pressure sometimes exceeds 3.0 MPa, and it gives an external force called a thrust force to a pipe bend according to its angle. The thrust force is one of the main factors that greatly influence the

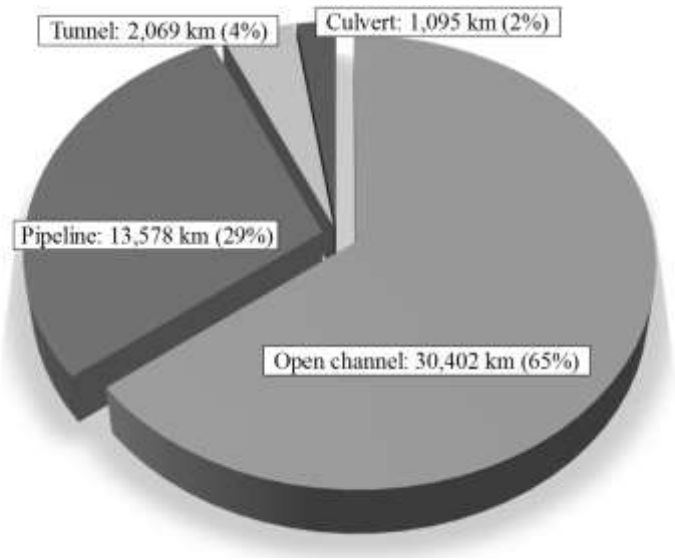

Figure 1.1 Stock of main agricultural channels

stability of the buried pipelines. Compared with waterworks that has already been developed, the working condition of agricultural pipelines is more severe. The diameter of the agricultural pipelines is larger (sometimes over 3,000 mm) and the water-supply pressure is quite higher. Furthermore, agricultural pipelines repeat the water-full and empty conditions according to the irrigation season. Due to increase in water demand in addition to these situations, further enhancement of structural design guidelines has been demanded.

1.1.2 Seismic damage of buried pipeline

Same as other civil engineering structures, seismic damage is a serious problem for buried pipelines. In particular, we cannot avoid taking countermeasures against earthquake because Japan is one of the most earthquake-prone countries in the world. In the 1964 Niigata Earthquake and Alaska Earthquake, extensive damage due to the liquefaction phenomenon was observed over a wide range, and the stability problems of the underground structures against liquefaction began to be noticed. Since these earthquakes, survey research for seismic and liquefaction damages of buried pipelines has been reported around the world. Several reports of the past are summarized as follows.

Toyoshima et al. (1984) investigated the seismic damages of the agricultural channels by the 1983 Nihonkai Chubu Earthquake in Noshiro area in Akita. They found the evidence of

Figure 1.2 Detachment of pipe bend by the 1993 Southwest-off Hokkaido Earthquake (Mohri et al., 1995)

the liquefaction of backfills and the water leakage from the joints, and revealed that the damages were concentrated on the change field of the strata. On the basis of the research, the authors mentioned the importance of prevention of liquefaction. Mohri (1985) also detailed the pipelines damaged by the same earthquake. They reported that a concrete block attached to 53 degrees pipe bend moved backward by approximately 0.4 m. Also in the 1989 Loma Prieta Earthquake, soil liquefaction and significant ground deformation were observed in San Francisco. O'Rourke and Gowdy (1991) examined the distribution of pipeline-system damage, and illustrated how the natural site conditions and artificial fills contributed to soil liquefaction and buried pipeline damage. Mohri et al. (1995) investigated the seismic damages of pipelines caused by the 1993 Southwest-off Hokkaido Earthquake. The authors revealed that one particular pipe bend moved backwards by 0.6 ~ 0.8 m because of liquefaction and action of thrust force (see **Figure 1.2**). In the 1995 Southern Hyogo Prefecture Earthquake, many buried pipelines received serious damages due to the lateral flow of liquefied soil, and the risk assessment of the lateral flow of the soil was closed up. Hamada et al. (1996) examined the relationship between the damage levels of the waterworks and the occurrence of the lateral flow according to the ground strain calculated from the lateral displacement vector obtained by aerial photogrammetry. Investigations conducted by Ariyoshi et al. (2012) and Mohri et al. (2014) of the damage caused by the 2011 off the Pacific coast of Tōhoku

Earthquake reported large displacement of pipelines and many joint separations caused by liquefaction. The above overview clearly indicate that liquefaction of backfills and movement of pipe bends are keywords of the seismic damage of the buried pipelines.

1.1.3 Seismic design of agricultural pipeline

The Ministry of Agriculture, Forestry, and Fisheries of Japan (MAFF) analyzed the causes and characteristics of the seismic damage of buried pipelines in the "Design Guideline for Agricultural Pipelines (MAFF, 2009)". **Table 1.1** summarizes the total six causes and five characteristics of the seismic damages. Note that these distinctive damages are prominent in the area where the seismic intensity is 5.0 or more. The water leakage due to detachment of a joint causes a secondary damage such as the ground run off.

On the basis of the above summary, MAFF further elaborates the summary of the seismic weak points of buried pipelines in the design guideline. More detailed classification is carried out on the seismic weak points based on the following four factors: topographical

Table 1.1 Cause and characteristic of seismic damage of pipeline

Cause
1. Seismic wave propagation
2. Liquefaction of natural soil or backfill sand
3. Settlement of soil due to consolidation
4. Sliding failure of embankment
5. Proximity structure and accessory structure
6. Fault
Characteristic
1. Detachment of joint at connection part with accessory facility
2. Detachment of joint at boundary where topography or geology change
3. Deformation of pipe due to liquefaction of backfill
4. Displacement of pipe due to sliding failure
5. Detachment of joint at periphery of structure installed at corner of slope

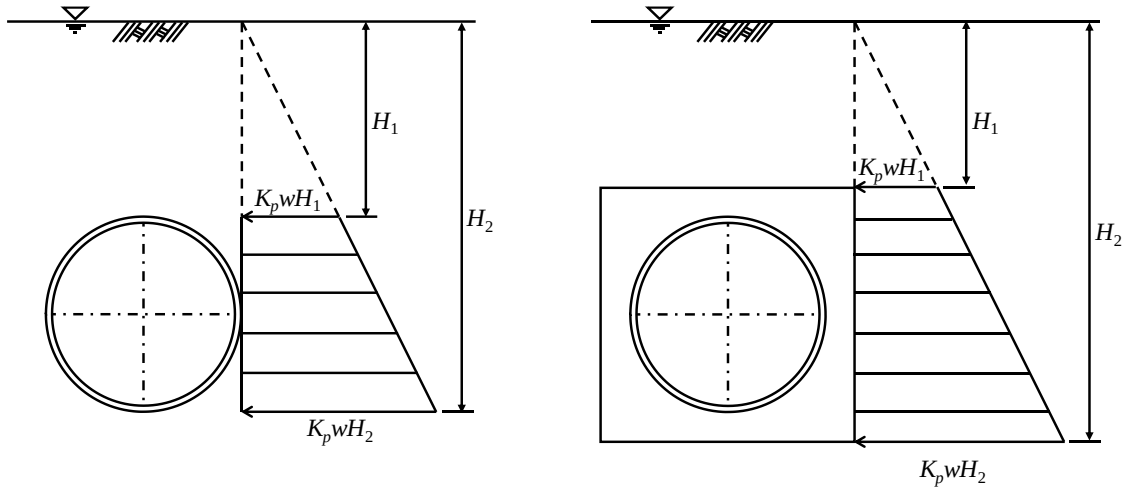

(a) (b)

Figure 1.3 Passive earth pressure acting on (a) pipe and (b) concrete block

factors, structural factors, construction factors, and soil factors. In particular, according to the damage surveys in the 2011 Tōhoku Earthquake, it was revealed that the structural and soil factors occupied the most of the causes of the seismic damages.

Structural factors mainly indicate connection parts of the pipe with accessory structures, pipe bends, and deformed fittings. In a pressurized pipe bend subjected to the thrust force, the joints of the pipe bend are inevitably weak against earthquake motion because of the difference of the inertia force. In the present design guideline, the necessity of the installation of the countermeasure structure for those parts is judged from the ratio (safety factor) of the thrust force to the resistive force acting on the pipe. As shown in **Figure 1.3**, the resistive force is the resultant of the Rankin's passive earth pressure acting on behind the pipe. When the resistive force (earth pressure) is judged as insufficient, the guideline proposes to secure the passive earth pressure by installing the concrete block (hereinafter, thrust block) around the pipeline. However, this countermeasure structure does not take into account the influence of the inertia force mentioned above. Furthermore, this simple method calculated from Rankin's earth pressure is not rational because the design does not take into account the variations in the earth pressure by the displacement of the pipe.

Secondly, there are various soil factors that lead to liquefaction of the backfill. Floating and displacement of pipelines because of liquefaction give excessive bending stress on the joint. Furthermore, the passive earth pressure that should resist the thrust force also

decreases considerably due to liquefaction. The above facts imply that the seismic damage of the buried pipeline has occurred by a combination of these structural and soil factors. On the other hand, the current guidelines do propose some countermeasures against liquefaction that are not related to thrust restraint. These countermeasures can be divided into two groups: measures to enhance the soil strength against liquefaction (e.g. compaction control or suppression of excess pore water pressure) or those to remodel the pipeline structure (e.g. use of flexible joints). However, since it is clear that the behavior of a buried pipeline subjected to an external force is determined by complex soil-pipe interactions, the displacement behavior of the pipe and the liquefaction of the backfill need to be considered simultaneously.

1.2 Aim of Study

Although many problems concerning the stability of buried pipelines are cited, the effective countermeasure has not been proposed yet. On the contrary, uneconomical structural designs due to excessive design philosophy are scattered. In order to solve these problems, the following three aims of study were set.

Elucidation of displacement characteristic of buried pipe under various effective stress

First, it is crucial to elucidate the fundamental displacement characteristics of buried pipes during liquefaction. Since the behavior of buried pipelines is determined by the complicated interaction with the surrounding soil, we should pay attention to its ground strength that varies depending on the effective stress conditions. To examine this interaction, a series of model experiments, image analysis, and numerical analysis are carried out.

Prediction of lateral displacement of buried pipe subjected to external force

The relative displacement between the pipe and its surrounding soil caused by the thrust force leads to the separation of joints. Therefore, only by predicting this relative displacement, we can discuss the stability of the buried pipeline. In particular, there is no established method for predicting the lateral displacement of the pipe during liquefaction, which is an indispensable task to judge the necessity of countermeasures. This study aims to

formulate the force-displacement relationship of the buried pipe.

Examination of effective thrust countermeasure during liquefaction

The current design guideline recommends the installation of a thrust block when the passive earth pressure against thrust force is insufficient. However, we cannot ignore the influence of the inertia force acting on the thrust block due to the earthquake motion, and its effectiveness during liquefaction has also not been examined. Therefore, the present study verifies the effectiveness of a thrust restraint method using gravel and geogrid as an alternative method that is effective during liquefaction. This countermeasure is intended to suppress liquefaction of the backfill by substituted with gravel and to increase the passive earth pressure by integrating with geogrid.

1.3 Overview of Thesis

This thesis is organized into following seven chapters. Chapter 1 briefly introduces the outline of agricultural pipelines, their seismic damages, and the present design guideline. This chapter also describes the aim of the study. Chapter 2 reviews the previous literatures. The studies concerning the lateral displacement behavior of buried pipes are mainly introduced. Several studies on various countermeasures related to earthquake resistance of buried pipes are also summarized. Chapter 3 describes the small-scale model experiments. The fundamental knowledge on the displacement characteristics of the buried pipe during liquefaction is collected by means of lateral loading experiments. Chapter 4 treats the middle-scale lateral loading experiments. A soil bed with various effective stress is prepared using a similar experimental method as shown in Chapter 3, and lateral load is applied to a model pipe under either displacement or load control. From the various viewpoints, the interaction between the movement of the pipe and the liquefied soil is examined. Furthermore, applicability of thrust restraint using gravel and geogrid during liquefaction is verified. In Chapter 5, two-dimensional discrete element method (DEM) analyses are presented. To simulate the model experiments shown in Chapter 4, fluid coupled-DEM analyses considering the pore water pressure is performed. In Chapter 6, a concept of design method is proposed

regarding the stability of the buried pipelines subjected to lateral load. Finally, Chapter 7 summarizes this thesis and describes the perspectives of the study.

References

Ariyoshi, M., Mohri, Y., Asano, I. and Ueno, K. 2012. Damage and Restoration of Agricultural Pipeline at Kumadogawa Irrigation Project by the 2011 off the Pacific coast of Tohoku Earthquake, *Technical report in NIRE*, 213, 201-215. (in Japanese).

Hamada, M., Isoyama, R., and Wakamatsu, K. 1996. Liquefaction-Induced Ground Displacement and Its Related Damage to Lifeline Facilities, *Special issue of soils and foundations*, 81-89.

Ministry of Agriculture, Forestry and Fisheries of Japan (MAFF). 2009. Planning and Design Criteria of Land Improvement Project (Pipeline), JSIDRE, 321-409. (in Japanese).

Ministry of Agriculture, Forestry and Fisheries of Japan (MAFF). 2012. (Reference in 2017.4.1), Maintenance conditions of agricultural production base ver. 2013, (online), < http://www.maff.go.jp/j/council/seisaku/nousin/bukai/h24_4/pdf/ref-data4.pdf > (in Japanese).

Ministry of Land, Infrastructure, Transport and Tourism (MLITT). 2014. (Reference in 2017.4.1), Water Resources in Japan ver. 2013, (online), < http://www.mlit.go.jp/common/001006494.pdf > (in Japanese).

Mohri. Y. 1985. Report on the damage of pipelines by the 1983 Nihonkai Chubu Earthquake, *Technical report in NIRE*, 4, 93-147. (in Japanese).

Mohri, Y., Yasunaka, M. and Tani, S. 1995. Damage to Buried Pipeline due to Liquefaction Induced Performance at the Ground by the Hokkaido-Nansei-Oki Earthquake in 1993, *Proceedings of 1st International Conference on Earthquake Geotechnical Engineering*, 31-36.

Mohri, Y., Masukawa, S., Hori, T. and Ariyoshi, M. 2014. Damage to Agricultural Facilities, *Soils and Foundations*, 54(4), 588-607.

O'Rourke, T. D. and Gowdy, T. E. 1991. Lifeline and Geotechnical Aspects of the 1989 Loma Prieta Earthquake, *Proceedings of 2nd International Conference on Recent Advances in Geotechnical Earthquake Engineering and Soil Dynamics*, LP04, 1601-1612.

Toyoshima, K., Akutsu, H., Noro, T., and Ishido, T. 1984. Damage of pipelines caused by the 1983 Nihonkai Chubu Earthquake and its restoration, *Journal of the Agricultural Engineering Society*, 52-6, 23-28. (in Japanese).

CHAPTER 2

Chapter 2

Literature Review

2.1 Introduction

The study field of buried pipelines is very diverse. The structure, the material, and the size of the pipeline are various, and external environment such as the burial condition, the land use on the ground surface, and the construction method largely influence the stability of pipelines. For revealing the phenomenon at each site, it is crucial to identify its essence and to reproduce specific condition in response to the site. Meanwhile, it is indispensable to outline the past studies deeply related to the present study for understanding the essence of the study.

This chapter firstly introduces a number of experimental and analytical studies on lateral displacement behavior of underground structures. This review distinguishes the studies on buried pipes carried out in dry soil and in liquefied soil. The studies for buried anchor plates are also introduced because its mechanical behavior is similar to that of pipes. Subsequently, several studies on various countermeasures for buried pipes concerning earthquake, liquefaction, and thrust force are introduced.

2.2 Lateral Displacement Behavior of Underground Structure

2.2.1 In dry and unsaturated soil

Regarding the relationship between the resistive force and the displacement of buried pipelines or anchor plates, many experimental studies have been conducted. Many of them were carried out for the purpose of predicting the displacement of structures subjected to the external force. By setting several parameters: the ground density, the burial depth, and the size

and shape of the structures, past studies discussed the relationship quantitatively. Furthermore, non-linear approximation was performed on the force-displacement curve to propose prediction equations of the resistive force.

The earliest experimental works on the lateral displacement behavior of the underground structures are the studies by Hansen (1961) and Ovesen (1964). Hansen carried out total 26 model experiments on wooden piles in dry sand to determine their resistive force against lateral loads. The author showed the very beneficial relationship between the bearing capacity factor, the burial depth, and the internal frictional angles. Ovesen also examined the parameters that influenced the resistive force of anchor plates. Finally, the author proposed the reliable calculation method of the resistive force. Das (1975) measured the pullout force of the vertical anchors by a series of model experiments. The author expressed the maximum force by exponential function with the burial depth, the size, and the shape (square or circular) of the anchor. Das et al. (1977) subsequently defined the dimensionless force and compared with the one suggested by Ovesen (1964). The authors pointed out that there was about 25% difference of the resistive force between the experiment and the theory for a deep anchor plate in dense sand. Audibert and Nyman (1977) conducted lateral loading experiments on pipes in dry sand. The authors obtained the ultimate displacement of the pipe empirically by changing the soil density and the burial depth. They proposed a bilinear expression method on the force-displacement curve in addition to a hyperbolic approximation. On the basis of laboratory scale experiments performed on laterally loaded vertical anchor plates in sand, Akinmusuru (1978) revealed that the shape and size of anchor plates largely influenced its pullout capacity. The author also photographed the two-typical movement patterns of surrounding soil, and indicated that the lateral behavior of an anchor changed depending on the burial depth from shallow to deep. Dickin and Leung (1983, 1985) conducted centrifugal tests to review the design methods for vertical anchor plates subjected to the lateral pullout forces in prototype-scale. They pointed out that a lack of consistent agreement between model tests and centrifugal tests attributed to inherent difficulties in obtaining reliable data for small model at low stress levels. Trautmann and O'Rourke (1985) examined the displacement of the pipe subjected to lateral load under total 30 conditions. By changing the soil density, the burial depth, and the surface roughness, they obtained the ultimate displacement. The authors

established an empirical formula regarding the relationship between the ultimate displacement and the burial depth. Das et al. (1985) measured the lateral resistive force of the cohesive soil by applying the lateral load to a vertical anchor plate in clayey soil. The authors formulated the maximum lateral resistive force by exponential function. Hsu (1993) carried out a series of lateral loading tests for a buried pipe with focusing on the loading rate. The experimental results found the two-constant hyperbolic equation that have the power law relationship with the loading rate. Suemasa et al. (1998) showed the theoretical solutions of force-displacement curves for a pile or buried pipe loaded by lateral soil movements. These formulations based on CEM (Cavity Expansion Method) and SPN (Strain Path Method) were able to express the displacement behavior from initial elastic state to ultimate state, and took the appearance of the void behind the pipe into the account.

Meanwhile, in recent years, numerical analysis methods: Finite Element Method (FEM) and Discrete Element Method (DEM) have been developed and are being used for the displacement problems with the development of processing capability of computers. Yimsiri et al (2004) carried out the FE analysis for large-scale model tests by Trautmann and O'Rourke (1983) in the two soil models with input parameters determined from laboratory element tests. The FE results showed reasonably well fitting with the experimental data for medium and dense sands. On the basis of the FE analysis, they summarized a design chart of the peak dimensionless forces against burial depth for soil with different frictional angles. Guo and Stolle (2015) investigated the pipe-soil interaction by means of FE analysis when subjected to lateral soil movement. The systematical study focusing on the scale-effects, the stress level, the burial depth, and the soil properties revealed that the effects of the pipe size and the burial depth must be taken into account to properly estimate the maximum resistive force. Yimsiri and Soga (2006) investigated the soil-pipeline interactions under lateral and upward pipe movements in sand using DEM. They compared the results of DEM with FEM results and confirmed that the advantage of DEM over FEM was its ability to simulate large movement of soil around the pipe. The DEM analysis continued with unlimited pipe movement until it reached ultimate force, whereas the FEM often stop due to a large distortion of the mesh before reaching the ultimate force. Kouretzis et al. (2013) devised a large-deformation numerical methodology for simulating the interaction effects for a pipeline

installed in a trench backfilled with loosely deposited dry sand. The authors compared their numerical results with the experimental results by Trautmann and O'Rourke (1985) and Yimsiri et al. (2004), and suggested that the parameters expressing the critical-state shear strength of dry sand were sufficient for describing the failure mode of the pipeline-backfill system. Roy et al. (2015) also carried out FE analyses for pipelines buried in dense sand subjected to lateral ground displacement by using the MMC model (Modified Mohr-Coulomb). The FE model devised by the authors considered a pre- and post-peak behavior with a smooth transition and the variation of the angle of the internal friction and dilation angle. The FE analysis showed better simulation of the force-displacement response for a wide range of lateral displacement of the pipe for different burial depth.

2.2.2 In liquefied soil

In comparison with a series of studies carried out for dry sand, there have been relatively few studies of the dynamic behavior of buried pipes and vertical anchor plates in liquefied soil. Due to the geographical characteristics, many of the studies have been conducted in Japan. Studies of pipeline-liquefied-soil interaction are categorized generally into two groups: those that focus on vertical displacement (floating) or those that focus on lateral displacement by the thrust force or the lateral ground flow. The experimental method that reproduces liquefaction of soil bed is also classified into two: a method using a shaking table or a method using boiling phenomenon.

Regarding lateral displacement behavior, Yasuda et al. (1987) experimentally examined the reduction rate of the resistive force of the buried pipe in the liquefied sand. The authors pointed out that the reduction rate obtained from the boiling tests was smaller than that from the shaking table tests due to the non-homogeneity of the liquefied soil bed. Kiku et al. (1989) investigated the lateral resistive force of the liquefied sand during pipe movement by means of the shaking table tests. They controlled the liquefaction levels by adjusting the excess pore water pressure ratio, and revealed that the resistive force varied depending on the liquefaction levels. Suzuki et al. (1993) also carried out model experiments to measure the resistive force of the pipe during liquefaction. The authors expressed the loading rate-resistive

force relationships of the flexible pipes. Miyajima and Kitaura (1994) investigated the response of a model pipe subjected to the lateral ground flow through shaking table tests. The authors determined the viscous coefficient of the liquefied soil and compared the bending moment of the pipe with that calculated by using the viscous coefficient. Ohtomo (1998) focused on the load characteristics of liquefaction-induced lateral ground flow on underground structures. The author firstly measured the relationships between the viscosity and Reynolds number in the liquefied soil from shaking table tests, and indicated that the liquefied soil was regarded as viscous fluid. Secondly, the author showed that the resistive force pf the lateral ground flow acting on underground structures could be estimated based on the viscosity. Towhata et al. (1999) also carried out shaking table tests to investigate the influence of lateral ground flow on a buried pipe. These showed that the lateral resistive force increased with the rate of pipe movement, from which the authors concluded that liquefied sand behaved as a viscous fluid. Morimitsu et al. (1999) verified the rate effect of the lateral ground flow on the horizontal subgrade reaction by means of shaking table tests. The test results revealed that the horizontal subgrade reaction between the liquefied soil and the underground structure had a strong rate dependence: the faster the relative velocity was, the greater horizontal subgrade reaction was measured due to the positive dilatancy. Zhang et al. (2002) constructed a bounding surface model to simulate the force–displacement response of an offshore pipe observed in centrifuge model tests. The model reproduced a gradual transition from elastic to plastic response and the strain-softening behavior of the pipe under lateral loading. Calvetti et al. (2004) investigated the pipeline–landslide interaction during liquefaction by means of model experiments and DEM analyses. The authors reproduced the effects of upward seepage artificially in DEM by reducing the acceleration due to gravity. They confirmed that the DEM model well simulated the decrease of the lateral resistive force. Dungca et al. (2006) examined the effect of loading rate on the lateral resistive force by applying lateral cyclic vibrations to a buried pipe. The test results showed that the strain of the resistance transformation point became larger as the loading rate becomes smaller. The authors mentioned that this tendency was not only be associated with the dilatancy characteristics of sand but also with the pore fluid migration around the cylinder. Itani et al. (2015a) conducted model experiments to discuss the behavior of the pipe bend laterally

loaded in the liquefied sand. The authors revealed that the displacement of the pipe increased during liquefaction, and the coefficient of subgrade reaction in the liquefied soil reduced to 1/7 to 1/8 compared to that in saturated sand.

2.3 Liquefaction Countermeasure and Thrust Restraint

2.3.1 Soil improvement

The current design guidelines for agricultural pipelines propose some countermeasures against liquefaction. Since it has already been revealed that liquefaction is caused by a sudden rise in excess pore water pressure, it is needless to say that methods of suppressing the rise of the excess pore water pressure or immediately dissipating the raised pressure are effective for preventing liquefaction. Many experimental studies about soil improvement have been conducted since 1990s to prevent floating of buried pipeline during liquefaction. Yoshida et al. (1993) verified the application of a gravel-drain system to buried pipes to mitigate their damage due to liquefaction. The system mitigated the increase in the excess pore water pressure ratio of the backfill surrounding the pipe, and reduced settlement of soil and floatation of the pipes. Yasuda et al. (1995) carried out a series of shaking table tests to study the effect of the permeability at the boundary between the trench and the surrounding soil on floatation of a buried pipe. The authors revealed that the buried pipe did not float because the excess pore water pressure induced in the backfill sand dissipated into the surrounding soil. Kobayashi et al. (1997) conducted shaking table tests for sewer pipes to examine the uplift displacement due to liquefaction. The uplift of the pipe was observed when only the lower part of the pipe was backfilled with gravel, while the pipe was not uplifted when backfilling the upper part of the pipe with gravel. Koseki et al. (1998) investigated the uplift behavior of sewer pipes caused by liquefaction of surrounding soil by a series of shaking table tests. The results showed that the pipes suffered sudden large uplift when the dissipation of the excess pore water pressure from the backfill soil to the original soil was prevented. On the contrary, the uplift of the pipes was reduced by backfilling the upper part with gravelly sand. Sato et al. (2000a, 2000b) carried out the shaking table tests for buried pipes subjected to lateral load by two-different methods: load control and displacement

control. Test results verified the effectiveness of the gravel-drain for the resistive force of the pipe during liquefaction. Ling et al. (2003) conducted a total of eight shaking table tests on the buried pipe under 30*g* gravitational field with focusing on the stability against floatation during liquefaction. The authors revealed that the deadweight and the stiffness of the gravel unit, which was confined by geosynthetic, were important items in a design. Otsubo et al. (2016a, 2016b) carried out a series of shaking table tests to investigate the performance of the recycled backfill material for mitigating the liquefaction-induced floating of sewer pipes. The test results showed that the examined materials were useful for mitigating the floatation of pipes irrespective of the liquefaction potential in the surrounding soil. The importance of balancing the unit weight of the backfills and the surrounding soils was highlighted for enhancing the safety when the surrounding soil was liquefiable.

2.3.2 Remodeling of pipeline structure

The method of remodeling the pipeline structure is one of the effective methods as a countermeasure for displacement of buried pipelines although this needs additional cost. Takada et al. (1999) carried out model tests to examine the behavior of earthquake-proof PVC pipeline subjected to uneven ground settlement. The experimental results showed that the sling of the joint mitigated the axial strain of the pipe. On the contrary, the axial strain greatly increased when the slip-out preventer of the joint worked well. Fujita et al. (2007) conducted model experiments to verify the performance of curved jointed pipelines. The authors compared the displacement of a pipe with new joints subjected to repeated internal water pressure with a bend pipe having the same bend angle. The test results indicated that the widen area receiving the earth pressure suppressed the displacement of the curved jointed pipe. Itani et al. (2015b) proposed chain-structure joints to decrease the displacement of the bend pipe subjected to the thrust force during liquefaction. The experimental results revealed that the displacement of the bend pipe decreased because the entire connected pipes followed the displacement of the pipe bend by the detachment-prevention structure. Itani et al. (2016) subsequently verified the dynamic behavior of the pipe bend with chain-structure joints with using shaking table. The authors confirmed the effectiveness of the joint structure in the

heavily liquefied sand bed.

2.3.3 Lightweight thrust restraint

Since thrust restraint using thrust blocks has a large risk for earthquake motion due to the difference of the inertia force, Kawabata et al. (2006) devised a lightweight thrust restraint that combinates geogrid and anchor plate. The results of lateral loading experiments indicated that the new method was significantly effective for enhancing the lateral resistance. For this method, Sawada et al. (2010) proposed the calculation method of the maximum lateral resistive force based on the force equilibrium on the failure surface. The authors formulated the increment of the lateral resistive force from the proposed method considering the tensile characteristics of geogrid, and suggested the design method for the lightweight thrust restraint. Finally, Kawabata et al. (2011) verified the effectiveness of the lightweight thrust restraint during liquefaction by shaking table tests on a model pipe with bends. The authors confirm that the lateral displacement of the bend with the new method decreased in comparison with the conventional thrust block.

References

Akinmusuru, J. O. 1978. Horizontally Loaded Vertical Plate Anchors in Sand, *Journal of the Geotechnical Engineering Division*, 104(2), 283-287.

Audibert, J. M. E. and Nyman, K. J. 1977. Soil Restraint against Horizontal Motion of Pipes, *Journal of the Geotechnical Engineering Division*, 103(10), 1119-1142.

Calvetti, F., Prisco, C. and Nova, R. 2004. Experimental and Numerical Analysis of Soil–Pipe Interaction, *Journal of Geotechnical and Geoenvironmental Engineering*, 130(12) 1292-1299.

Das, B. M. 1975. Pullout Resistance of Vertical Anchors, *Journal of the Geotechnical Engineering Division*, 101(7), 87-91.

Das, B. M., Seeley G. R., and Das, S. C. 1977. Ultimate Resistance of Deep Vertical Anchor in Sand, *Soils and Foundations*, 17(2), 53-56.

Das, B. M., Moreno, R., and Dallo, K. 1985. Ultimate Pullout Capacity of Shallow Vertical Anchors in Clay,

Soils and Foundations, 25(2), 148-152.

Dickin, E. A. and Leung, C. F. 1983. Centrifugal Model Tests on Vertical Anchor Plates, *Journal of Geotechnical Engineering*, 109(12), 1503-1525.

Dickin, E. A. and Leung, C. F. 1985. Evaluation of Design Methods for Vertical Anchor Plates, *Journal of Geotechnical Engineering*, 111(4), 500-520.

Dungca, J. R., Kuwano, J., Takahashi, A., Saruwatari, T., Izawa, J., Suzuki, H., and Tokimatsu, K. 2006. Shaking Table Tests on the Lateral Response of a Pile Buried in Liquefied Sand, *11th International Conference on Soil Dynamics and Earthquake Engineering*, 26(2-4), 287-295.

Fujita, N., Mohri, Y., and Suzuki, H. 2007. Performance of Flexible Joints Formed Underground Pipeline for Seismic Motion, *Transactions of JSIDRE*, 249, 63-73. (in Japanese with English summary).

Guo, P. J. and Stolle, D. F. E. 2005. Lateral Pipe–Soil Interaction in Sand with Reference to Scale Effect, *Journal of Geotechnical and Geoenvironmental Engineering*, 131(3), 338–349.

Hansen, J. B. 1961. The Ultimate Resistance of Rigid Piles Against Transversal Forces, *Bulletin 12*, Danish Geotechnical Institute, Copenhagen, Denmark, 5-9.

Hsu, T. W. 1993. Rate Effect on Lateral Soil Restraint of Pipelines, *Soils and Foundations*, 33(4), 159-169.

Itani, Y., Fujita, N., Sawada, Y., Ariyoshi, M., Mohri, Y., and Kawabata, T. 2015a. Model Experiment on the Horizontal Resistance Force of Buried Pipe in Liquefied Ground, *IDRE Journal*, 83(1), 77-83. (in Japanese with English summary).

Itani, Y., Fujita, N., Yokota, Y., Ariyoshi, M., Mohri, Y., and Kawabata, T. 2015b. Mechanical Behavior of Flexibly Jointed Pipeline with a Bend on Lateral Loading Tests, *IDRE Journal*, 83(6), 177-183. (in Japanese with English summary).

Itani, Y., Fujita, N., Ariyoshi, M., Mohri, Y., and Kawabata, T. 2016. Dynamic Behavior of Flexibly Jointed Pipeline with a Bend in Liquefied Ground, *IDRE Journal*, 84(1), 1-8. (in Japanese with English summary).

Kawabata, T., Sawada, Y., Mohri, Y., and Uchida, K. 2006. Verification of Effectiveness for Lightweight Thrust Restraint Method of Buried Bend and Mechanism of Lateral Resistance by Model Tests, *Transactions of the Japanese Society of Irrigation, Drainage and Reclamation Engineering*, 74(4), 581-587. (in Japanese with English summary).

Kawabata, T., Sawada, Y., Mohri, Y., and Ling, H. I. 2011. Dynamic Behavior of Buried Bend with Thrust Restraint in Liquefying Ground, *Journal of Japan Society of Civil Engineers*, Series C (Geosphere Engineering), 67(3), 399-406. (in Japanese with English summary).

Kiku, T., Yasuda, S., and Yoshida, G. 1989. Relationship Between Restraint Force against Buried Pipe and Degree of Liquefaction, *Proceedings of the JSCE earthquake engineering symposium*, 20, 277-280. (in Japanese).

Kobayashi, H., Tamura, K., and Ninomiya, Y. 1997. Shaking Table Tests on Floating of Sewer Pipelines with Different Backfill Material, *Proceedings of the JSCE earthquake engineering symposium*, 24, 501-504 (in Japanese).

Koseki, J., Matsuo, O., and Tanaka, S. 1998. Uplift of Sewer Pipes Caused by Earthquake-Induced Liquefaction of Surrounding Soil, *Soils and Foundations*, 38(3), 75-87.

Kouretzis, G. P., Sheng, D., and Sloan, S. W. 2013. Sand-Pipeline-Trench Lateral Interaction Effects for Shallow Buried pipelines, *Computers and Geotechnics*, 54, 53-59.

Ling, H. I., Mohri, Y., Kawabata, T., Liu, H., Burke, C., and Sun, L. 2003. Centrifuge Modeling of Seismic Behavior of Large-Diameter Pipe in Liquefiable Soil, *Journal of Geotechnical and Geoenvironmental Engineering*, 1092-1101.

Miyajima, M. and Kitaura, M. 1994. Experiments on Force Acting on Underground Structures in Liquefaction-Induced Ground Flow, *Proceedings of 5th US-Japan Workshop on Earthquake Resistant Design of Lifeline Facilities and Countermeasures against Soil Liquefaction*, 445-455.

Morimitsu, T., Tamura, K., Higashi, T., and Kobayashi, H. 1999. Experimental Study for Rate Dependence on Horizontal Subgrade Reaction in Liquefied Soil, *Proceedings of the JSCE earthquake engineering symposium*, 25, 377-380 (in Japanese).

Ohtomo, K. 1998. Load Characteristics of Ground Lateral Flow on In-Ground Structures, *Journal of JSCE*, 591, 283-297. (in Japanese with English summary).

Otsubo, M., Towhata, I., Hayashida, T., Shimura, M., Uchimura, T., Liu, B., Taeseri, D., Cauvin, B., and Rattez, H. 2016a. Shaking Table Tests on Mitigation of Liquefaction Vulnerability for Existing Embedded Lifelines, *Soils and Foundations*, 56(3), 348-364.

Otsubo, M., Towhata, I., Hayashida, T., Liu, B., and Goto, S. 2016b. Shaking Table Tests on Liquefaction Mitigation of Embedded Lifelines by Backfilling with Recycled Materials, *Soils and Foundations*, 56(3), 365-378.

Ovesen, N. K. 1964. Anchor Slab, Calculation Methods and Model Tests, *Bulletin 16*, Danish Geotechnical Institute, Copenhagen, Denmark, 5-39.

Roy, K., Hawlader, B., Kenny, S., and Moore, I. 2016. Finite Element Modeling of Lateral Pipeline–Soil

Interactions in Dense Sand, *Canadian Geotechnical Journal*, 53, 490-504.

Sato, H., Mohri, Y., and Kawabata, T. 2000a. Shaking Table Tests for Lateral Resistive Force of Buried Pipe in Liquefied Soil, *Proceedings of 35th Japan National Conference on Geotechnical Engineering*, 2147-2148. (in Japanese).

Sato, H., Kawabata, T., and Mohri, Y. 2000b. Countermeasure Methods and Seismic Motion of Pipe Subjected to Thrust Force, *Proceedings of H.12 Japan National Conference on JSIDRE,* 478-479. (in Japanese).

Sawada, Y., Kawabata, T., and Mohri, Y. 2010. Design for Lightweight Thrust Restraint of Pipe Bend, *Transactions of the Japanese Society of Irrigation, Drainage and Reclamation Engineering*, 78(1), 33-40. (in Japanese with English summary).

Suemasa, N., Katada, T., Hashimoto, O., and Nakamura, K. 1998, Non-Linear P-Y Spring Models of a Pile Loaded by Lateral Soil Movements, *Journal of Japan Society of Civil Engineers*, 603, 67-76. (in Japanese with English summary)

Suzuki, N., Yano, T., and Matsuyama, E. 1993. Deformation of Buried Pipeline by Lateral Ground Flow of Liquefied Soil, *Proceedings of the JSCE Earthquake Engineering Symposium*, 22, 663-666. (in Japanese).

Takada, S., Nakano, M., Katagiri, S., Tani, K., and Koyanagi, S. 1999. Experimental Study on Earthquake-Proof U-PVC Pipeline Subjected to Uneven Ground Settlement During Earthquakes, *Journal of JSCE*, 619, 145-154. (in Japanese with English summary).

Towhata, I., Vargas-Monge, W., Orense, R. P., and Yao, M. 1999. Shaking Table Tests on Subgrade Reaction of Pipe Embedded in Sandy Liquefied Subsoil, *Journal of Soil Dynamics and Earthquake Engineering*, 18(5), 347-361.

Trautmann, C. H. and O'Rourke, T. D. 1985. Lateral Force-Displacement Response of Buried Pipe, *Journal of the Geotechnical Engineering*, 111(9), 1077-1092.

Yasuda, S., Saito, K., and Suzuki N. 1987. Restraint Force of Liquefied Soil against Buried Pipe, *Proceedings of the JSCE Earthquake Engineering Symposium*, 19, 189-192. (in Japanese).

Yasuda, S., Nagase, H., Itafuji, S., Sawada, H., and Mine, K. 1995. A Study on the Mechanism of the Floatation of Buried Pipes due to Liquefaction, *Proceedings of the 7th International Conference on Soil Dynamics and Earthquake Engineering*, 125-132,

Yimsiri, S., Soga, K., Yoshizaki, K., Dasari, G. R., and O'Rourke T. D. 2004. Lateral and Upward Soil-Pipeline Interactions in Sand for Deep Embedment Conditions, *Journal of Geotechnical and Geoenvironmental Engineering,* 130(8), 830-842.

Yimsiri, S. and Soga, K. 2006. DEM Analysis of Soil-Pipeline Interaction in Sand under Lateral and Upward Movements at Deep Embedment, *Journal of Southeast Asian Geotechnical Society*, 37, 83-94.

Yoshida, M., Kitaura, M., Miyajima, M., and Oishi, H. 1993. Experimental Study on a Countermeasure against Liquefaction for Underground Pipelines using Gravel Drain System, *Journal of JSCE*, 459, 149-158. (in Japanese with English summary).

Zhang, J., Stewart, D. P., and Randolph, M. F. 2002. Modeling of Shallowly Embedded Offshore Pipelines in Calcareous Sand, *Journal of Geotechnical and Geoenvironmental Engineering*, 128(5), 363-371.

CHAPTER 3

The contents of this chapter are based on:

Ono, K., Yokota, Y., Itani, Y., Sawada, Y., and Kawabata, T. 2017. Influence of Hydraulic Gradient and Loading Rate on Lateral Resistance Force of Buried Pipe, *Transactions of JSIDRE*, 304(85-1), I_29-I-35. (in Japanese with English summary).

Ono, K., Yokota, Y., Sawada, Y., and Kawabata, T. 2016. Lateral Loading Test for Buried Pipe on Reinforcing Effect of Geogrid for Shear Resistance of Liquefied Soil, *Geosynthetics Engineering Journal*, 31, 261-268. (in Japanese with English summary).

Ono, K., Yokota, Y., Itani, Y., Sawada, Y., and Kawabata, T. 2016. Lateral Loading Experiment for Buried Pipe in Reinforced Ground with Geogrids under Different Hydraulic Gradient, *Proceedings of the 6th European Geosynthetics Congress*, 1322-1331.

Ono, K., Yokota, Y., Sawada, Y., and Kawabata, T. 2016. Lateral Loading Test for Buried Pipe under Different Hydraulic Gradient, *Proceedings of 26th International Ocean and Polar Engineering Conference*, 664-669.

Chapter 3

Characteristics of Resistive Force and Rate Dependence of Liquefied Sand

3.1 Introduction

In a pressurized pipe bend, a thrust force is generated that depends on the angle of the bend and the magnitude of the internal pressure. The lateral resistance to this thrust force is expected to come from the passive earth pressure behind the pipe bend. However, the current design only considers pipeline stability under normal conditions, which do not include a decrease of thrust restraint because of liquefaction.

This chapter describes small-scale model experiments that are performed to gather fundamental knowledge about characteristics of lateral displacement of a buried pipe during liquefaction. The mechanism of liquefaction due to seismic motion is generally understood as follows. First, the saturated sand subjected to cyclic shear stress causes volume shrinkage due to negative dilatancy. The pore water constrains the volume shrinkage, and this reaction reduces contact force between soil particles (effective stress). As this cycle is repeated, the excess pore water pressure gradually accumulates and eventually the effective stress reaches zero. The soil particles are in a state of floating in water, and the sand behaves as liquid.

In the present study, boiling tests are used instead of shaking table tests to reproduce liquefaction of sand. In boiling phenomenon, upward seepage is dominant instead of the movement of soil particles. Since the total stress of the soil is absolute that is determined only by the weight of sand and water, the effective stress decreases to zero as the excess pore water pressure that is raised by the upward seepage increases to the total stress. Although the

process in which the effective stress varies is completely different between both methods, the state in which the effective stress decreases to zero is considered to be essentially equivalent.

In the experiment, the lateral load is applied to a model pipe after the stress state of the soil bed is controlled to investigate the force–displacement relationship that depends on the effective stress of the soil. The influence of the loading rate of the pipe on the resistive force is also examined. Furthermore, the thrust restraint using gravel and geogrid is investigated to qualitatively verify its effectiveness in the saturated and liquefied soil.

3.2 Outline of Model Experiment

3.2.1 Equipment and materials

Experimental set-up

Figure 3.1 shows the schematic diagram of a test container. The inner dimensions of the container were 600 mm in width, 500 mm in height, and 200 mm in length. The wall of the container was made of acrylic glass to monitor the inside of the model. Total 14 pore pressure transducers were installed in the central cross-section at four different levels.

Sand

Silica sand was used for the backfill materials. **Figure 3.2** and **Table 3.1** show the particle size distribution and the physical properties of the silica sand, respectively. The sufficiently saturated soil bed was prepared by a water-pluviation technique. The properties of the soil bed are shown in **Table 3.2**.

To confirm the liquefaction strength of the soil bed, cyclic undrained triaxial tests (JGS-0541) were conducted in advance, for a specimen whose relative density was 40%. **Figure 3.3** shows the variation of the cyclic stress ratio with the number of cyclic loading at restraint pressure of 100 kPa. The cyclic stress ratio when the number of cyclic loading is 20 (SR_{20}) was approximately 0.19. According to the Japanese Design Guidelines for Agricultural Pipelines (M.A.F.F., 2009), the sandy soil keeps enough earthquake resistance when the degree of compaction is more than 95%, which is equal to the cyclic stress ratio of 0.4 and more. Judging from the above results, the liquefaction restraint of the present soil bed was

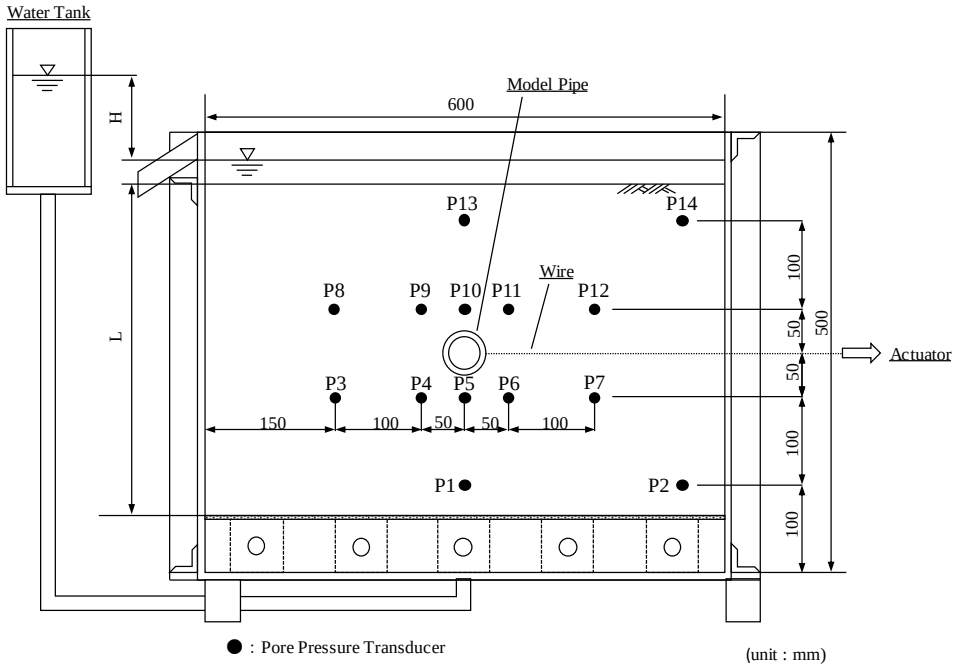

Figure 3.1 Cross section of test container

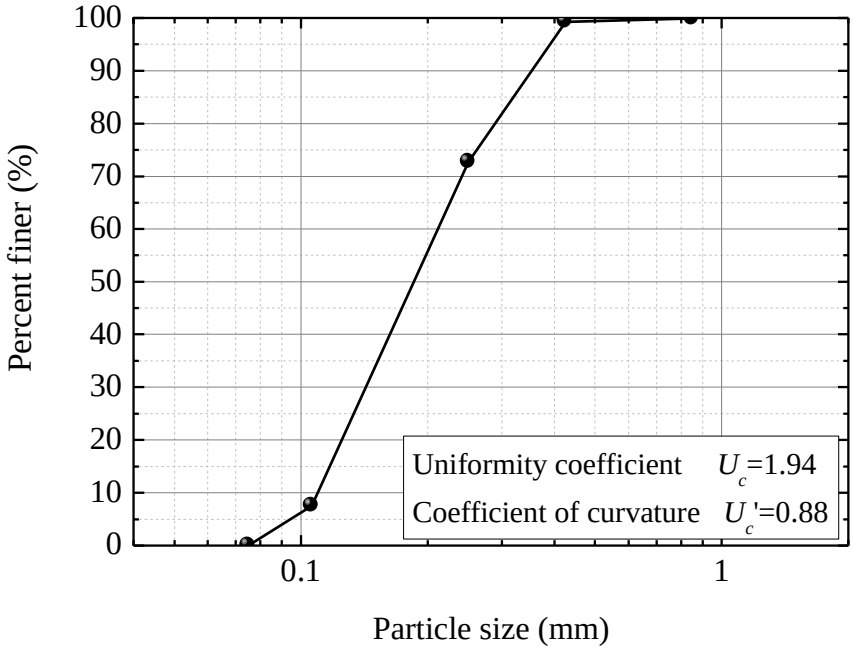

Figure 3.2 Particle size distribution of sand

very low because of the simple granular sand and low dry density.

Model pipe

Although thrust forces generally act on the pipe bends, the various boundary conditions (e.g. the length of the pipe and the angles of the bends) are fairly complex in a

Table 3.1 Properties of silica sand

Density of sand particles (g/cm^3)	2.64
Maximum void ratio	1.11
Minimum void ratio	0.66
Internal friction angle (^{o})	37.9

Table 3.2 Properties of soil bed

Saturated unit weight (kN/m^3)	18.1
Dry unit weight (kN/m^3)	13.4
Relative density (%)	40.0
Void ratio	0.93

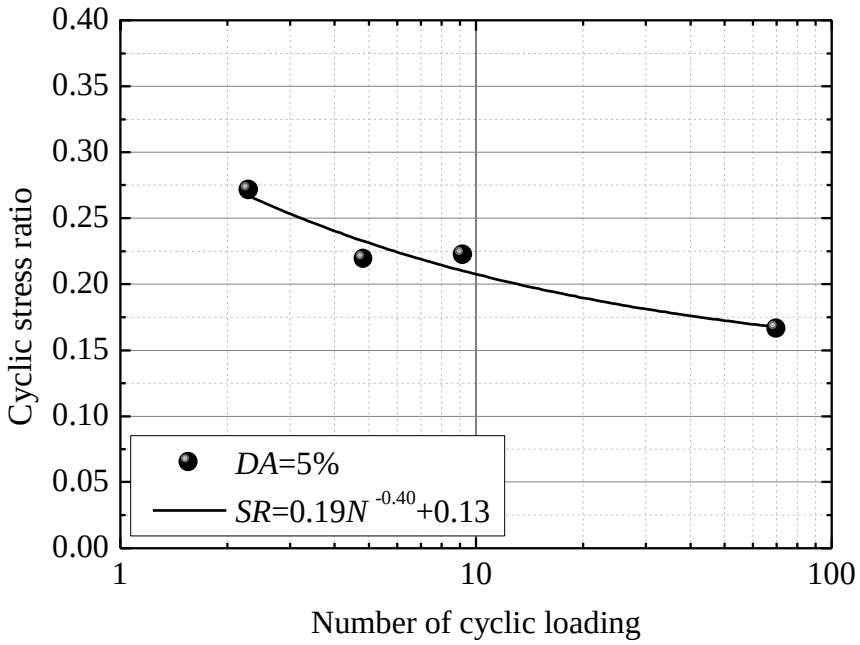

Figure 3.3 Variation of cyclic stress ratio with number of cyclic loading

three-dimensional pipe with bends. Therefore, in the present experiment, a straight aluminum pipe was used to obtain the force–displacement relationship under relatively simple conditions. An aluminum pipe modeled a rigid pipe that did not deform in the cross section. The length and the outer diameter of the pipe were 200 mm and 50 mm, respectively. The specific gravity of the pipe was adjusted to be the same as that of the saturated sand bed (= 1.81) to prevent the pipe from floating and settling during backfilling. Non-woven fabrics

were attached on the both ends of the pipe to mitigate the frictional resistance between the wall surface and the pipe during lateral loading. Moreover, a pore pressure transducer and an earth pressure transducer were embedded in the spring-line of the pipe.

3.2.2 Experimental procedure

The bottom of the test container was connected to an external water tank through a thin-flex tube. By making a head difference between the water levels in the water tank and in the container, the upward seepage was given to the soil bed to generate the excess pore water pressure for reducing the effective stress of the soil bed. By regulating the hydraulic gradient ($i = H/L$), any target liquefaction-levels can be reproduced.

After stabilizing the hydraulic gradient at the prescribed height, the pipe was pulled to the lateral direction by an electric actuator under displacement control. The pipe and the actuator were connected with a wire, and no vertical constraints were applied to the pipe. The pipe was pulled 60.0 mm divisionally twice. After the first traction (30.0 mm), once the tensile force applying to the wire was released, the second traction (30.0 mm) was conducted. The loading rate of the pipe was determined based on the past research. For instance, Yasuda et al. (1987) and Kiku et al. (1989) conducted tests at 1.0 ~ 2.0 mm/s and Towhata et al. (1999) carried out at 4.0 and 8.0 mm/s. Suzuki et al. (1993) and Sato et al. (2000) conducted the lateral loading at 30.0 mm/s and more. Their loading rate is relatively high because their studies all focused on influence of the lateral ground flow. In contrast, as the studies focusing on the thrust force, the loading rate of the experiment performed by Sawada et al. (2005) was 0.5 mm/s, and Itani et al (2015) set at 0.1 ~ 1.0 mm/s. Considering these past studies, total six loading rates were prepared: 0.1, 1.0, 5.0, 10.0, 15.0, and 20.0 mm/s.

The lateral loading was conducted for the hydraulic gradient of i = 0.0, 0.5, and 1.0. The hydraulic gradient of 0.0 represents the saturated condition. The experiment was also carried out for the pipe buried in the dry sand of which relative density was the same with the other cases to confirm the influence of the pore water on the resistive force.

3.3 Variation of Lateral Resistive Force with Displacement

Figure 3.4 shows the variation of the lateral resistive force with the lateral displacement at the loading rate of 0.1 mm/s. Note that the measured force is scaled by the projected area of the pipe (0.05 m × 0.2 m = 0.01 m^2). The resistive force increases non-linearly with the lateral displacement. The resistive force of the dry sand is the largest of all, and the force decreases as the hydraulic gradient increases. As is the case with many past research conducted in dry sand, any force-displacement curves under saturated sand have non-linear relationship. In the second traction after unloading, the resistive force is immediately measured, and it follows the previous force-displacement curves. This result indicates that the soil bed possesses the stress history against the pipe displacement.

Figure 3.5 shows the variation of the maximum resistive force with the excess pore water pressure ratio at the loading rate of 0.1 mm/s. The excess pore water pressure ratio is the average of that calculated from the excess pore water pressure measured at P3 ~ P12 (see **Figure 3.1**). The all-experimental results in both of two tractions are plotted with the approximate lines estimated by a least-squares method. The lateral resistive force decreases

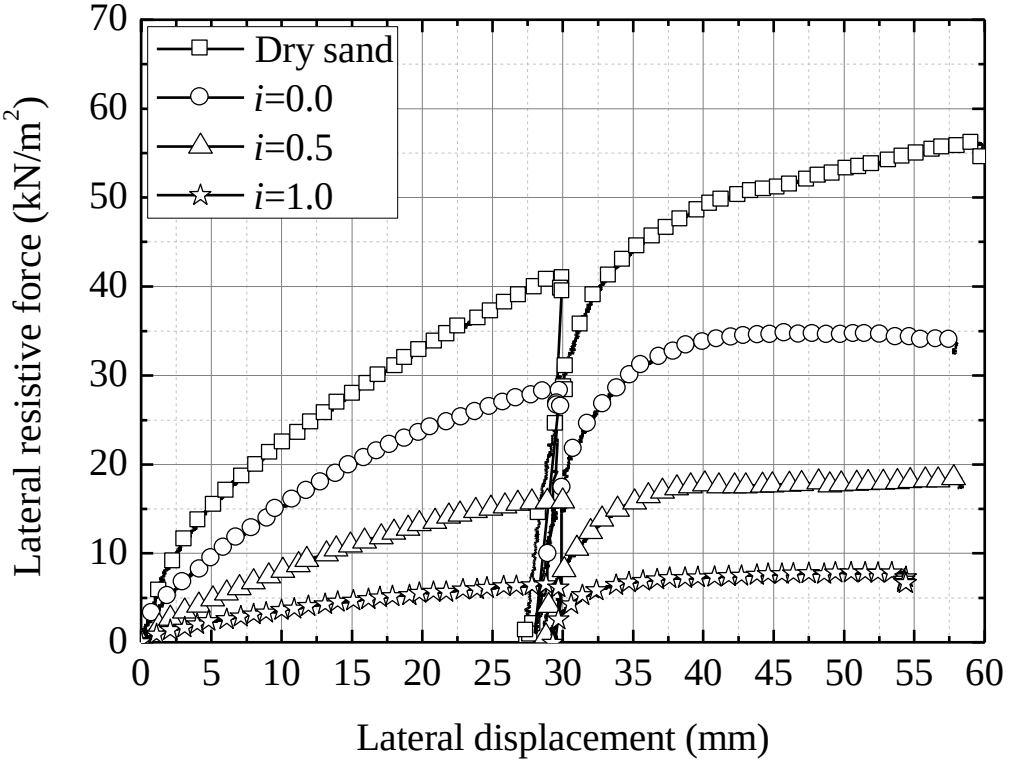

Figure 3.4 Force-displacement curve (v = 0.1 mm/s)

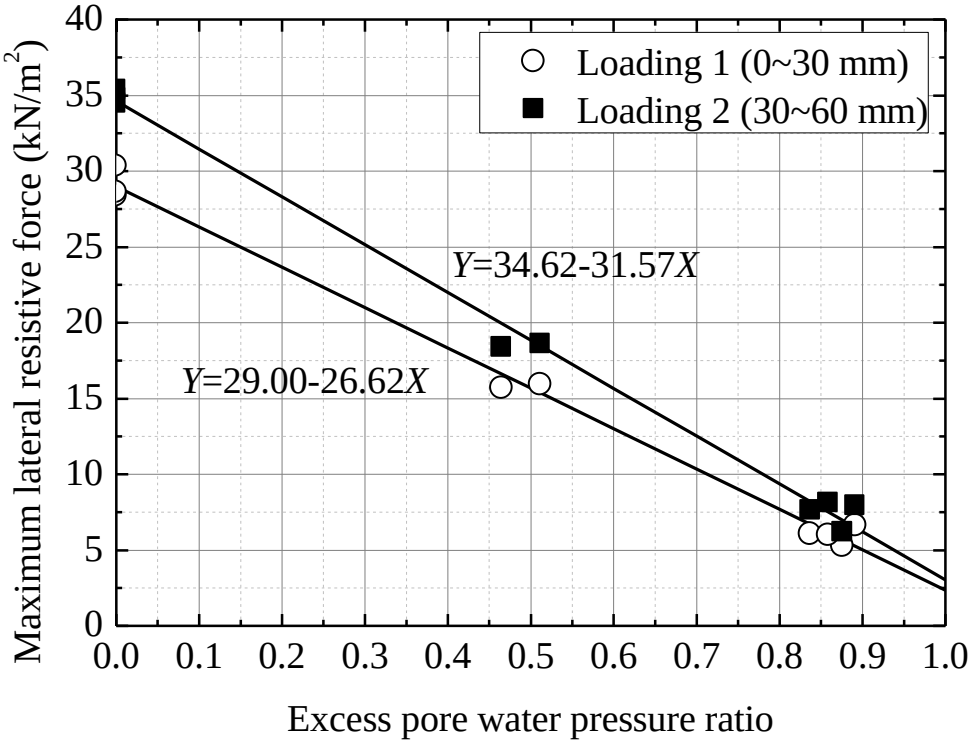

Figure 3.5 Variation of maximum resistive force with excess pore water pressure ratio

linearly in accordance with the increment of the excess pore water pressure ratio. The lateral resistive force of the perfectly liquefied sand (excess pore water pressure is 1.0) extrapolated from the approximate line is approximately 8% of that of the saturated sand. This result implies that the liquefied sand still has the resistive force.

3.4 Rate Dependence of Lateral Resistive Force

3.4.1 Lateral resistive force in saturated sand

Figure 3.6 shows the variation of the lateral resistive force with the lateral displacement at loading rate of 0.1 ~ 10.0 mm/s. In the dry sand, similar force-displacement curves are described under different loading rate. Hsu (1993) conducted a series of lateral loading experiments on a buried pipe in dry dense-sand (ρ_d = 1.75 g/cm^3). The author indicated that there was a positive correlation between the loading rate and the lateral resistive force. On the contrary, the present results imply that the influence of the loading rate on the resistive force can be ignored in the relatively loose sand.

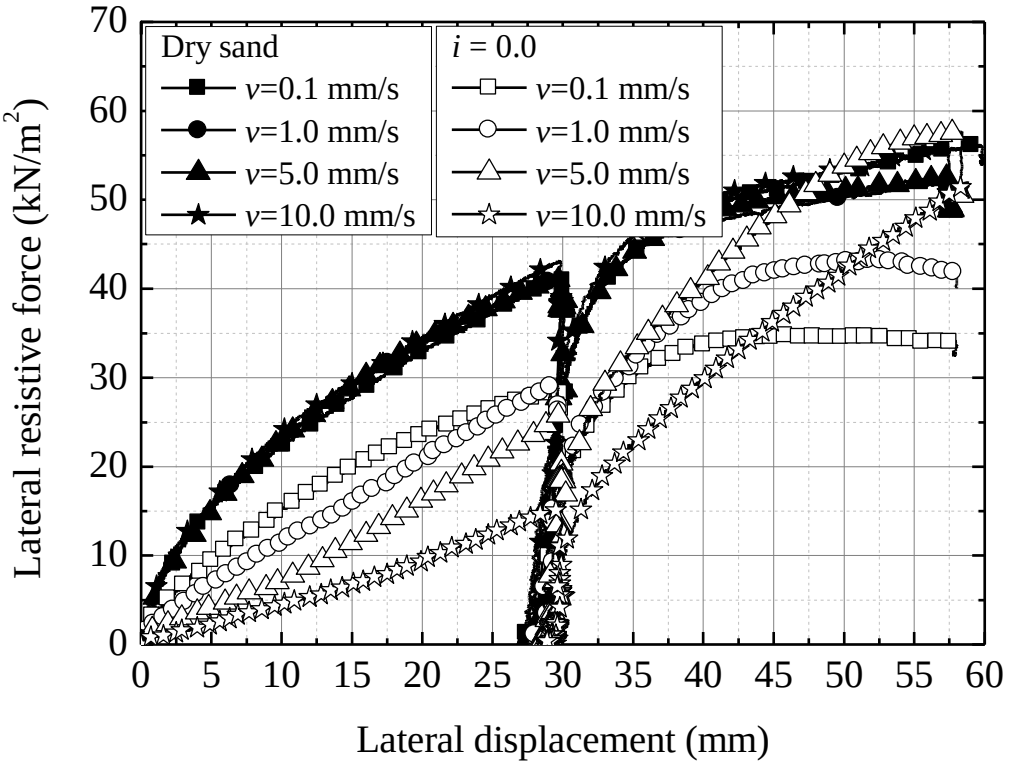

(a)

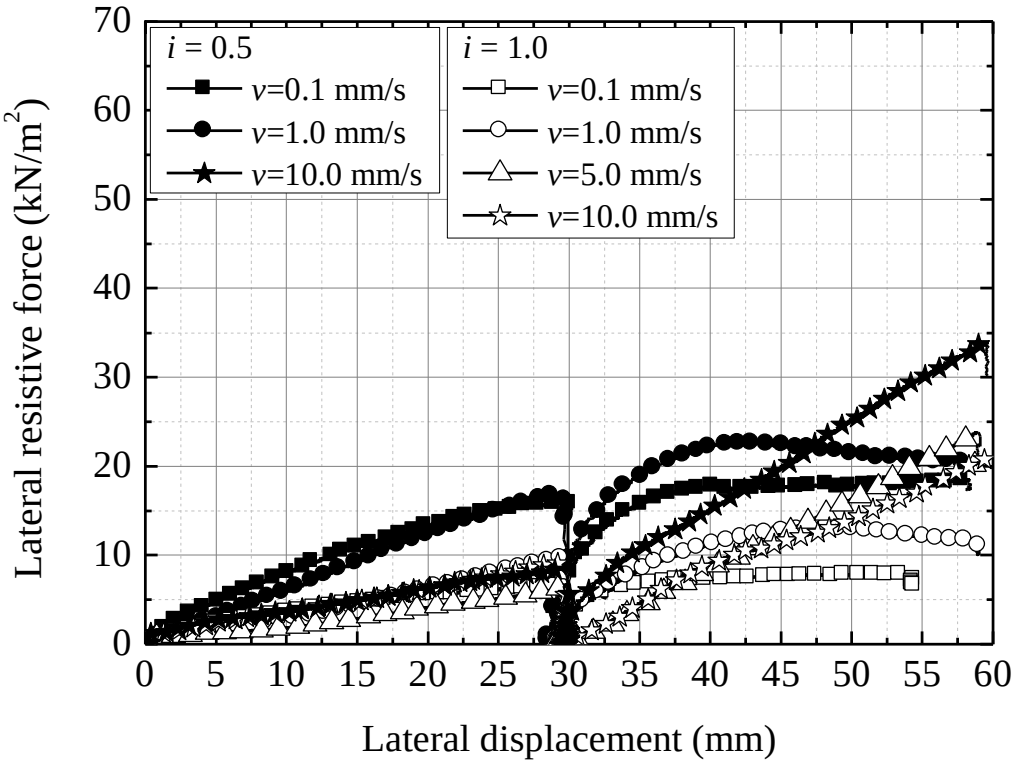

(b)

Figure 3.6 Force-displacement curve (v = 0.1 ~ 10.0 mm/s):
(a) Dry sand, i = 0.0 and (b) i = 0.5, i = 1.0

In contrast, in the saturated sand (i = 0.0), the resistive force decreases as the loading rate increases. Considering the results in the dry sand, it is clear that the pore water influences on the resistive force. Similarly, in the soil bed with the initial hydraulic gradient of 0.5, the resistive force decreases with the increase in the loading rate.

Figure 3.7 shows the variation of the excess pore water pressure ratio in the saturated sand during the lateral loading. Note that the excess pore water pressure ratio is calculated from the initial effective overburden pressure and the excess pore water pressure. The excess pore water pressure was measured at the pore pressure transducer embedded in the pipe. **Figure 3.7 (a)** indicates that the excess pore water pressure ratio on the passive (right) side of the pipe increases rapidly right after the loading starts. This increment was attributed to the negative dilatancy of the soil on the passive side due to the soil compression. The variation of the excess pore water pressure ratio increases as the loading rate increases, and the ratio exceeds 1.0 temporarily at the loading rate of 10.0 mm/s. In other words, the soil on the passive side partially liquefies temporarily due to the displacement of the pipe. Above results indicated that the lateral resistive force in the saturated sand greatly varied because of the rise of the excess pore water pressure due to the displacement of the pipe. **Figure 3.7 (b)** shows the enlarged view of the variation of the excess pore water pressure in the active side (left side) of the pipe. The ratio decreases to the negative value immediately after the pipe starts to move. Although this negative pressure is due to the development of voids behind the pipe, this degree of the pressure has no great influence on the resistive force of the pipe.

Figure 3.8 shows the variation of the maximum excess pore water pressure ratio with the loading rate in the saturated sand. The excess pore water pressure is calculated by the same way as **Figure 3.7**. The maximum measured values are plotted for each loading rate. The maximum excess pore water pressure ratio increases non-linearly, and reaches approximately 1.15 at the loading rate of 10.0 mm/s and more. In other words, the excess pore water pressure generated at high loading rate was approximately equal to the effective overburden pressure. The reason why the excess pore water pressure exceeded 1.0 was presumed to be that the effective stress on the passive side increased due to the increase in the passive restraint in response to the displacement of the pipe.

The above results qualitatively revealed that the soil bed on the passive side perfectly

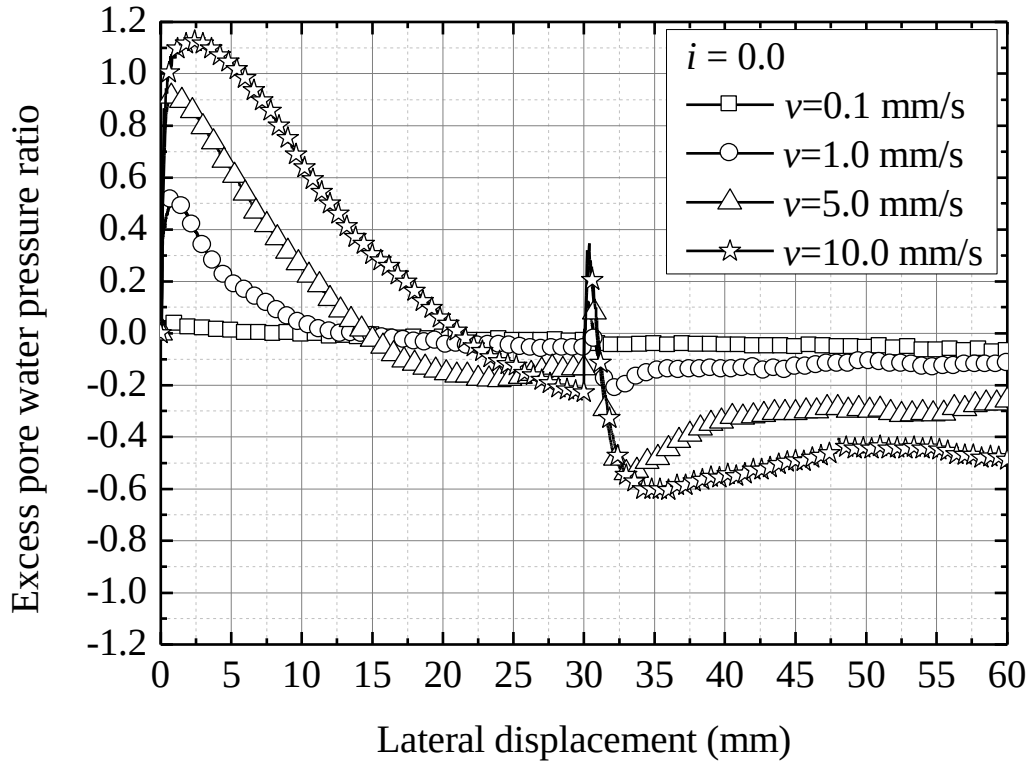

(a)

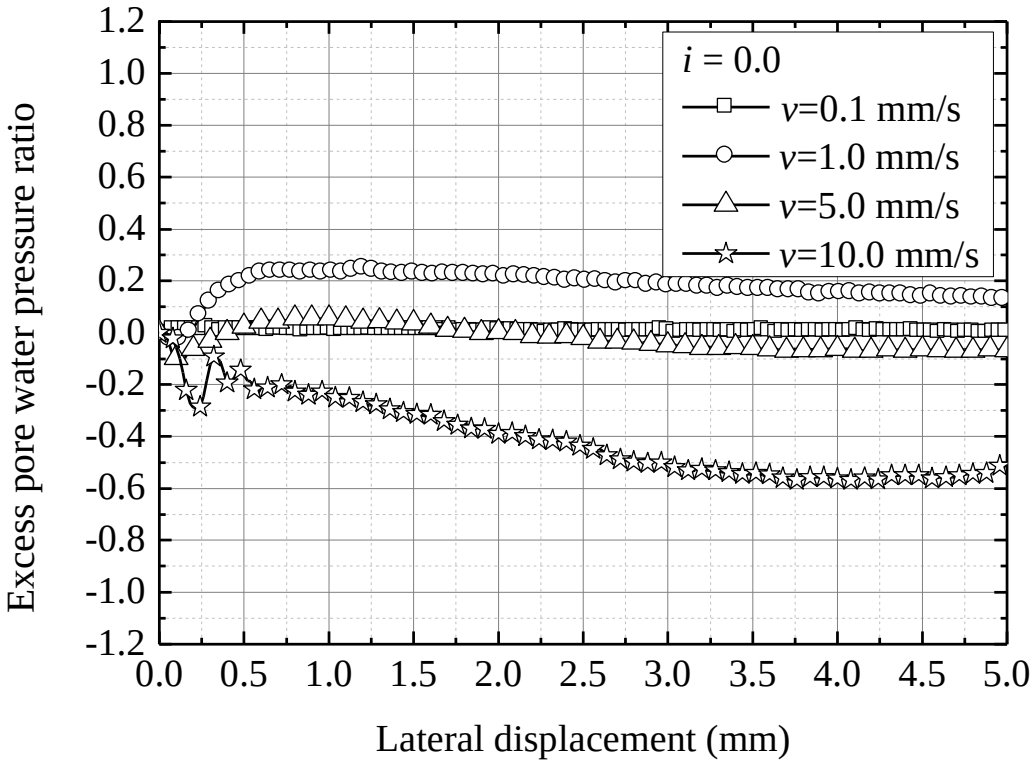

(b)

Figure 3.7 Variation of excess pore water pressure ratio with lateral displacement on: (a) passive side and (b) active side

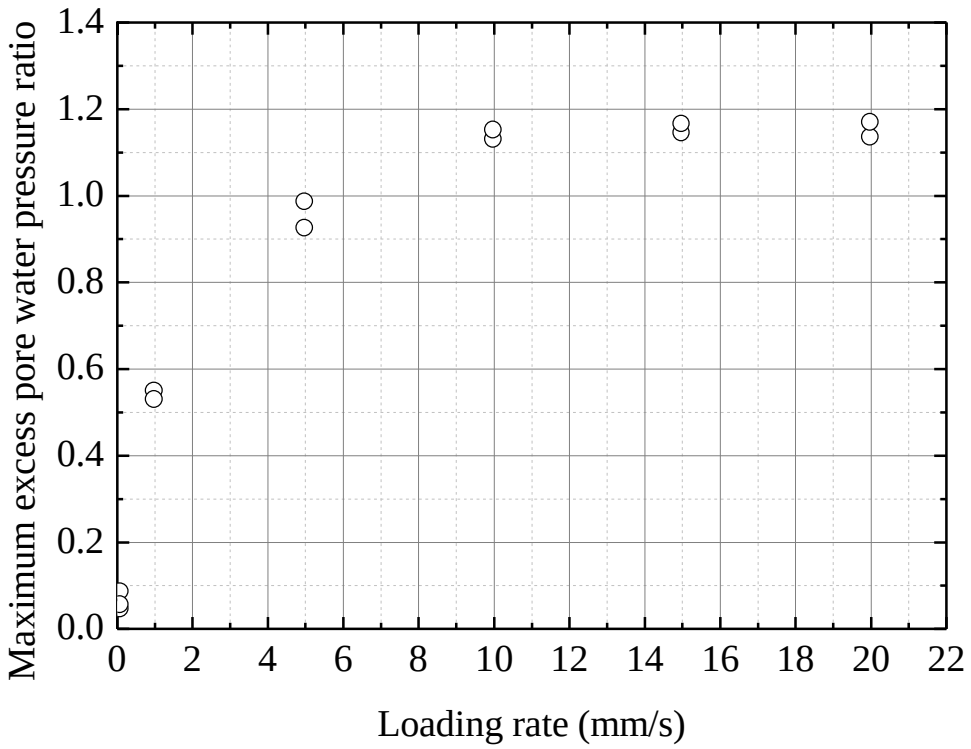

Figure 3.8 Variation of maximum excess pore water pressure ratio with loading rate (i = 0.0)

liquefied due to the displacement of the pipe when the loading rate was relatively high. However, it should be noted that the relationship between the loading rate and the excess pore water pressure ratio greatly varies depending on the diameter of the pipe, the density of the soil bed, or confining pressure.

3.4.2 Lateral resistive force in liquefied sand

The coefficient of the subgrade reaction is calculated to clarify the influence of the excess pore water pressure on the lateral resistive force. The coefficient of the subgrade reaction is a gradient of a secant line obtained from the following equation:

$$K = \frac{P}{\delta A} \tag{3.1}$$

where K is the coefficient of the subgrade reaction (kN/m^3), P is the lateral resistive force (kN), δ is the lateral displacement (m), and A is the lateral projected area of the pipe (m^2). In reference to the experimental study by Yasuda et al. (1987), the coefficient at the displacement

of 5.0 mm is calculated. **Figure 3.9** shows the variation of the coefficient of the subgrade reaction with the loading rate under each hydraulic gradient. It should be noted that the experiments at i = 0.5 was conducted only at the loading rate of 0.1, 1.0, and 10.0 mm/s. Each variation of plot shows that the influence of the loading rate on the coefficient of the subgrade reaction differs depending on the initial effective stress.

The coefficient of the saturated sand (i = 0.0) decreases as the loading rate increases within the range of 0.1 to 10.0 mm/s. The coefficient is the smallest at the loading rate of 10.0 mm/s, and this rate perfectly matches the one at which the soil on the passive side liquefies (see **Figure 3.8**). This result implies that the resistive force has a lower limit because only the effective overburden pressure determines an upper limit of the excess pore water pressure without depending on the loading rate. The coefficient turns to an increasing trend when the loading rate exceeds 10.0 mm/s, and varies along that at i = 0.5 and 1.0. In other words, the rate dependence of the saturated sand (i = 0.0) has developed as a liquefied sand because the soil on the passive side of the pipe liquefies due to the displacement of the pipe.

When the initial hydraulic gradient is 1.0, the coefficient of the subgrade reaction slightly decreases within the range of 0.1 to 5.0 mm/s because the excess pore water pressure

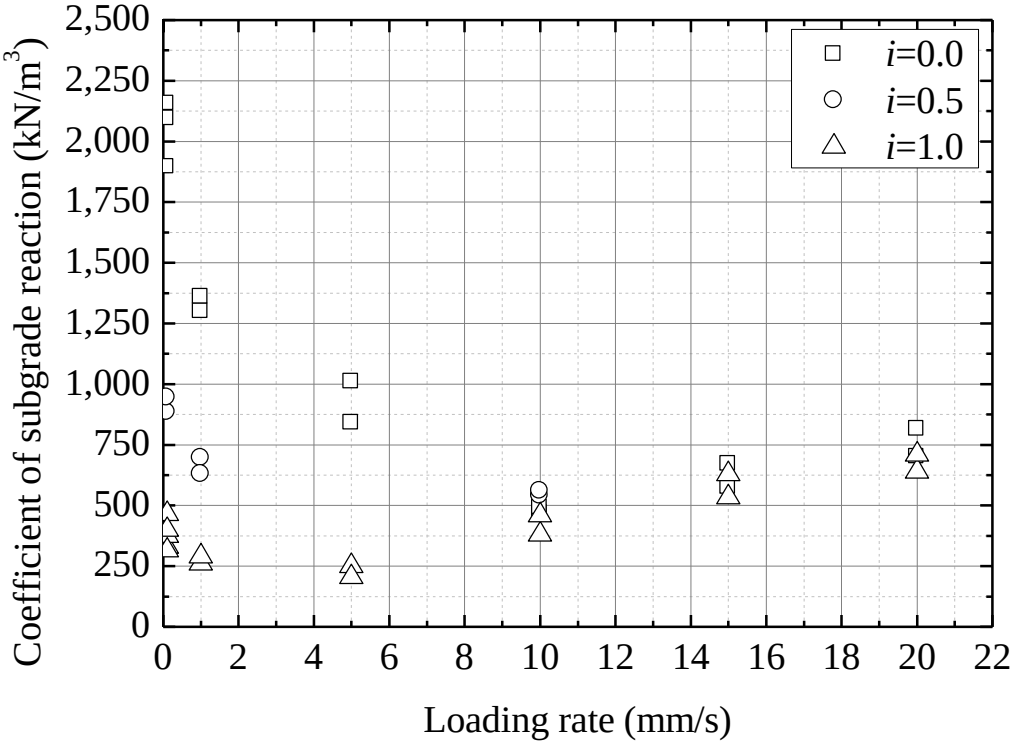

Figure 3.9 Variation of coefficient of subgrade reaction with loading rate

increases slightly due to the pipe displacement (see **Figure 3.7 (a)**). In contrast, when the loading rate is 5.0 mm/s and more, the coefficient increases in proportion to the loading rate. Towhata et al. (1999) or Dungca et al. (2006) reported the rate dependence of the lateral resistive force due to the apparent viscosity from their lateral loading experiments for a model pipe. We can see similar tendency in the present experiment. The coefficient of the saturated sand at the initial hydraulic gradient of 0.5 is positioned at just between two cases, and shows the smallest value at the loading rate of 10.0 mm/s as the same with that at $i = 0.0$.

3.5 Thrust Restraint by Gravel and Geogrid

3.5.1 Outline of thrust restraint

In this section, the applicability of a thrust restraint method combining gravel and geogrid during liquefaction is examined.

The mean particle-size and the dry density of the gravel were 6.75 mm and approximately 1.50 g/cm^3, respectively. NETLON sheet Z20B (Mitsui Kagaku Sanshi, Inc.) was used as the geogrid. The allowable tensile strength and the mesh size were 6.0 kN/m and 5 × 5 mm, respectively. **Figure 3.10** shows the schematic diagram of the backfill. In reference to the past study (Sato et al. (2000)), total three backfill conditions were proposed. Each condition is as follows. Type-A is a basic case: the pipe is buried in the sand bed directly without any countermeasures. The experimental results have already been shown in previous

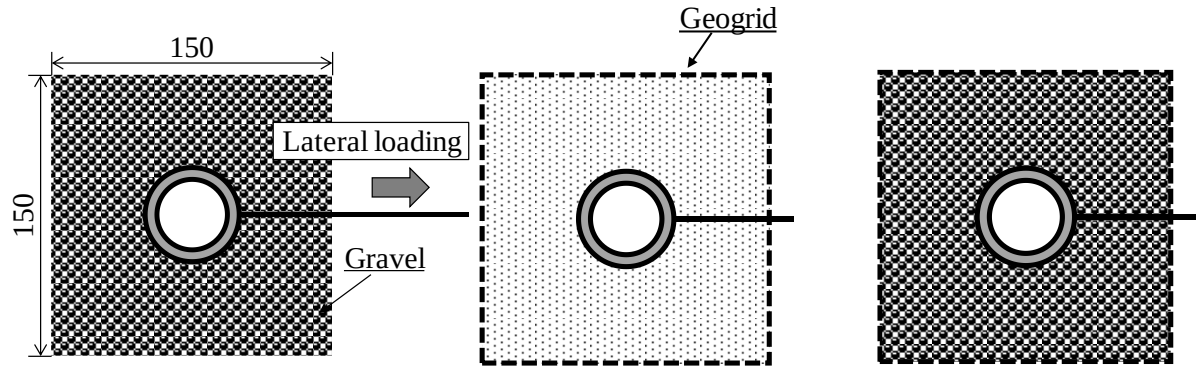

Figure 3.10 Backfill condition around pipe:
(a) Type-B, (b) Type-A_G, and (c) Type-B_G

sections. In Type-B, the square area (3*D*) surrounding the pipe is buried with the gravel. In Type-A_G, the geogrid integrates the sand in the square area surrounding the pipe. In Type-B_G, the geogrid integrates the gravel zone in Type-B. The geogrid was overlapped on the top and was fixed with cable-ties. In each case, lateral loading was applied to the pipe with the loading rate of 0.1 mm/s at the hydraulic gradient of 0.0, 0.5, and 1.0.

3.5.2 Dissipation effect of excess pore water pressure

Figure 3.11 shows the variation of the excess pore water pressure ratio in the process of increasing the hydraulic gradient from 0.0 to 1.0. The excess pore water pressure ratio is calculated from the initial effective overburden pressure and the increment of the excess pore water pressure from i = 0.0. The excess pore water pressure ratio is average of that measured at P3 ~ P12 (see **Figure 3.1**). Note that when the pipe is partially backfilled with the gravel (Type-B and Type-B_G), the excess pore water pressures at P3, 7, 8, and 12 are used for the calculation. The ideal relationship obtained from the critical hydraulic gradient of the sand

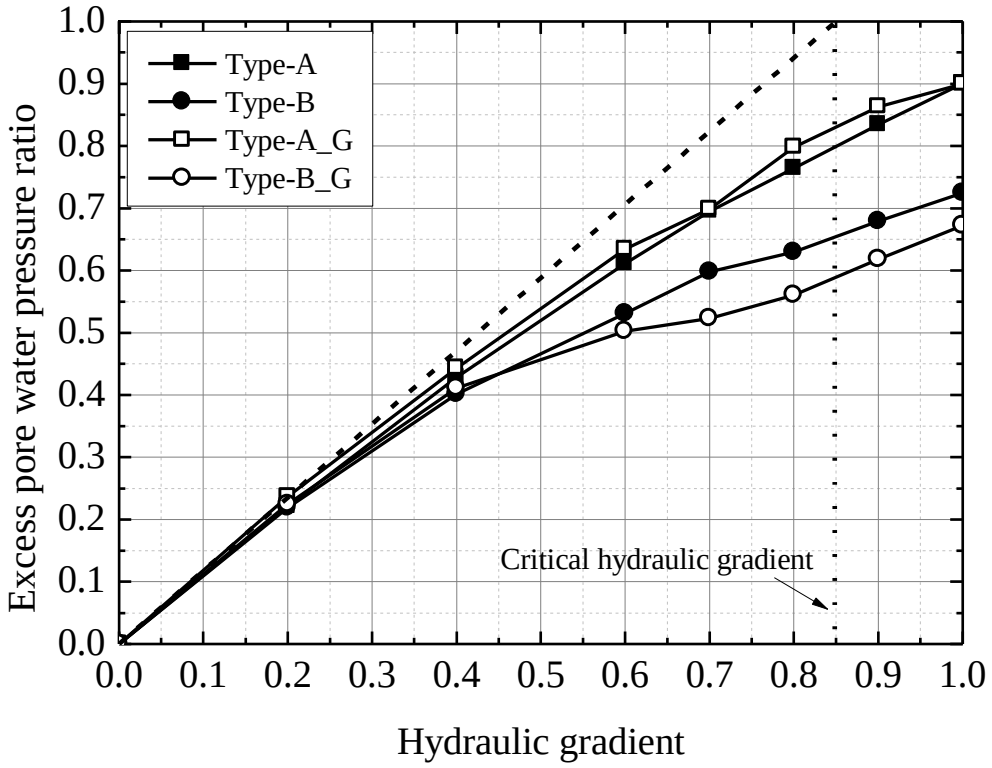

Figure 3.11 Variation of excess pore water pressure ratio with hydraulic gradient

bed is also drawn in the graph as short-dashes line. The critical hydraulic gradient of the soil is calculated as

$$i_{cr} = \frac{G_s - 1}{1 + e} \tag{3.2}$$

where G_s is the specific gravity of the sand particles (= 2.64) and e is the void ratio (= 0.93).

The graph indicates that the increasing rate of the excess pore water pressure ratio in Type-B is lower than that of Type-A. The difference is evident when the hydraulic gradient is 0.6 or more. The ratio at i = 1.0 is approximately 0.7, which is roughly equal to that at i = 0.7 in Type-A. The suppression of the excess pore water pressure was attributed to the flow of the upward seepage toward the gravel zone due to the comparatively high hydraulic conductivity. The relationship between the hydraulic gradient and the excess pore water pressure ratio in Type-A_G and Type-B_G is almost the same with that of Type-A and Type-B, respectively.

Figure 3.12 shows the variation of the hydraulic conductivity with the hydraulic gradient in Type-A, B, A_G, and B_G. the hydraulic conductivity is calculated based on Darcy's law from the hydraulic gradient and the measured flow rate. The hydraulic conductivity is almost the same under different hydraulic gradient. Since there is no

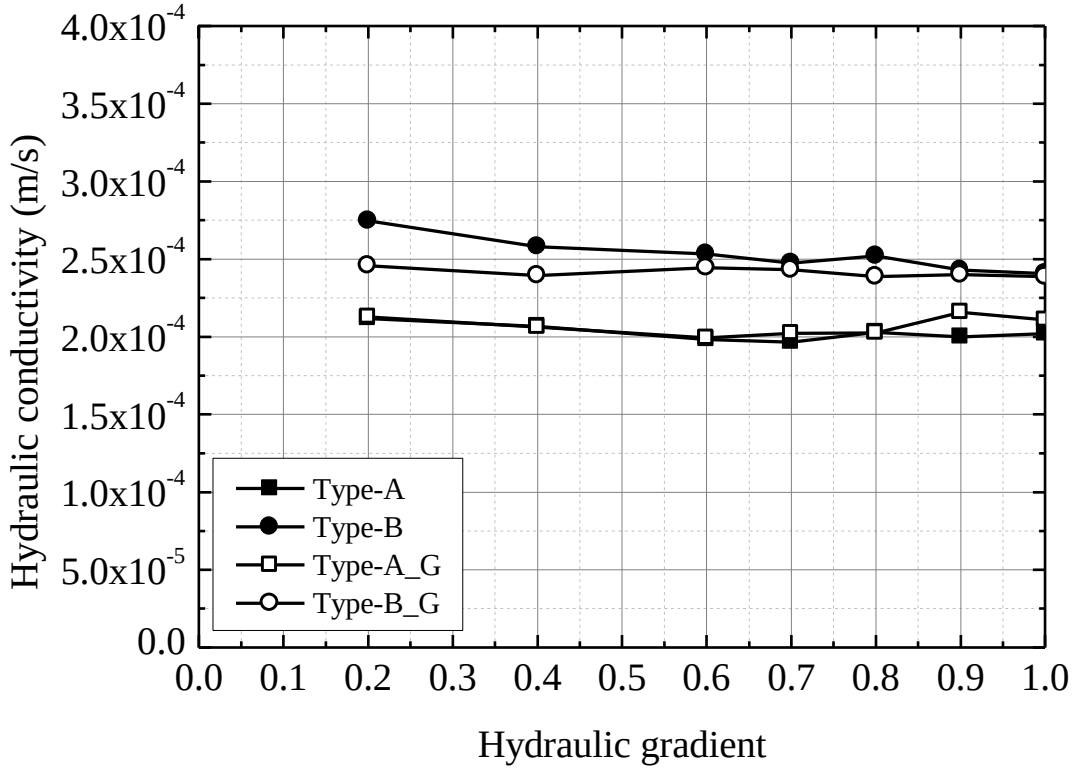

Figure 3.12 Variation of hydraulic conductivity with hydraulic gradient

significant difference between Type-A and A_G, or Type-B and B_G, the influence of the geogrid on the permeability can be ignored. In comparison of the results between in Type-A and Type-B, the variation of the hydraulic conductivity due to the partial substitution of the gravel is very small: the difference is approximately 5.0×10^{-5} m/s. This result implies that the substitution of the gravel has little influence on the hydraulic conductivity of the soil bed because the installation volume of the gravel is relatively small in comparison with the whole volume of the sand bed.

3.5.3 Resistive force in saturated sand

Figure 3.13 shows the variation of the lateral resistive force with the lateral displacement of the pipe in the saturated soil (i = 0.0). Firsty, the results at i = 0.0 are compared because the permeability of the soil bed greatly changed depending on the backfill condition (see **Figure 3.11**). Note that the lateral loading in Type-B_G was forcibly terminated at Y = 18 mm due to the capacity of the load cell.

The graph shows that each resistive force in Type-B, A_G, and B_G is larger than

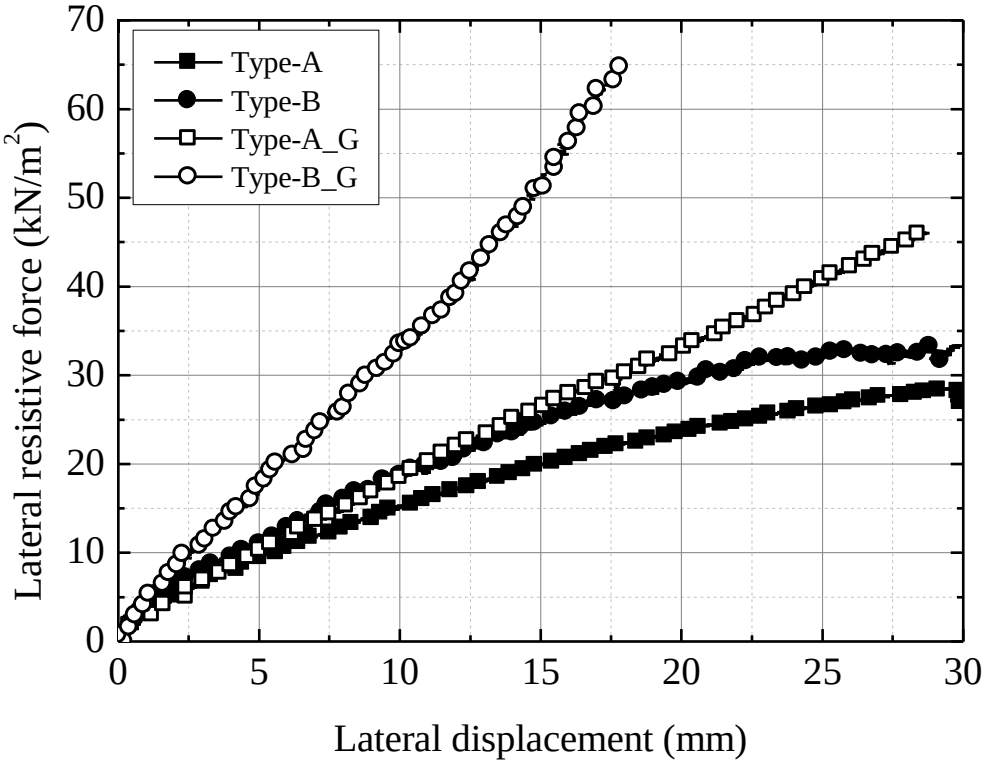

Figure 3.13 Force-displacement curve in Type-A, B, A_G, and B_G

that of Type-A, indicating that the gravel and the geogrid surely contribute to an increase in the resistive force. The relationships between the lateral displacement and the resistive force in Type-A and B are non-linear: each increment of the resistive force decreases with the lateral displacement. In contrast, the force-displacement relationships in Type-A_G and B_G are almost linear and have no peak until the pipe moves 30.0 mm.

Figure 3.14 shows the increment of the lateral resistive force in Type-B, A_G, and B_G against Type-A. The graph indicates that the increment of the resistive force in the very beginning of the lateral loading in Type-B is larger than that in Type-A_G. The all increment of the lateral resistive force in Type-B was due to the shear resistive force of the gravel because the hydraulic gradient of the soil was the same (i = 0.0). In contrast, when the lateral displacement is 15.0 mm and more, the increment of the resistive force in Type-A_G is larger than that of Type-B, and this difference is expanding with the pipe displacement. The above results imply that the geogrid reinforcement is more effective than the gravel when the pipe greatly moves although it is not exerted immediately after the pipe displaces.

The difference of the resistive force is the largest between Type-A and Type-B_G. The difference is increasing non-linearly with the lateral displacement. This variation of the

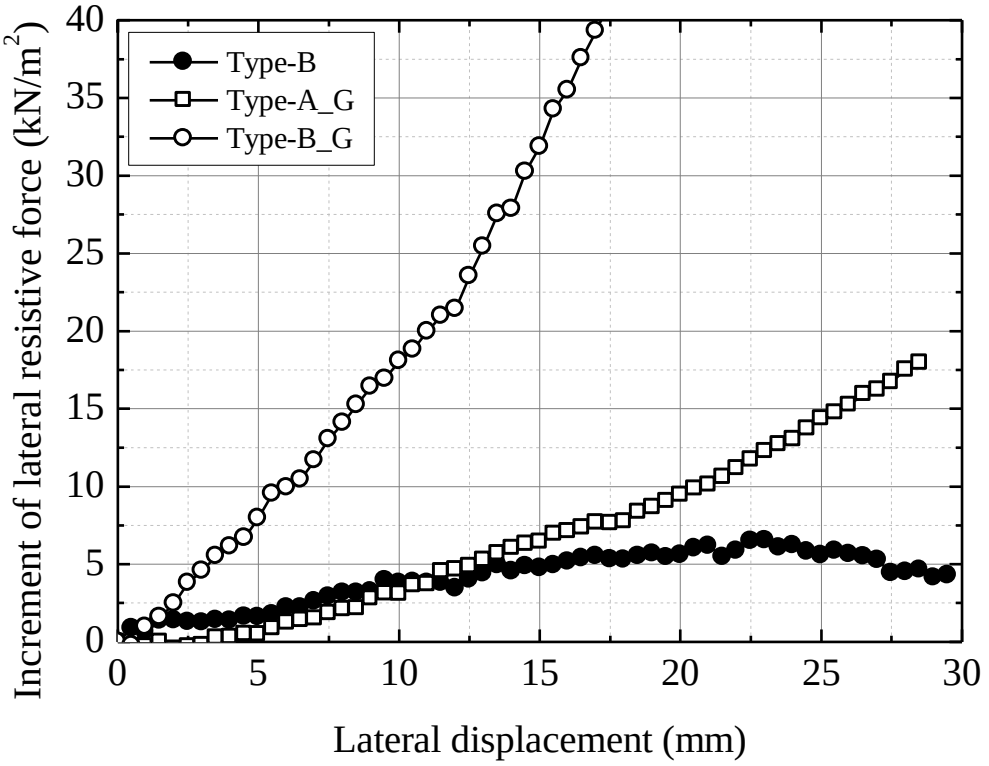

Figure 3.14 Increment of resistive force in Type-B, A_G, and B_G

difference is due to the linear relationship as shown in **Figure 3.13**. The tendency is the same as in the past study by Hirakawa et al. (2005) that examined the characteristics of the supporting force of the reinforced ground. That is, the geogrid reinforcement and the decrease in the stiffness of the soil due to the shear fracture is balanced. Moreover, the comparison between Type-A_G and B_G clearly shows that the physical properties of the constrained soil material inside the geogrid have a great influence on the development of the resistive force because the integrated volume is the same in both cases. The superiority over each countermeasure is in good agreement with the preceding study by Sato et al. (2000).

3.5.4 Resistive force in liquefied sand

Figure 3.15 shows the variation of the lateral resistive force with the excess pore water pressure ratio. The excess pore water pressure ratio is calculated from the excess pore water pressure measured just before the lateral loading. The lateral resistive force when the pipe displaces 15.0 mm is plotted in reference to the experimental results carried out on the same scale (Itani et al., 2015). Note that the lateral displacement of 15.0 mm is corresponding to the displacement of the pipe when the lateral loading of 19.6 N, which is equal to the total of passive earth pressure behind the pipe, is applied to the pipe in the liquefied sand. In other words, it is a reasonable displacement of the pipe during liquefaction in the present model scale. The approximation lines obtained by a least-squares method are superimposed for Type-A and B.

The lateral resistive force decreases with the increase in the excess pore water pressure in all cases. As is clear from the approximate lines in Type-A and B, the difference between them becomes less clear as the excess pore water pressure ratio increases. Especially when the ratio is more than 0.5, this trend is obvious. The limited shear resistive force by the gravel is not sufficiently demonstrated because the resistive force of the sand that occupies the most of the soil bed decreases as the excess pore water pressure increases. However, the rise of the excess pore water pressure of the soil surrounding the pipe is suppressed in some extent by using the gravel as the backfill as shown in **Figure 3.11**. In other words, the suppressing effect of the rise of the excess pore water pressure contributes sufficiently to securing the

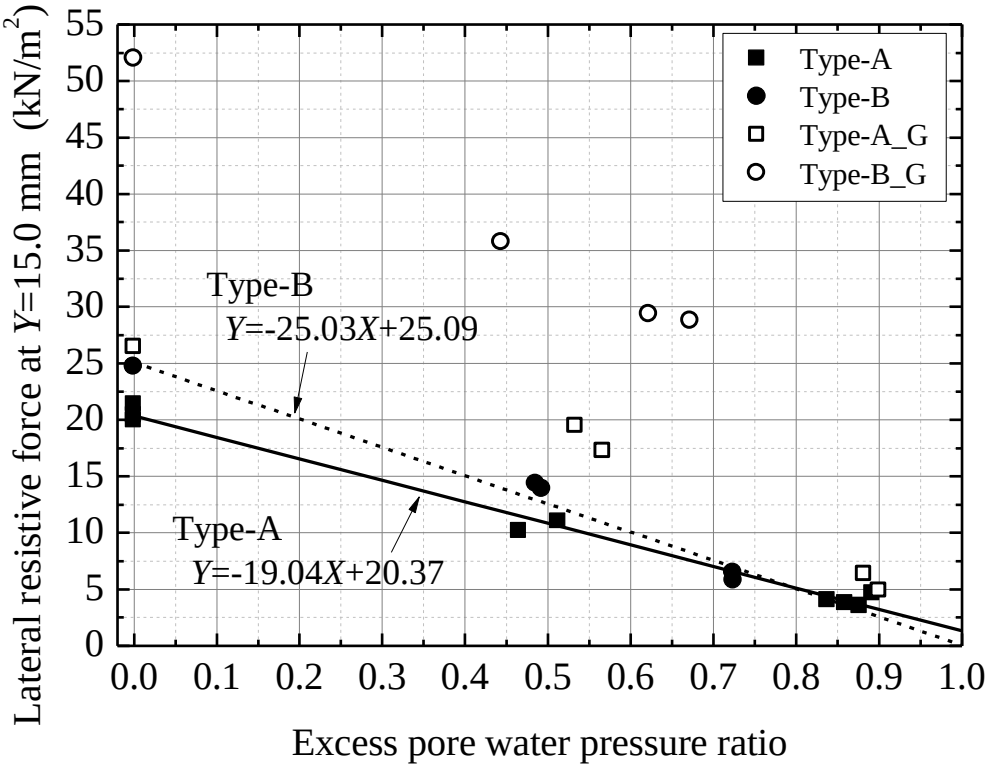

Figure 3.15 Variation of lateral resistive force at Y = 15.0 mm with excess pore water pressure ratio

resistive force of the backfill although the shear resistive force given by the gravel is lost somewhat due to liquefaction.

3.5.5 Geogrid Reinforcement

Figure 3.16 shows the variation of the increment rate of the lateral resistive force by geogrid in Type-A_G and B_G with the excess pore water pressure ratio. The increment rate of the resistive force is defined as below.

$$I_r = \frac{P_{Type-AG} - P_{Type-A}}{P_{Type-A}} \times 100 \tag{3.3}$$

where I_r is increment rate (%) and P is the resistive force (kN) at Y = 15.0 mm. The increment rate in Type-B_G is calculated in the same way with the resistive force in Type-B. Note that the resistive force in Type-A and B at each excess pore water pressure is obtained from the approximate lines shown in **Figure 3.15**. The increment rate by the geogrid is larger in

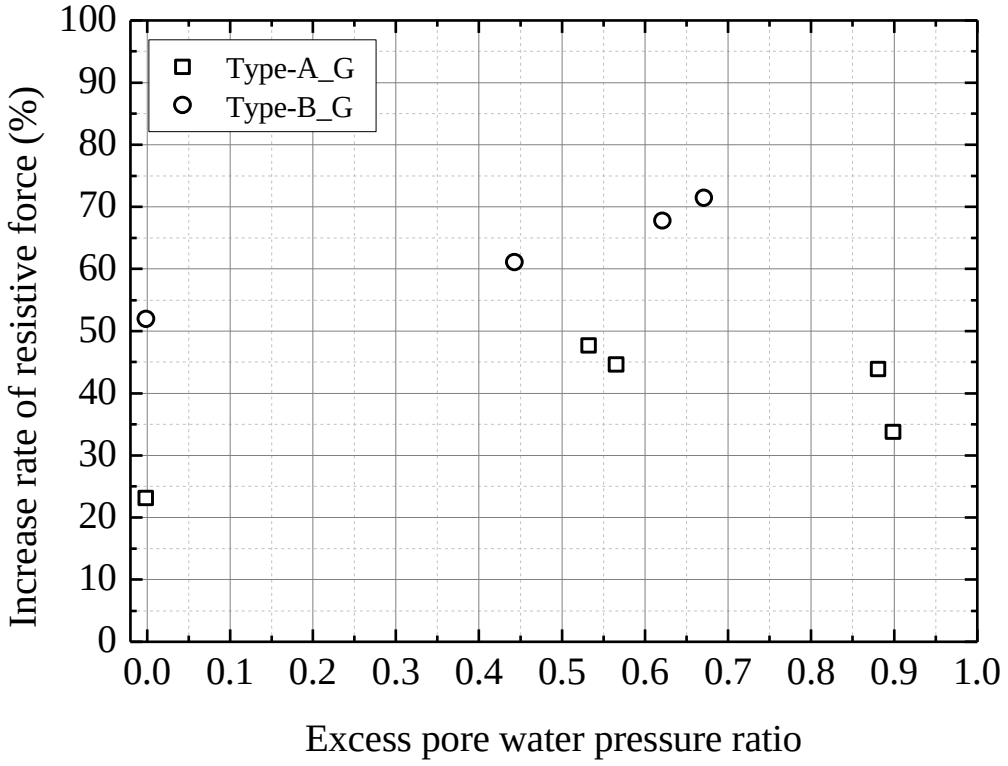

Figure 3.16 Variation of increment rate of resistive force by geogrid

Type-B_G and is increasing with the excess pore water pressure ratio. The soil on the passive side of the pipe secured the surface pressure without large deformation by integrating the pipe and the surrounding gravel with the geogrid, and possessed the high shear strength. On the contrary, in Type-A_G, the increment rate of about 40% is exhibited by the geogrid regardless of the magnitude of the excess pore water pressure ratio. However, it should be noted that the resistive force in Type-A was extremely small when the excess pore water pressure ratio was very high. Thus, its geogrid reinforcement is difficult to evaluate.

Figure 3.17 shows the pictures of the pipe and its surrounding soil at i = 1.0 after the lateral loading. The area enclosed by the solid line represents the gravel zone, the broken line shows the arrangement of the geogrid, and a dotted line indicates each initial arrangement.

In Type-A_G, the shape of the geogrid on the right side (passive side) is not greatly deformed, and the position of the geogrid on the left side (active side) has hardly changed. It is expected that the sand particles pushed out by the lateral displacement of the pipe pass through the mesh of the geogrid when the sand is subjected to a certain passive earth pressure. The geogrid reinforcement for soil structures is generally categorized as following three: the

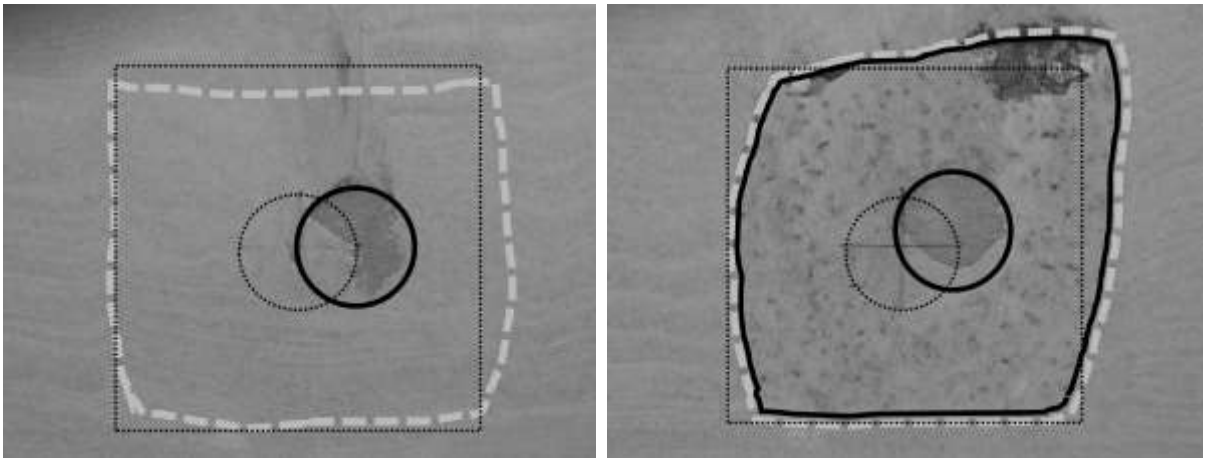

(a) (b)

Figure 3.17 Picture of pipe and surrounding soil after lateral loading (i = 1.0): (a) Type-A_G and (b) Type-B_G

frictional force between upper and lower surfaces of the reinforcing material and the soil material, the tensile force generated in reinforcing material, and the confining effect to suppress the deformation of soil mass (Kawamura et al., 1998). The present reinforcement refers to the increase in the strength of the soil mass by increasing the restraint pressure by limiting the deformation of the soil surrounding the pipe. Once the sand bed liquefies, the frictional force between the upper and lower surfaces of the geogrid and the sand is not sufficiently expected. The confining effect by the geogrid also does not work so much because the sand particles pass through the grid.

On the other hand, in Type-B_G, the supporting force of the passive side soil pushes upward the pipe and the gravel within the geogrid on the passive side. Along with that, the tensile force acts on the entire geogrid, and the gravel and the geogrid on the left side are greatly deformed. This result implies that the resistive force is enhanced by transferring the passive earth pressure generated by the displacement of the pipe to the geogrid integrating the gravel zone. The difference in deformation behavior of the geogrid in Type-A_G and B_G supports the results of the difference in the geogrid reinforcement in each case as shown in **Figure 3.16**.

3.6 Conclusions

In this chapter, lateral-displacement characteristics of a buried pipe during liquefaction were examined by the lateral loading experiments for a model pipe. From the model experiments, following conclusions were made:

1. The lateral resistive force increased non-linearly with the lateral displacement of the pipe. In the reloading process after unloading, the force-displacement relationship varied along the curve obtained before unloading. In other words, the stress history of the soil bed against the lateral displacement of the pipe was observed.
2. The maximum lateral resistive force decreased linearly as the excess pore water pressure ratio of the soil bed increased.
3. In the saturated sand, the excess pore water pressure on the passive side of the pipe raised rapidly and the resistive force decreased due to the pipe movement.
4. The excess pore water pressure reached upper limit when exceeding the certain loading rate, and its upper limit roughly agreed with the initial effective stress of the soil bed. In other word, the possibility that the saturated sand temporarily liquefied by the movement of the pipe was shown.
5. When the excess pore water pressure ratio of the soil on the passive side exceeded 1.0 due to the displacement of the pipe, the lateral resistive force showed the rate dependence that the coefficient of the subgrade reaction increased in proportion to the loading rate.
6. By backfilling the pipe partially with gravel, a rise of the excess pore water pressure was somewhat suppressed due to its high permeability.
7. In the saturated sand, the resistive force was enhanced by substituting the gravel and installing the geogrid due to the high shear strength and the dissipation effect. The geogrid reinforcement was quite larger than that of the gravel. In the liquefied sand, the countermeasure that integrated the gravel surrounding the pipe with the geogrid was the most effective to enhance the resistive force.

References

Dungca, J. R., Kuwanoo, J., Takahashi, A., Saruwatari, T., Izawa, J., Suzuki, H., and Tokimatsu, K. 2006. Shaking table tests on the lateral response of a pile buried in liquefied sand, *Soil Dynamics and Earthquake Engineering*, **26**, (2-4), 287-295.

Hirakawa, D., Kongkitkul, W., and Tatsuoka, F. 2005. Rate-dependent bearing capacity properties of shallow foundation on geogrid-reinforced sand, *Geosynthetics Engineering Journal*, **20**, 229-234. (in Japanese with English summary).

Hsu, T. W. 1993. Rate effect on lateral soil restraint on pipelines, *Soils and Foundations*, **33**, (4), 159-169.

Itani, Y., Fujita, N., Yokota, Y., Ariyoshi, M., Mohri, Y. and Kawabata, T. 2015. Model experiment on the horizontal resistance force of buried pipe in liquefied ground, *IDRE Journal*, **83**, (1), 77-83. (in Japanese with English summary).

Kawamura, T., Ochiai, H., and Hirai, T. 1998. Confining effect in geogrid-reinforced soil structure and effect of shape of geogrid, *Geosynthetics Engineering Journal*, **13**, 306-315. (in Japanese with English summary).

Kiku, T., Yasuda, S., and Yoshida, T. 1989. Relationship between restraint force of soil and degree of liquefaction, *Proceedings of the JSCE Earthquake Engineering Symposium*, **20**, 277-280. (in Japanese).

Ministry of Agriculture, Forestry and Fisheries of Japan (MAFF). 2009. Planning and Design Criteria of Land Improvement Project (Pipeline), JSIDRE, 321-409. (in Japanese).

Sato, H., Mohri, Y., and Kawabata, T. 2000. Experiment on the buried pipe subjected lateral force during liquefaction, *35th Japan National Conference on Geotechnical Engineering*, 2147-2148. (in Japanese).

Sawada, Y., Kawabata, T., Kitano, T., Uchida, K., Hirai, T., and Saito, K. 2005. Resistant mechanism on thrust protecting method for buried bend with geogrid, *Geosynthetics Engineering Journal*, **20**, 217-222. (in Japanese with English summary).

Suzuki, N., Yano, T., and Matsuyama, E. 1993. Deformation of buried pipeline subjected to lateral displacement of liquefied soil, *Proceedings of the JSCE Earthquake Engineering Symposium*, **22**, 663-666. (in Japanese).

Towhata, I., Vargas-Monge, W., Orense, R. P., and Yao, M. 1999. Shaking table tests on subgrade reaction of pipe embedded in sandy liquefied subsoil, *Soil Dynamics and Earthquake Engineering*, **18**, (5), 347-361.

Yasuda S., Saito, K., and Suzuki N. 1987. Restraint force of liquefied soil against buried pipe, *Proceedings of the JSCE Earthquake Engineering Symposium*, **19**, 189-192. (in Japanese).

CHAPTER 4

The contents of this chapter are based on:

Ono, K., Yokota, Y., Sawada, Y., and Kawabata, T. 2017. Lateral Force-Displacement Prediction for Buried Pipe under Different Effective Stress Condition, *International Journal of Geotechnical Engineering* (published online)

Chapter 4

Lateral Pipe-Soil Interaction under Different Effective Stress Condition

4.1 Introduction

Buried pipelines subjected to thrust force displace laterally in the direction perpendicular to the axis of the pipeline. The thrust force is an external force generated by the internal water pressure and is regarded as a constant load not depending on the displacement of the pipeline. Quantitative prediction of the displacement of the buried pipeline according to the magnitude of the thrust force is one of the most important issues in terms of the safety design for buried pipelines.

The objective of this chapter is to elucidate the pipe-soil interaction in sand with different effective stress due to liquefaction. To obtain a relationship between the lateral resistive force and the lateral displacement of a pipe subjected to an external force, lateral loading experiments are performed on a model pipe in saturated sand. This chapter pays attention to the relationship between the essential three parameters: lateral displacement, resistive force, and effective stress (or excess pore water pressure). A soil bed with different effective stress is prepared using a similar experimental method as shown in Chapter 3, and a lateral loading is applied to a model pipe under either displacement or load control. From the various viewpoints (e.g. slip surface, contour diagram of excess pore water pressure, profile of ground surface, coefficient of apparent viscosity), the complex interaction between the movement of the pipe and liquefied soil is examined.

4.2 Outline of Lateral Loading Experiment

4.2.1 Equipment and materials

Experimental set-up

The test container was made of stainless-steel and had inner dimensions of 1300 × 400 × 500 mm. A total of 18 pore pressure transducers were installed along the rear wall of the test container as shown in cross section in **Figure 4.1**. The front of the model was monitored through a transparent wall made of acrylic glass.

Sand

The same silica sand used for the experiments in Chapter 3 was used as the backfill material. The physical properties of the sand are shown in **Table 3.1**. The sand was rained from a sieve into the container that held enough water to create a sufficiently saturated soil bed. The properties of the soil bed are shown in **Table 4.1**.

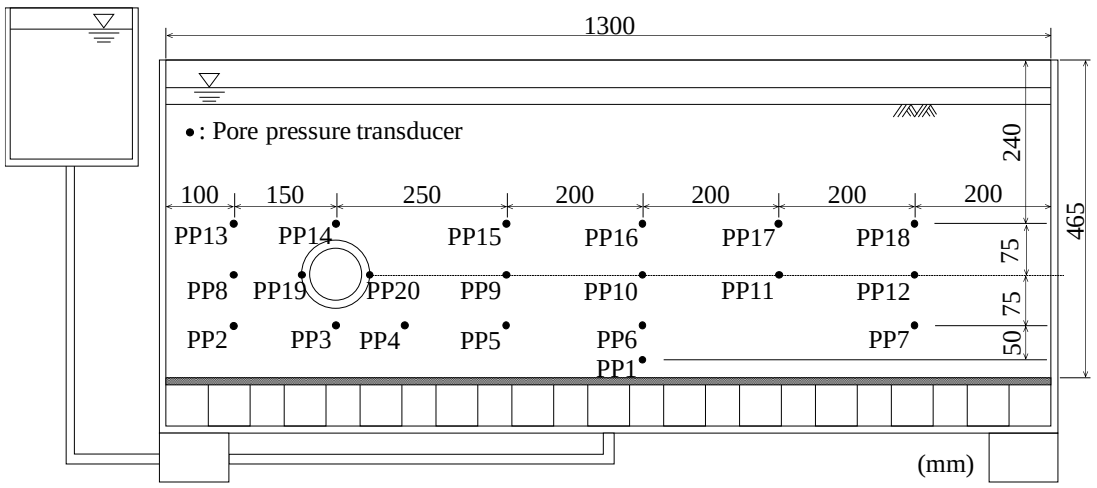

Figure 4.1 Cross section of test container

Table 4.1 Properties of soil bed

Saturated unit weight (kN/m^3)	18.2
Dry unit weight (kN/m^3)	13.6
Relative density (%)	50.0
Void ratio	0.93

Model pipe

The outer diameter and the length of the model pipe were 100 mm and 400 mm, respectively. The pipe having 20 mm thickness was selected so that the specific gravity of the pipe was equal to that of the saturated sand to prevent the pipe from either floating or settling during backfilling. Two pore pressure transducers were embedded in either side of the model pipe. Both ends of the model pipe were closed and covered with non-woven fabric to mitigate the friction from the end walls of the test container.

4.2.2 Experimental procedure

Sand boiling

The bottom of the test container was connected to an external water tank via a hose, and an upward seepage was supplied to the soil bed by raising the hydraulic gradient. This upward seepage increased the excess pore water pressure and decreased the effective stress of the soil. This technique of using sand boiling to reproduce liquefaction is a common one (e.g.

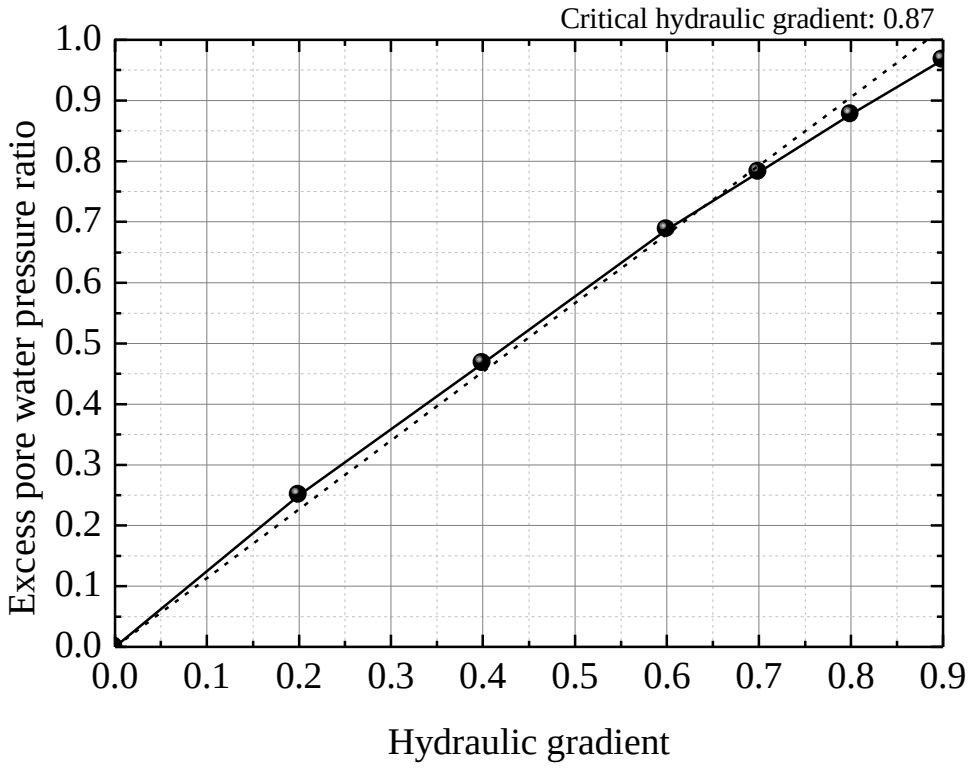

Figure 4.2 Variation of excess pore water pressure ratio with hydraulic gradient

Calvetti et al., 2004). In comparison to conventional shaking table tests, any desired initial effective stress can be easily achieved in the soil while keeping the soil bed stable.

Prior to the lateral loading experiments, the relationship between the hydraulic gradient and the excess pore water pressure ratio of the soil bed was confirmed. The critical hydraulic gradient of the soil bed was calculated as Eq. (3.2). This gives a critical hydraulic gradient in the present experiment of approximately 0.87. **Figure 4.2** shows the variation of the excess pore water pressure ratio with the hydraulic gradient. The ratio is defined as the excess pore water pressure normalized by the effective overburden pressure at each measuring point. Each value in the graph is the average of the ratios that were measured individually at the pore pressure transducers of PP2 ~ 18 (see **Figure 4.1**). The graph shows that the variation in excess pore water pressure ratio agrees well with that predicted theoretically based on the calculated critical hydraulic gradient, reaching 0.96 at $i = 0.9$.

Figure 4.3 shows the distribution of the excess pore water pressure ratio in the x-direction in the case of $H/D = 2.0$. Each value in the graph is the average of the ratios calculated at each horizontal position. The graph shows that the excess pore water pressure ratio increases with the hydraulic gradient and reaches approximately 1.0 at $i = 0.9$ that is roughly equal to the

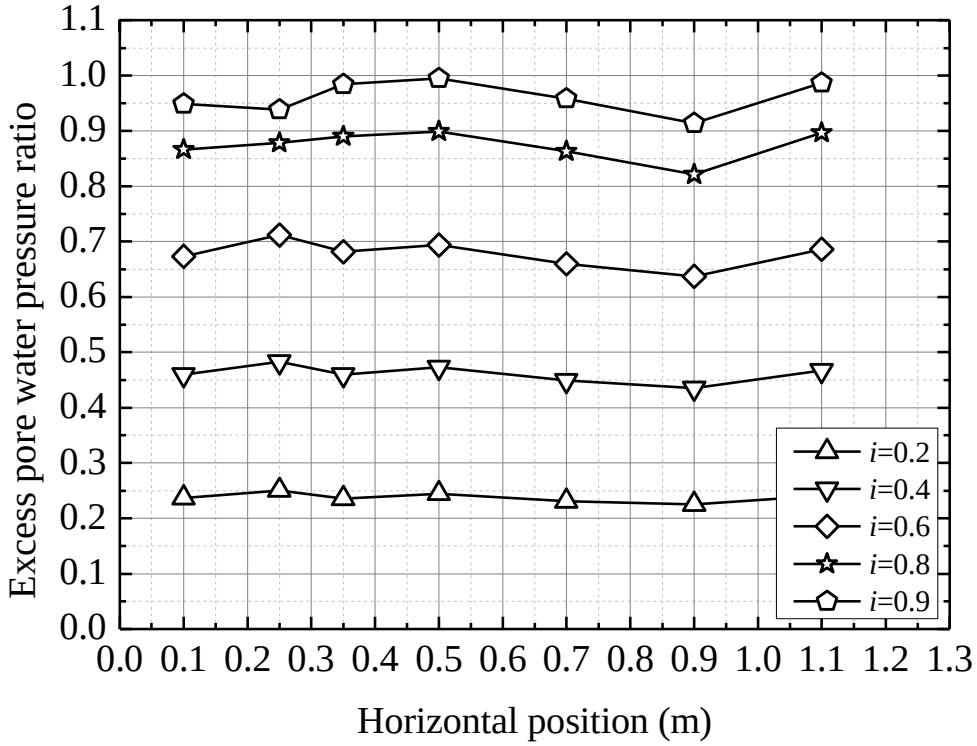

Figure 4.3 Horizontal distribution of excess pore water pressure ratio

critical hydraulic gradient. The ratio distributes uniformly in the *x*-direction in the soil bed. Judging from the above results, any desired initial effective stress of the soil can be achieved by sand boiling induced by the hydraulic gradient.

Loading method

The force-displacement curves could be obtained directly by measuring the resistive force while the pipe is being moved under displacement control. Although several experiments have to be carried out under different hydraulic gradient, the variation of the resistive force with the displacement can be followed simultaneously. However, the thrust force is a constant external force acting on a pipeline, and this load condition is totally different from that of displacement control. Therefore, to verify whether the relationships are equivalent, force-displacement relationships should be compared under two different loading methods: displacement control and load control.

Displacement-controlled experiments

In the displacement-controlled experiments, an electric actuator pulled the model pipe laterally with a loading rate of 1.0 mm/s after allowing the soil bed to stabilize for around ten minutes under the prescribed hydraulic gradient. The pipe and the actuator were connected by two stainless-steel wires whose diameter was 3.0 mm; no vertical restraint was applied to the pipe. The variations in the lateral resistive force and the excess pore water pressure of the soil were measured dynamically during loading.

The lateral loading was conducted for hydraulic gradient of i = 0.0, 0.2, 0.4, 0.6, 0.8, and 0.9 (≈ critical hydraulic gradient) in addition to dry conditions. There were two depths of soil cover—100 mm and 200 mm—giving a normalized depth H/D of either 1.0 or 2.0.

Load-controlled experiments

In the load-controlled experiments, a constant lateral load was applied to the model pipe by using a pulley and plumbs. The hydraulic gradient was gradually increased from 0.0 to 0.9 at 5-min intervals during the constant loading, and the lateral displacement of the pipe was measured. The weight of the plumbs was determined from the maximum resistive force

obtained from the displacement-controlled experiments at the critical hydraulic gradient.

According to the Design Guideline for Agricultural Pipelines (M.A.F.F., 2009), a thrust force acting on a pipe bend by internal water pressure is calculated as follows:

$$P_t = 2P_w A_c \sin\frac{\theta}{2} \tag{4.1}$$

where P_t is the thrust force (kN), P_w is the internal water pressure (kN/m^2), A_c is the cross-sectional area of the pipe (m^2), and θ is the angle of the pipe bend (^{o}). For instance, when the 100 kPa pressurized water flows through a 45^o pipe bend with 100 mm diameter, the calculated thrust force is approximately 0.6 kN. As shown in later section (4.3.1), 0.6 kN is corresponded to the lateral resistive force when the pipe displaces approximately 13 mm under the displacement control (H/D = 2.0). On the other hand, when the hydraulic gradient is 0.4 or more, the maximum resistive force is less than 0.6 kN. That is, the pipe keeps moving semi-permanently because the thrust force exceeds the lateral resistive force. Since the main aim of the present experiments is to obtain the force-displacement relationships considering liquefaction, the constant load was determined based on the maximum resistive force at the critical hydraulic gradient. Specifically, the plumb weight was 49.0 N and 98.0 N for the case of H/D = 1.0, and 98.0 N and 147.0 N for the case of H/D = 2.0.

4.3 Lateral Force-Displacement Relationship

4.3.1 Displacement-controlled experiments

Figure 4.4 shows the variations of the lateral resistive force with the lateral displacement in the displacement-controlled experiments. The measured force is scaled by the projected area of the pipe (0.1 m × 0.4 m = 0.04 m^2). Note that the frictional force between the walls of the container were subtracted from the calibration test conducted in water. The force-displacement curve for each hydraulic gradient shows a typical nonlinear relationship. The lateral resistive force increases more rapidly initially and then less so as the displacement progresses. As the hydraulic gradient increases, the resistive force decreases and the shape of the curves also changes. The initial tangential gradient decreases and the resistive force keeps increasing with the lateral displacement. At the critical hydraulic gradient ($i \approx 0.9$), the resistive

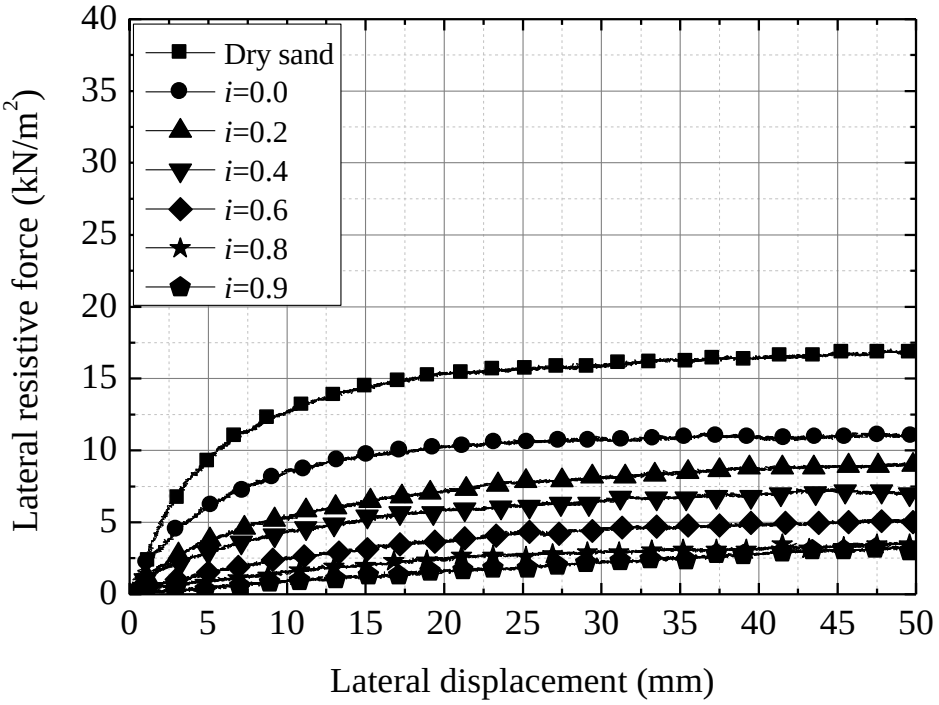

(a)

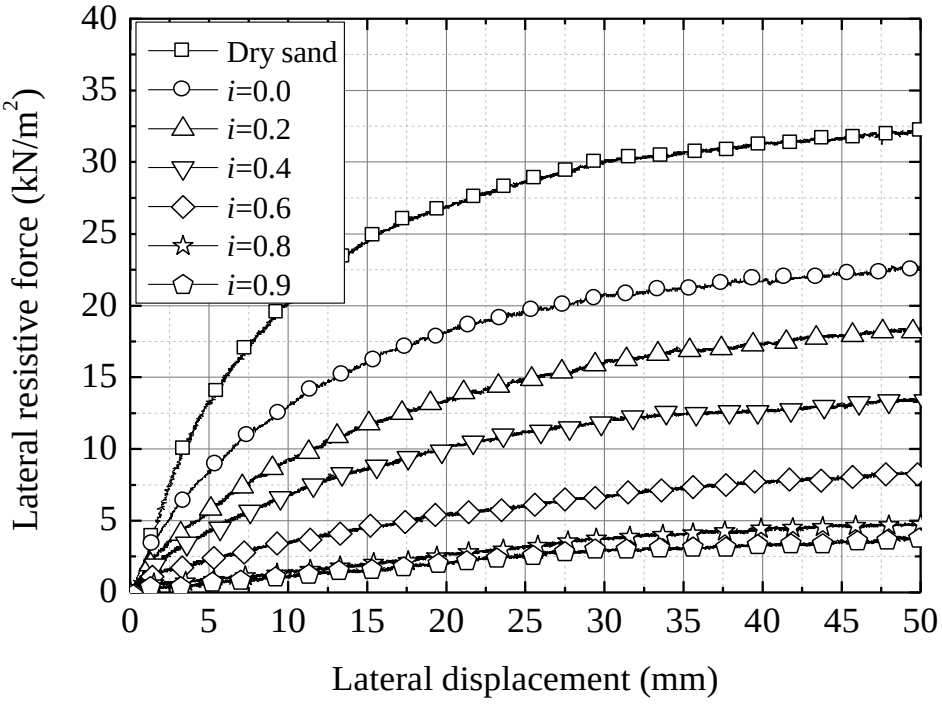

(b)

Figure 4.4 Force-displacement curve:
(a) H/D = 1.0 and (b) H/D = 2.0

force is almost zero at the very beginning of the loading, indicating that the surrounding soil lost its resistive force due to liquefaction. However, the resistive force at a displacement of 50 mm is roughly equal to that for $i = 0.8$ even though the soil bed is almost liquefied. In addition, when comparing two cases with different depths of soil cover, the lateral displacement until the resistive force reaches a constant value is smaller in the case of $H/D = 1.0$ than that of 2.0.

4.3.2 Load-controlled experiments

The experimental results of the load-controlled experiments are compared with those of the displacement-controlled experiments to verify whether the force-displacement relationships are equivalent under two different loading methods. **Figure 4.5** shows the variations of the lateral displacement of the pipe and the excess pore water pressure ratio in the load-controlled experiments. Note that the excess pore water pressure ratio is the average value calculated from the excess pore water pressure measured at PP2-18 (see **Figure 4.1**). **Figure 4.5** shows that the pipe starts to move laterally immediately after the excess pore water pressure is raised. The lateral displacement of the pipe increases rapidly once the excess pore water pressure ratio exceeds 0.8. Once it exceeds 0.9, the pipe continues to move even though the excess pore water pressure remains constant. The lateral speed of the pipe calculated from the lateral displacement and the measuring time varied in the range of 1.0 ~ 5.0 mm/s.

Figure 4.6 shows the variations of the excess pore water pressure ratio with the lateral displacement of the pipe. The results of the displacement-controlled experiments are also plotted in the graphs for comparison. The lateral displacement in the displacement-controlled experiments is the displacement of the pipe when the lateral resistive force is matched by the weight of the plumb. The graphs indicate clearly that the pipe starts to move appreciably when the excess pore water pressure ratio exceeds 0.8, as also shown in **Figure 4.5**. The results of the load-controlled experiments correspond reasonably well with those of the displacement-controlled experiments, regardless of the depth of soil cover and the weight of the plumb. This fact implies that the force-displacement relationship under constant load is equivalent to that under constant displacement. Hence, the following discussion about the force-displacement relationship will be based on the results of the displacement-controlled experiments.

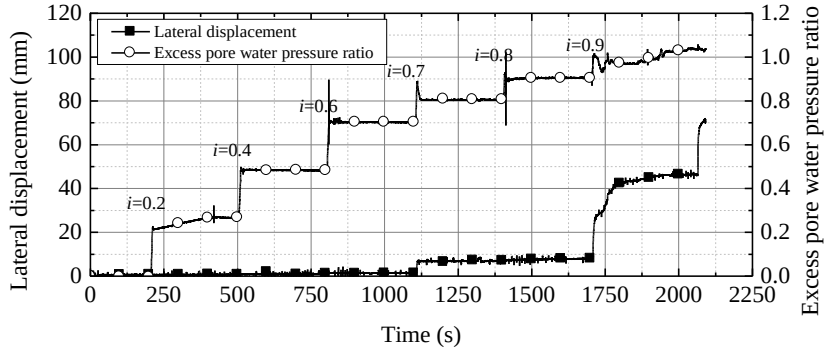

(a)

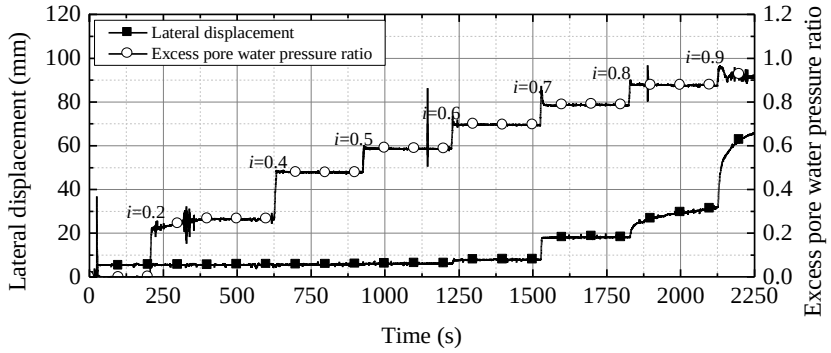

(b)

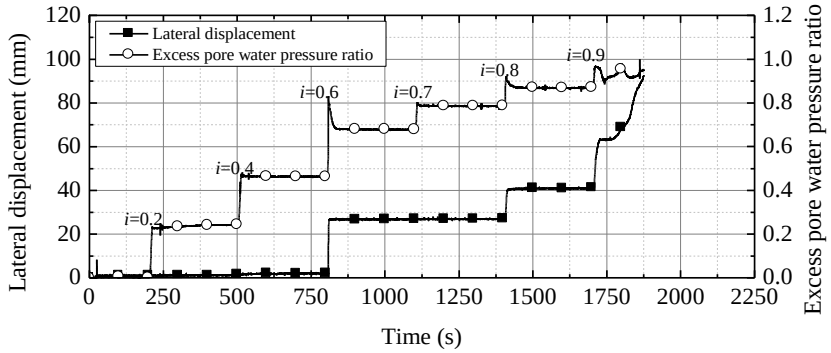

(c)

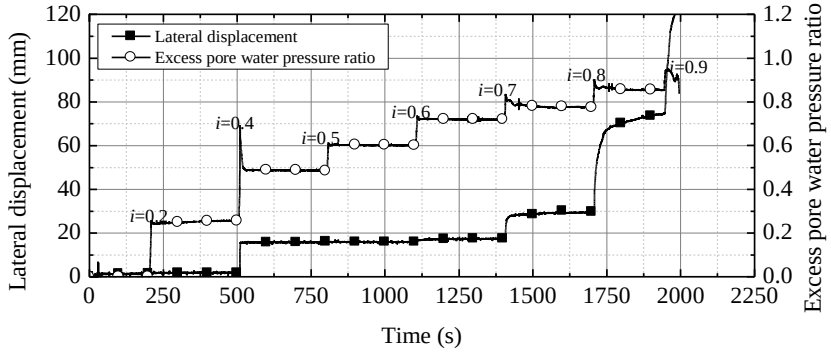

(d)

Figure 4.5 Variation of lateral displacement and excess pore water pressure ratio:

(a) *H/D* = 1.0, 49 N, (b) *H/D* = 1.0, 98 N, (c) *H/D* = 2.0, 98 N, and (d) *H/D* = 2.0, 147 N

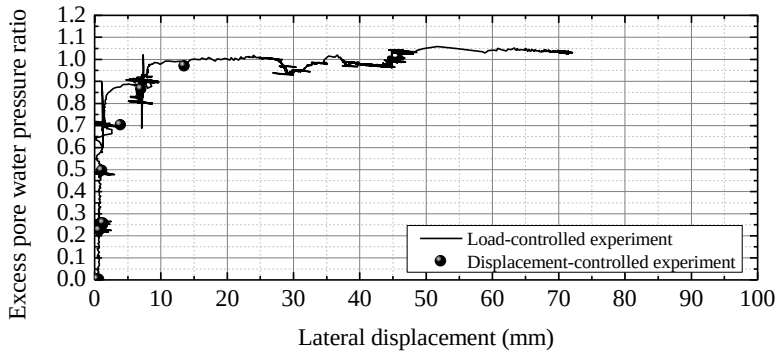

(a)

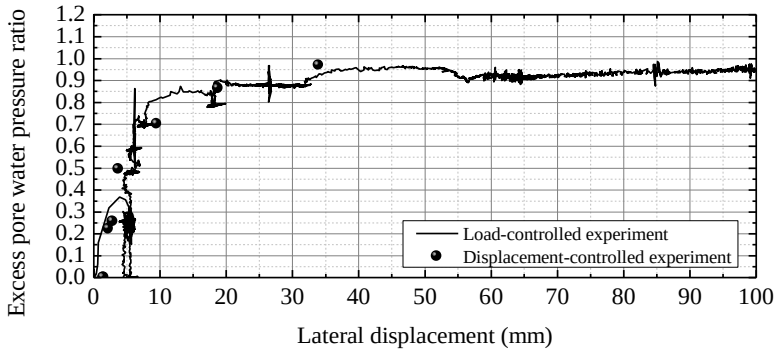

(b)

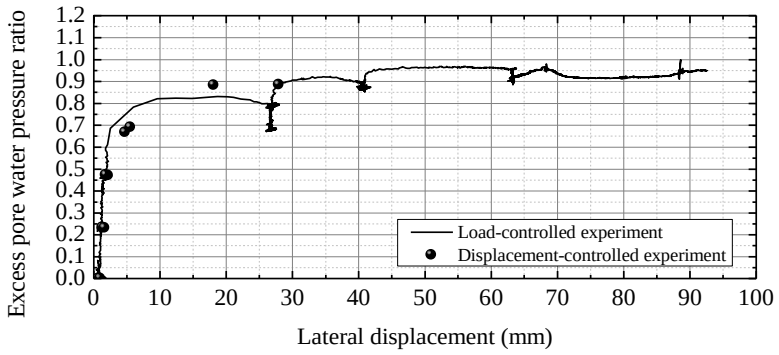

(c)

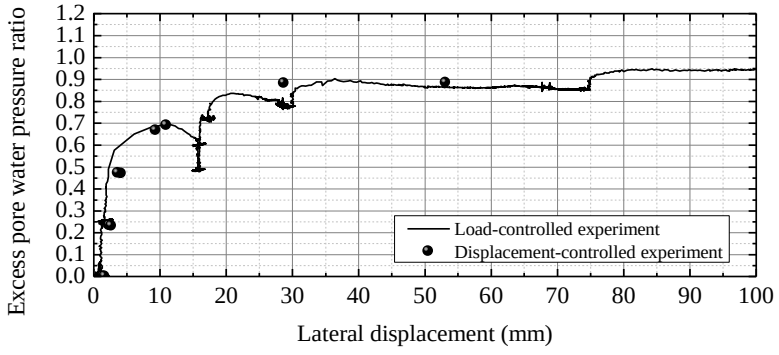

(d)

Figure 4.6 Variation of excess pore water pressure ratio with lateral displacement:

(a) *H/D* = 1.0, 49 N, (b) *H/D* = 1.0, 98 N, (c) *H/D* = 2.0, 98 N, and (d) *H/D* = 2.0, 147 N

4.4 Interaction between Displacement of Pipe and Sand

4.4.1 PIV analysis

Characteristics of soil strength appear in its failure mechanism. Effective countermeasures can only be taken after accurately understanding the failure mechanism. In this subsection, the movement characteristics of the surrounding soils due to the displacement of the pipe are tried to elucidate by using PIV (Particle Image Velocimetry) analysis. In PIV analysis, the moving vector of the target pixel can be obtained by the variation of the luminance between consecutive images. Image processing system "Flow-vec" (Library, Inc.) can calculate velocity, angle, vorticity, divergence, and turbulent energy. This packaged software supports the concentration correlation method and realizes the high speed processing by adopting an optimized algorithm. For details, refer to Kaga et al. (1994) and Kimura et al. (1992). The consecutive images were extracted every 2.0 s (2.0 mm in displacement) from the video shot of the front of the model. Other parameters are summarized in **Table 4.2**.

Dry sand

As a first step, PIV analysis was performed for the dry sand with different dry density to observe the failure mechanism under simple condition. **Figure 4.7** shows the variation of the lateral resistive force with relative density of 50% and 80%. The normalized depth *H/D* is 2.0. The graph indicates that the resistive force of the dense sand is obviously large, and the resistive force reaches the peak value when the displacement is approximately 11 mm.

On the basis of the variation of the lateral resistive force, the distributions of the vector are shown in **Figures 4.8** and **4.9** for a lateral displacement of 4.0 mm, 8.0 mm, 12.0 mm, and 15.0 mm. In these figures, the velocity vector and the contour map are overlaid. The figures reveal that the deformation mechanism of the soil is greatly different depending on the soil density. First, the movement range on the passive side is larger in the dense sand. This difference is due to the small volume change of the soil because of the low void ratio. Subsequently, a clear slip surface is observed at a displacement of 12.0 mm. This displacement roughly agrees with the displacement that the resistive force reaches maximum value (see **Figure 4.7**). That is, the resistive force increases nonlinearly in the compression process of the soil, and then the

Table 4.2 Parameters for PIV analysis

Grid interval (pix)	15
Search interval (pix)	21
Ratio of valid pixel	0.5
Minimum value of average luminance	10
Maximum value of valid luminance	250
Minimum value of valid luminance	5

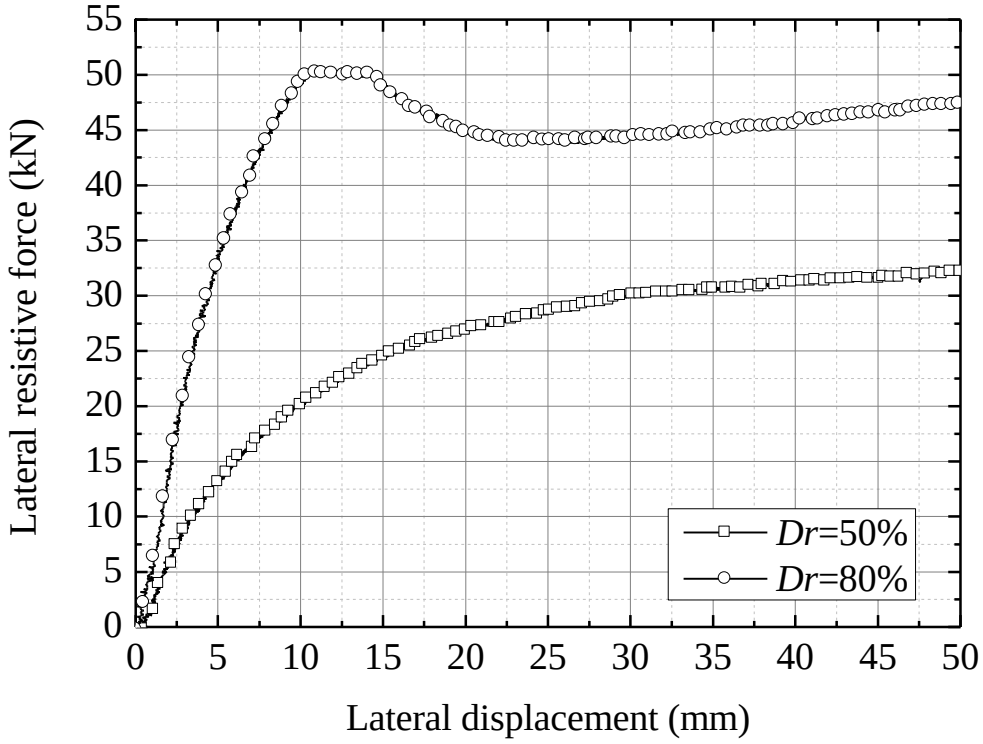

Figure 4.7 Force-displacement curve with different relative density

resistive force greatly drops due to the shear failure. This trend is similar to a general element test (e.g. uniaxial compression test). The difference in the soil density (void ratio) appears as a time lag of the above mechanism. On the other hand, in a loose sand, no clear peak is observed because the compression process occupies a large proportion. Therefore, the slip surface is difficult to appear.

The soil above the buried pipe is hardly moving regardless of the soil density. Audibert et al. (1974) called this area as “central wedge”. The authors revealed that this failure mechanism was observed at relatively shallow burial depth. Furthermore, the inclination of the

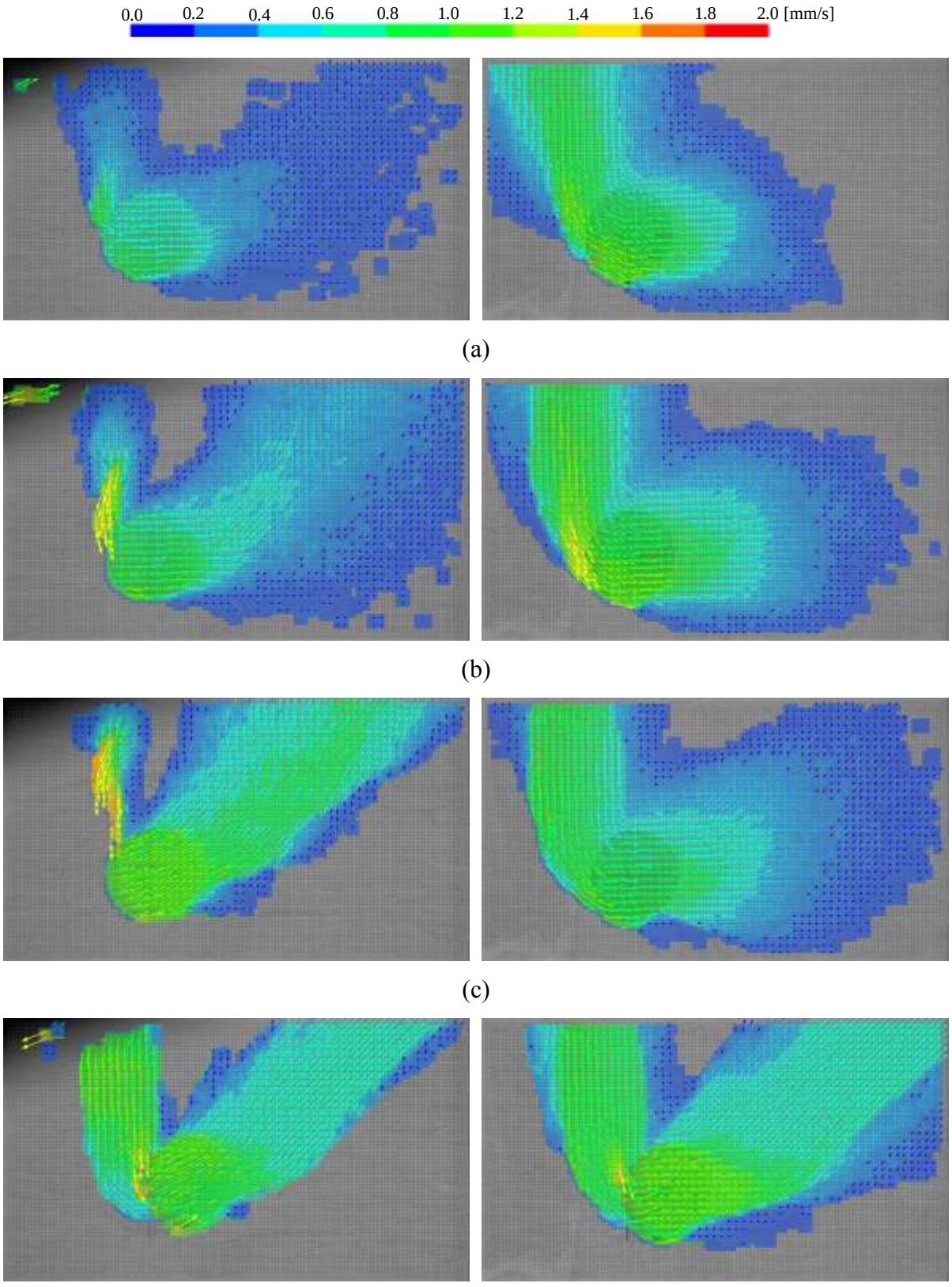

Figure 4.8 Velocity vector (D_r = 80%): (a) 4.0 mm, (b) 8.0 mm, (c) 12.0 mm, and (d) 50.0 mm

Figure 4.9 Velocity vector (D_r = 50%):

slip surface is clearly larger in the dense sand than in the loose sand. In consideration of the passive earth pressure acting on a retaining wall, the angle of the sip surface decreases as the internal friction angle increases. The reason why the opposite phenomenon occurred is due to the constraint condition of the pipe. In other words, the pipe is liable to float as it receives a larger resistive force because the pipe is not restrained in the vertical direction. As a result, it is inferred that the angle of the slip surface increased. This mechanism can be explained in a numerical analysis.

Judging from **Figure 4.8 (c), (d)**, the position of the slip surface does not move even when the pipe displaces 38.0 mm. This result indicates that once the slip surface is determined, the soil on the passive side displaces along it. This is a crucial clue for determining the area to be countermeasured.

Saturated sand

In a similar manner, the distributions of the vector at i = 0.0 and i = 0.8 are shown in **Figures 4.10** and **4.11**, respectively. Note that the accurate vector could not be measured at the critical hydraulic gradient (i = 0.9) because of the severe upward seepage at the front wall. **Figure 4.10** indicates that the deformation mechanism at i = 0.0 has no large difference from that in dry sand with the same density (see **Figure 4.8**). In contrast, the deformation behavior of the soil at i = 0.8 is fairly characteristic. The displacement range of the passive side at a displacement of 4.0 mm is narrow and the soil moves over the pipe toward the active side (left side) of the pipe. The soil bed shows a liquid-like flow due to the decrease of the effective stress with the increase of the hydraulic gradient. Subsequently, although the movement range of the soil expands with the displacement of the pipe, the large spiral flow of the passive side soil does not change. Even at a displacement of 50.0 mm, the distribution of the velocity vector has no large difference compared with that at 12.0 mm, and the slip surface does not develop clearly. Considering the results of the dense sand and loose sand in addition to the above results, the increase in the resistive force even at high hydraulic gradient as shown in **Figure 4.4** can be explained.

The mechanism of the development of the resistive force could be visually understood using PIV analysis. The variation of the resistive force depends mainly on the failure

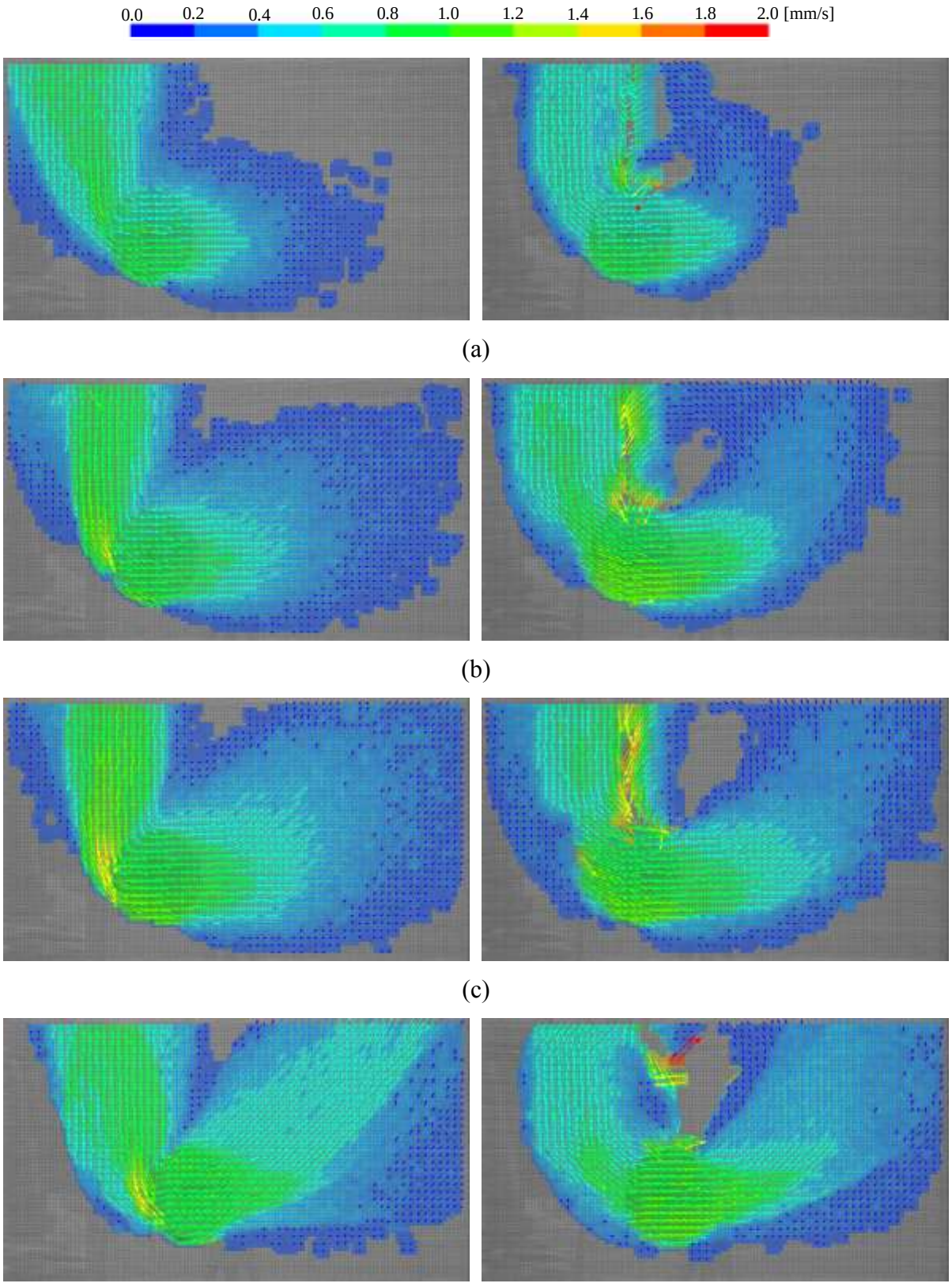

Figure 4.10 Velocity vector (i = 0.0): **Figure 4.11** Velocity vector (i = 0.8): (a) 4.0 mm, (b) 8.0 mm, (c) 12.0 mm, and (d) 50.0 mm

mechanism of the passive side soil, and two deformation patterns are clearly observed. On the other hand, moving vector shows the fluid like behavior of the soil as the effective stress decreases. In this state, a clear slip surface could not be confirmed, and this fact caused steady increase in the resistive force.

4.4.2 Profile of ground surface

Figure 4.12 shows the profile of the ground surface after the pipe displaced 100 mm in the case of H/D = 2.0. The vertical displacement is the variation from the initial value that was measured just before the lateral loading. In the graph, the right side of the pipe is positioned at 500 mm. The graph reveals that the soil on the passive side of the pipe is greatly lifted up. The upheaval of the soil is the largest in the dry sand and decreases as the hydraulic gradient rises. This upheaval on the passive side is one of the reason that the lateral resistive force kept increasing with the lateral displacement (see **Figure 4.4**). In contrast, the soil on the active side of the pipe settled, and the settlement decreases as the hydraulic gradient is raised. This is attributed to the fact that the hole on the active side was backfilled by the collapse of the

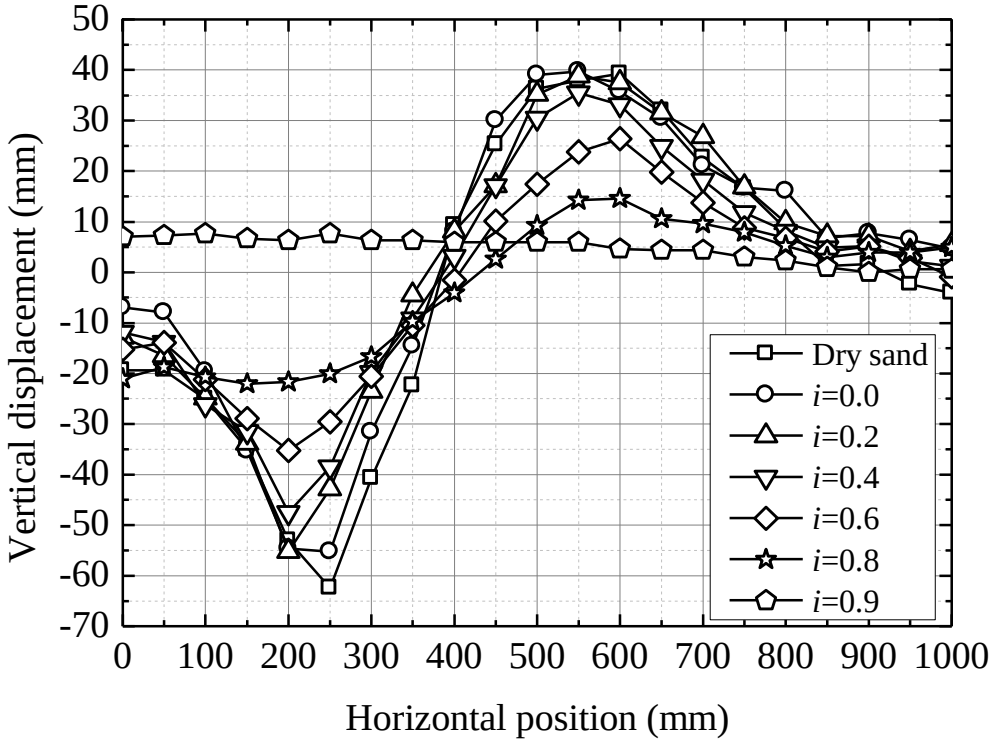

Figure 4.12 Profile of ground surface (H/D = 2.0)

upheaved sand pushed out by the pipe. When the hydraulic gradient was high, that is, when the effective stress of the soil decreased, the backfilling was likely to occur because the angle of the internal friction of the soil bed decreased. Moreover, when comparing the variation of the upheaval and the settlement of the soil, the amount of the settlement is slightly larger than that of the upheaval. This result means that the passive-side soil displaced with the slight compression.

The profile of the ground surface at $i = 0.9$ (critical hydraulic gradient) largely differs from the others. At $i = 0.9$, neither uplift nor settlement of the soil is observed. This means that the response of the liquefied sand is totally different from that of the saturated sand. This result is one of the evidence that the soil at the critical hydraulic gradient behaves as a liquid. This tendency was the same in the other cases having different depth of soil cover.

4.4.3 Variation of excess pore water pressure

To evaluate the stress state of the entire soil bed during the lateral loading, contour diagrams of the excess pore water pressure ratio in the case of $H/D = 2.0$ are shown in **Figures 4.13** and **4.14**. The excess pore water pressure ratio is calculated from the excess pore water pressure and the initial effective overburden pressure, and is the increment from the initial value. Each black dot in the contour diagrams shows the measuring points.

At the hydraulic gradient of 0.0, the contour diagram reveals that the excess pore water pressure rises on the upper-right side of the pipe with the lateral displacement (see **Figure 4.13 (a)**). This increment is due to the compression of voids and the negative dilatancy of the relatively loose sand. As also shown in the results of PIV analysis (see **Figure 4.10**), the contour diagram shows that the soil on the passive side displaces diagonally upward direction with the displacement of the pipe. Second, the raised excess pore water pressure dissipates from the side close to the pipe (see **Figure 4.13 (b)**). This dissipation is due to the increase of the permeability by the large deformation of the soil around the pipe. The raised excess pore water pressure further dissipates, and it decreases to zero (initial value) in the wide range when a displacement is 25.0 mm (see **Figure 4.13 (c)**). Once the pipe moves by 50.0 mm, the excess pore water pressure in the soil surrounding the pipe decrease to the negative value (see **Figure 4.13 (d)**).

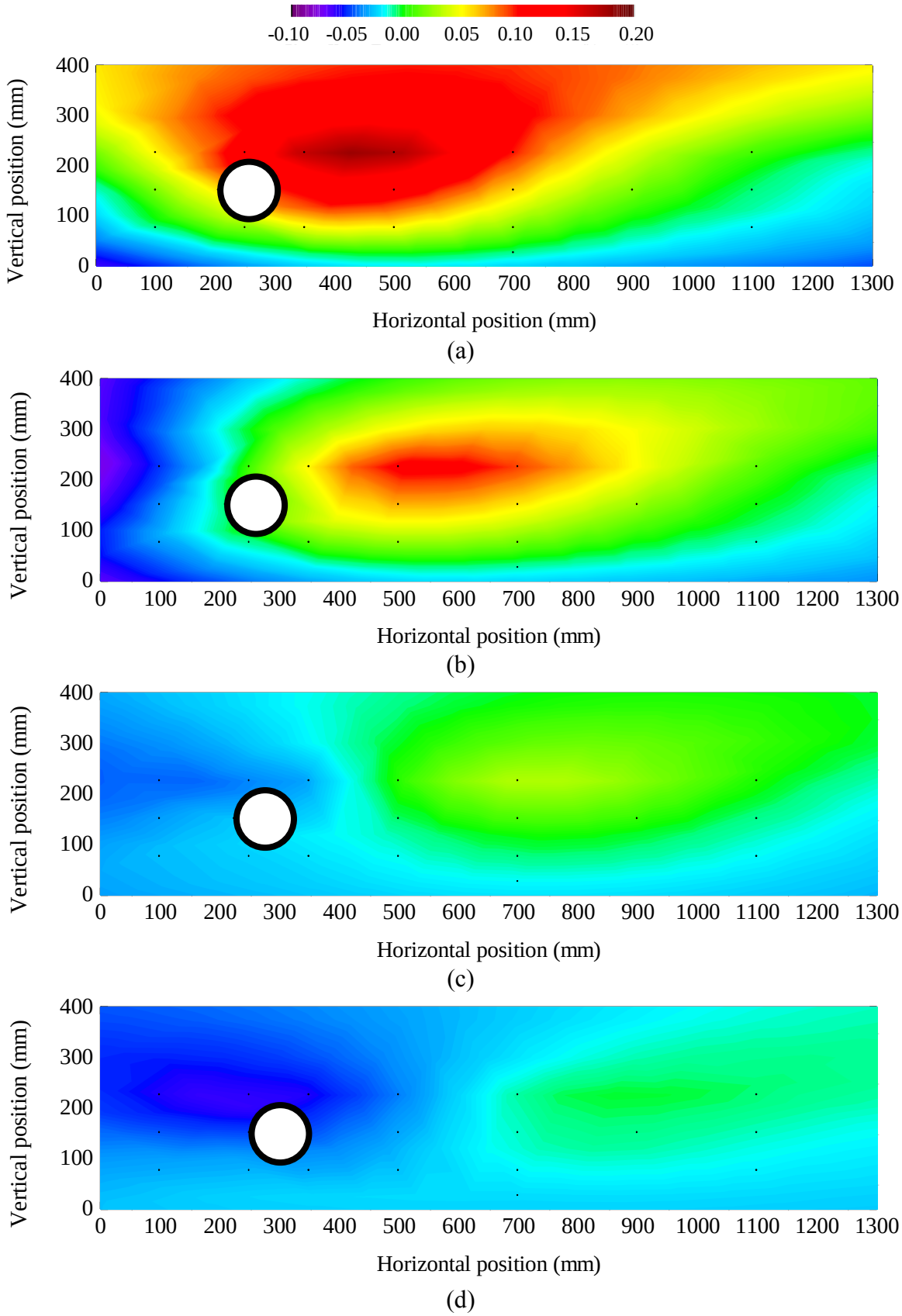

Figure 4.13 Distribution of excess pore water pressure ratio (i = 0.0): (a) 2.5 mm, (b) 5.0 mm, (c) 25.0 mm, and (d) 50.0 mm

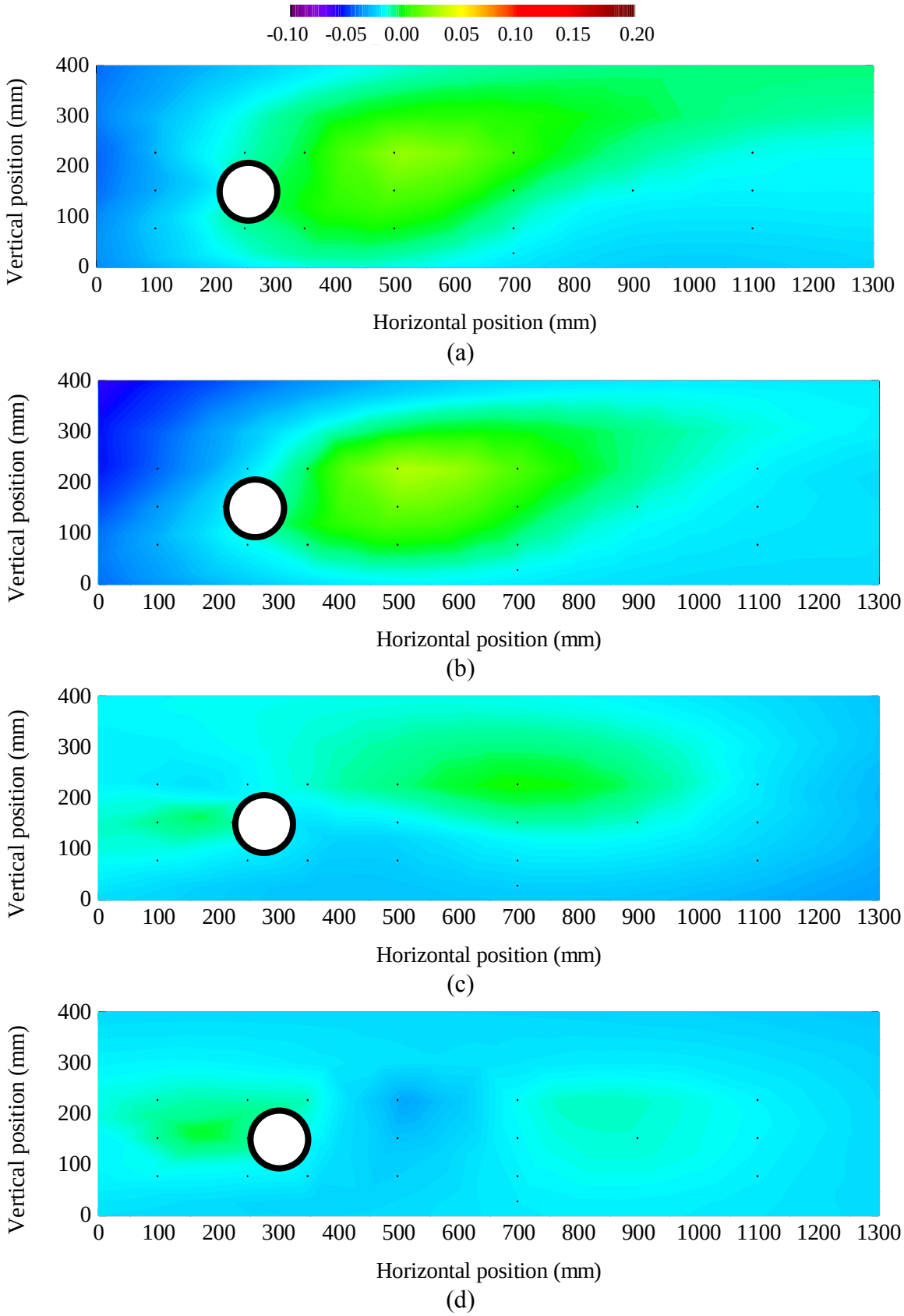

Figure 4.14 Distribution of excess pore water pressure ratio (i = 0.9): (a) 2.5 mm, (b) 5.0 mm, (c) 25.0 mm, and (d) 50.0 mm

In other words, the effective stress of the soil around the pipe recovers because of the large displacement of the pipe. The comparison with the PIV results tells us the fact that the distribution of the excess pore water pressure is different around the slip surface. The excess pore water pressure on the left side from the slip surface greatly decreases.

In contrast, at the hydraulic gradient of 0.9, the increment of the excess pore water pressure on the passive side of the pipe is relatively small, and the variation in the entire soil bed is small. The variation of the excess pore water pressure is largely depending on the initial hydraulic gradient: the increment becomes large, as the hydraulic gradient is low. This characteristic can be explained from the relationship between the total stress, the effective stress, and the excess pore water pressure.

4.4.4 Apparent viscosity of liquefied sand

Several geotechnical researchers have focused on the rate dependence of the resistive force of the liquefied soil based on the hydrodynamics. For instance, Miyajima et al. (1994) and Towhata et al. (1999) calculated the apparent viscosity coefficient of liquefied soil according to the following calculation procedure.

First, Reynolds number is defined as the following equation when a column is placed in the fluid. Reynolds number is the ratio of inertia force to viscous force.

$$R_e = \frac{\rho V D}{\eta} \tag{4.2}$$

where ρ is the density of the saturated sand (kg/m^3), V is the velocity of the pipe (m/s), D is the diameter of the pipe (m), and η is the coefficient of viscosity (kPa s). The drag force acting on the column is calculated as follows with using the drag coefficient:

$$F_D = \frac{1}{2} C_D V^2 D L \rho \tag{4.3}$$

where C_D is the drag coefficient and L is the length of the pipe (m). According to the Lamb's equation (Lamb, 1911), the drag coefficient applying on the column in the fluid is a function of Reynolds number only:

$$C_D = \frac{8\pi}{R_e\left(2.002 - \ln\left(R_e\right)\right)} \tag{4.4}$$

Therefore, the relationship between the resistive force (drag force) and the coefficient of viscosity can be obtained by substituting Eq. (4.4) into Eq. (4.3):

$$F_D = \frac{4\pi\eta VL}{2.002 - \ln\left(\rho VD/\eta\right)} \tag{4.5}$$

By substituting the measuring resistive force into Eq. (4.5), the coefficient of viscosity can be back calculated.

The coefficient of apparent viscosity was calculated from the experimental data obtained from the present experiment and the small-scale experiment written in Chapter 3. In the load-controlled experiments, assuming that the weight of plumb was equivalent to the resistive force, the weight of plumb and the moving rate of the pipe were used for the calculation. On the other hand, in the displacement-controlled experiment, the lateral resistive force increases rapidly right after the loading start and keeps increasing as shown in **Figure 4.15**. The first sudden increase in the resistive force was defined as the resistive force of the liquefied sand. **Table 4.3** summarizes the calculated coefficient of apparent viscosity. The calculation

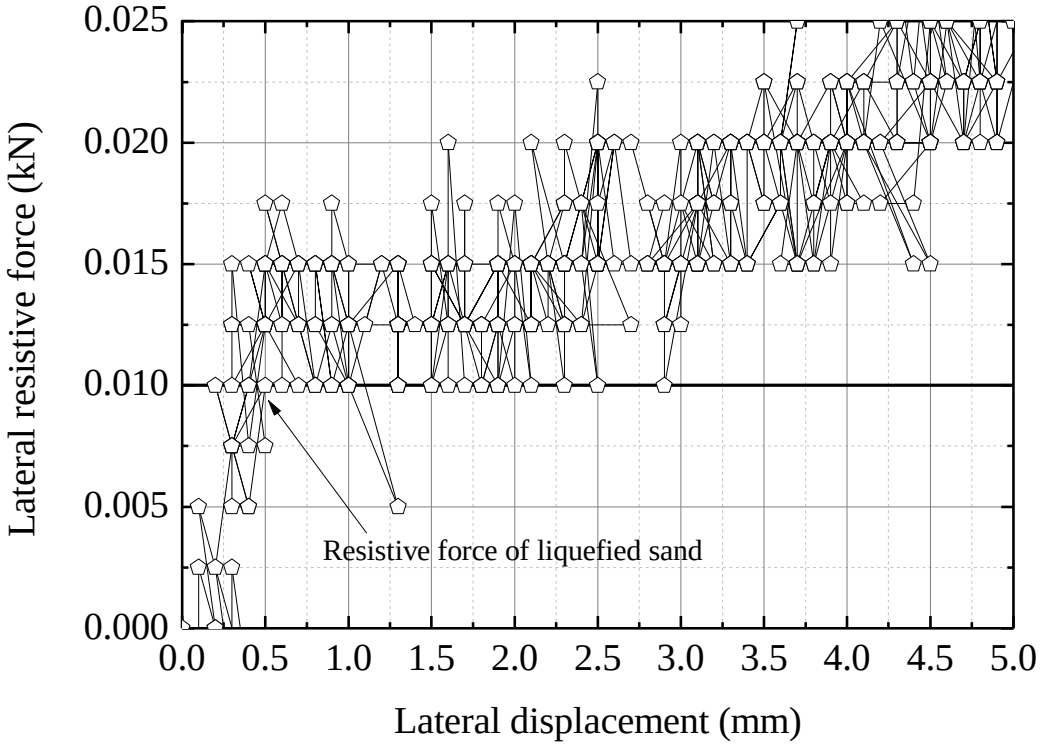

Figure 4.15 Force-displacement curve at i = 0.9 (enlarged view of **Figure 4.4 (b)**)

Table 4.3 Apparent viscosity of liquefied sand

Loading method	*H/D*	Velocity of pipe (mm/s)	Resistive force (N)	Apparent viscosity (kPa s)
Displacement control	3.5	0.1	2	145.0
		1.0	5.2	10.7
		5.0	7.0	6.4
		10.0	12.0	5.1
		15.0	11.0	2.8
		20.0	11.0	2.0
Displacement control	1.0	1.0	12.5	27.6
	2.0		10.0	35
Load control	1.0	12.0	49	8.3
		2.0	98	145.1
	2.0	3.0	98	91.1
		4.0	147	101.1

results varies widely in the range of 1.0 ~ 100 kPa s. The apparent viscosity tends to become large as the moving speed of the pipe is slow. According to the results shown by Towhata et al. (1999), the apparent viscosity of the liquefied sand was summarized as 0.45 ~ 2.16 kPa s. In comparison with those, the present results include extremely large value. This difference is attributed to the about 20% larger relative density of the soil bed and the non-homogeneity of the liquefied sand bed.

4.5 Thrust Restraint by Gravel and Geogrid

4.5.1 Outline of model experiment

This section verifies the effectiveness of the thrust restraint using gravel and geogrid during liquefaction. The attention of the experiment is focused on revealing the reinforcement mechanism of the countermeasure for determining the effective substituting area (width and height) of gravel in the cross section. After examining the effectiveness of gravel as the liquefaction countermeasure, the reinforcement effect of a combination method of gravel and

geogrid is investigated.

Pictures of the gravel and the geogrid are shown in **Figures 4.16** and **4.17**, respectively. The size of the gravel was selected in consideration of the size ratio with the model pipe. Approximately single-sized gravel (S-5) having a particle size range from 2.5 mm to 5.0 mm was used. The dry density of the gravel bed was approximately 1.50 g/cm^3, which was slightly larger than that of the sand bed. For geogrid, NETLON sheet Z20 (Mitsui Kagaku Sanshi, Inc.) was used. The mesh size of the geogrid was 6.0 mm in both vertically and horizontally. This geogrid was made of polyethylene, and its design tensile strength was 4.0 kN/m. The characteristics of this type of geogrid (e.g. lightweight, rust prevention, integral molding, cold resistance) are suitable for use as a thrust countermeasure. Its mesh structure is also advantageous to dissipate the excess pore water pressure immediately. Moreover, by using it together with gravel, the integration effect and the increase in the resistive force are expected.

Figure 4.18 illustrates the backfill conditions. The case of the homogeneous sand is called Type-A. In Type-B, the square area (2*D*) surrounding the pipe is substituted by the gravel. On the basis of the PIV results that there was almost no movement of the soil on the active side of the pipe during lateral movement, two cases extending the substitution width to the passive side are carried out. In Type-W1, the width is extended by 50 mm from Type-B, and by 100 mm in Type-W2. On the contrary, in Type-H1, the substitution height is extended from Type-B toward the ground surface. In Type-H2, the base of the pipe is sand. For the two cases of Type-B and H2, the gravel area is integrated by the geogrid.

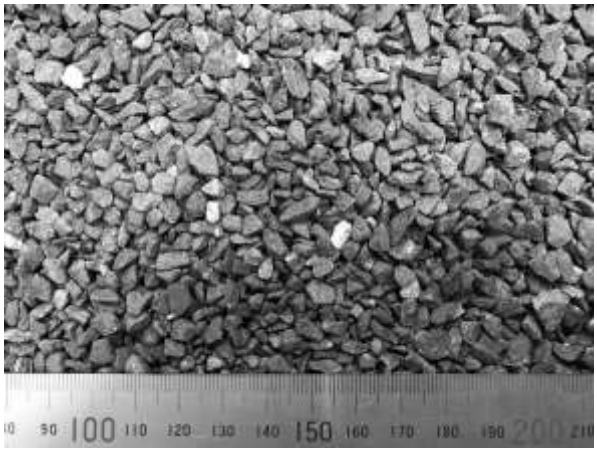

Figure 4.16 Picture of gravel (S-5)

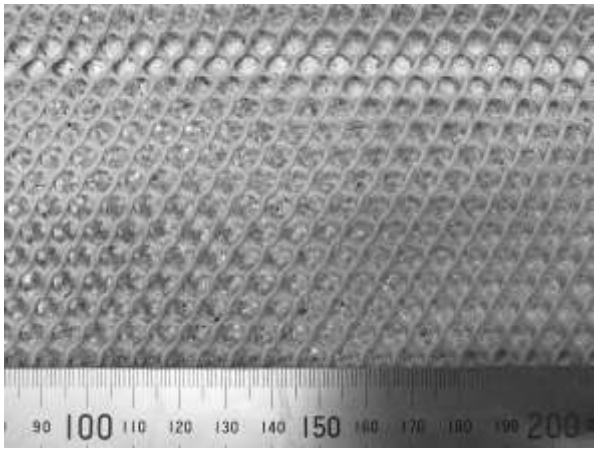

Figure 4.17 Picture of geogrid (Z-20)

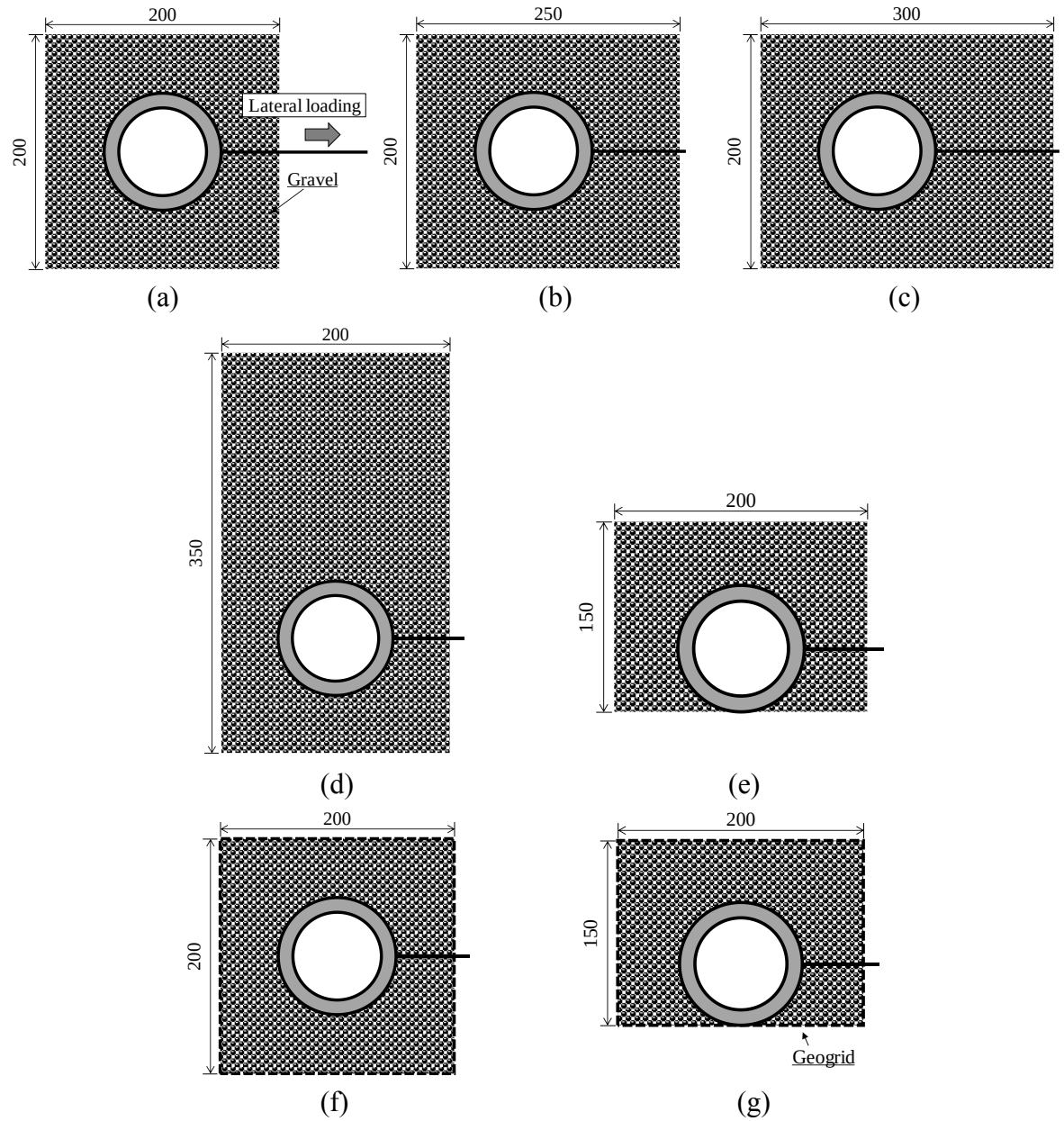

Figure 4.18 Backfill conditions: (a) Type-B, (b) Type-W1, (c) Type-W2, (d) Type-H1, (e) Type-H2, (f) Type-B_G, and (g) Type-H2_G

4.5.2 Dissipation effect of excess pore water pressure

Figure 4.19 shows the variation of the excess pore water pressure ratio with the hydraulic gradient in the process of increasing the hydraulic gradient. The calculation method of the excess pore water pressure ratio is the same as **Figure 4.2**. The excess pore water pressure ratio increases almost linearly in the homogeneous sand (Type-A), while the increase in the other cases (Type-B, W1, W2, H2) is slow. The decline rate from the homogeneous sand is

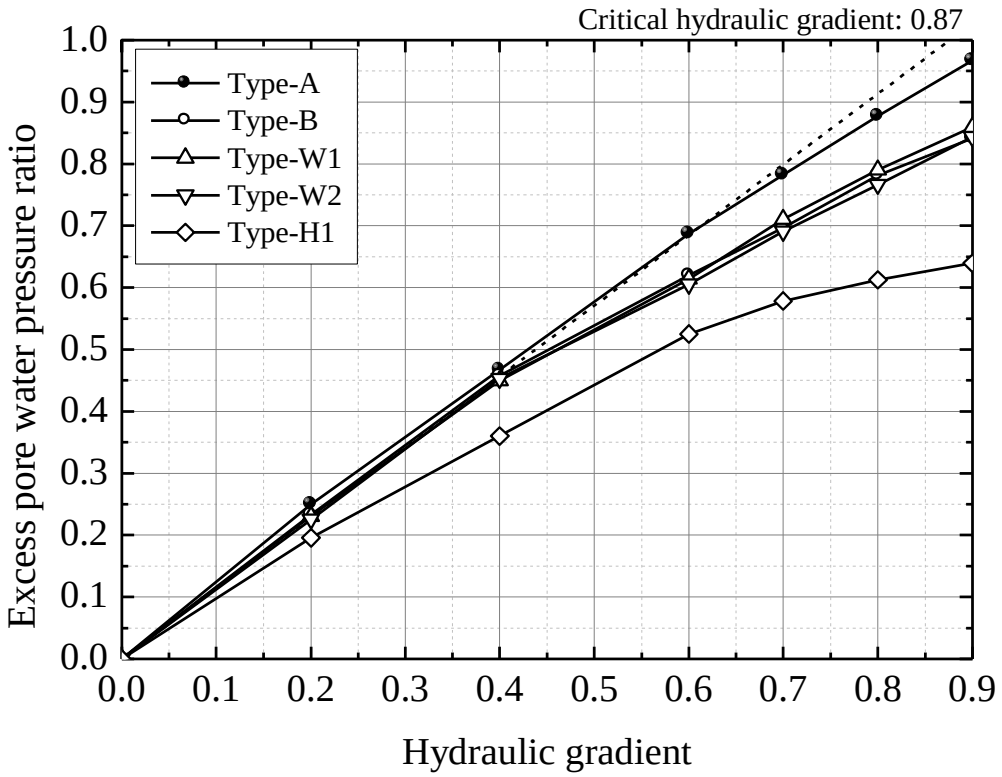

Figure 4.19 Variation of excess pore water pressure ratio with hydraulic gradient

approximately 10%. Note that the difference of the substitution range of the gravel has little influence on the variation of the ratio during the process of increasing the hydraulic gradient. The graph also reveals that the dissipation effect of the excess pore water pressure can be observed when the hydraulic gradient is 0.4 or more (excess pore water pressure ratio is 0.5 or more). Therefore, we can judge that the excess pore water pressure ratio is reduced 10% by substituting with gravel when the excess pore water pressure ratio is 0.5 or more.

Only in Type-H1, the increase in the ratio is suppressed from the early stage when the hydraulic gradient is low. Although this is a desirable result, large settlement of the pipe was observed due to the concentration of the upward seepage into the gravel area. It is not preferable to directly compare the lateral resistive force in Type-H1 with other cases because the burial condition is significantly different.

4.5.3 Effectiveness of substitution of gravel

The result of Type-B (the square area surrounding the pipe is buried with the gravel)

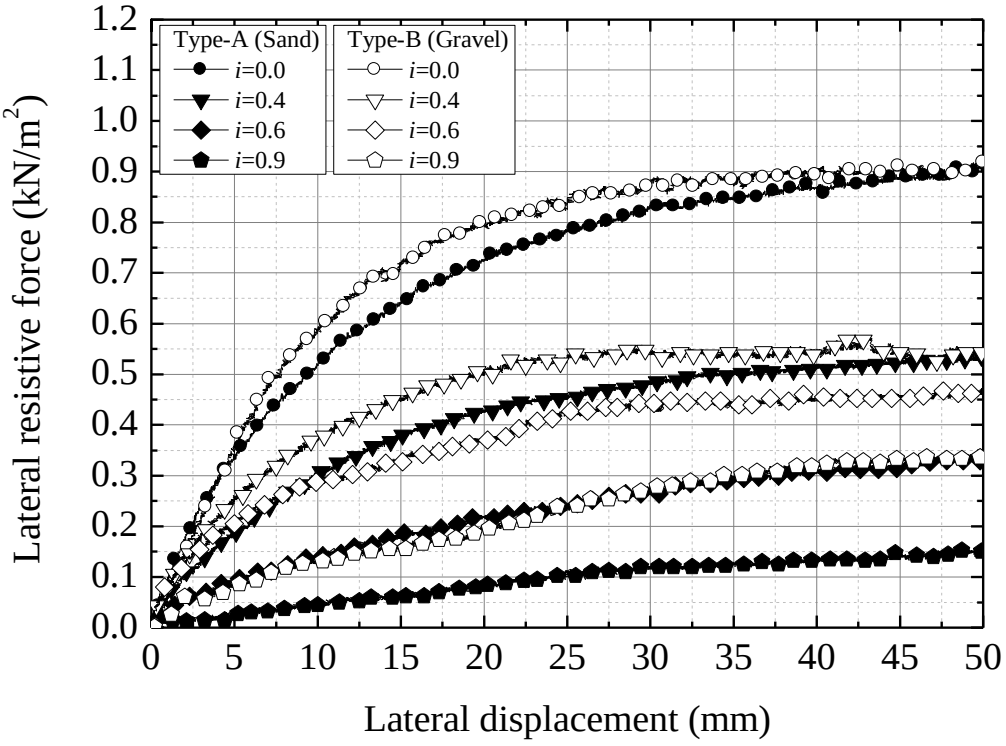

Figure 4.20 Force-displacement curve in Type-A and Type-B

is shown to verify the effectiveness of the substitution of the gravel on the lateral resistive force. **Figure 4.20** shows the variation of the lateral resistive force with the lateral displacement in Type-A and Type-B. Although two curves at i = 0.0 are not different so much, the difference widens as the hydraulic gradient increases. The results of Type-B can be categorized into two groups based on the initial resistive force: the group that the hydraulic gradient is 0.4 or less and 0.6 or more. Since the suppressing effect of the rise in the excess pore water pressure is confirmed from i = 0.6 or more (see **Figure 4.19**), **Figure 4.20** shows that the initial resistive force increases due to the suppression of the decrease of the effective stress.

4.5.4 Influence of substitution range of gravel

Figure 4.21 shows the variation of the lateral resistive force with the lateral displacement at i = 0.0 to examine the influence of the substitution range of the gravel on the lateral resistive force. The resistive force largely increases with widening the gravel area to the passive side of the pipe, while the height of the gravel zone does not greatly contribute to the

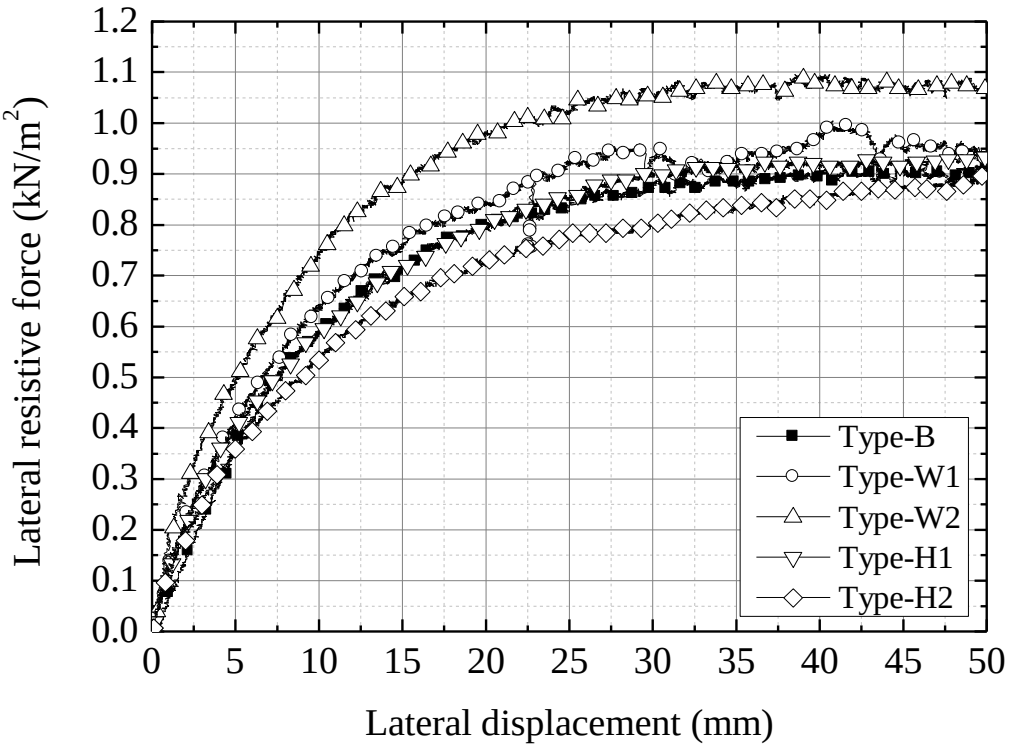

Figure 4.21 Force-displacement curve at i = 0.0 in Type-B, W1, W2, H1, H2

increase in the resistive force. When the base of the pipe is sand (in Type-H2), the resistive force is the same or less than that of Type-B. This difference may be due to the shear resistive force of the soil at the lower right part of the pipe because slight compression and displacement of the soil at this part was observed in PIV analysis (see **Figure 4.10**). Even in Type-H1, the increase in the resistive force is small.

The contour diagrams of the excess pore water pressure ratio in Type-B and Type-W2 are shown in **Figures 4.22** and **4.23**, respectively, to identify the reason why the resistive force increased by expanding the substitution width of the gravel. The definition of the calculation is the same as **Figure 4.13**. The results of the initial stage (Y = 5.0, 10.0 mm) are compared because the resistive force increased from the beginning of the lateral loading.

First, the excess pore water pressure ratio on the upper-left part of the pipe increases extremely as the pipe moves (Y = 5.0 mm) although the ratio is smaller than that of the homogeneous sand as shown in **Figure 4.13**. Furthermore, we can observe the variation of the ratio depending on the width of the gravel by comparison between **Figures 4.22** and **4.23**. The excess pore water pressure raised by the compression of the void (negative dilatancy) dissipates

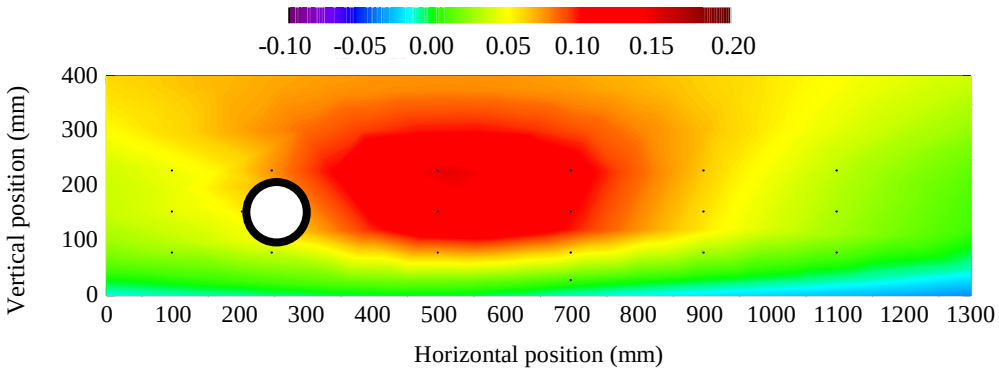

(a)

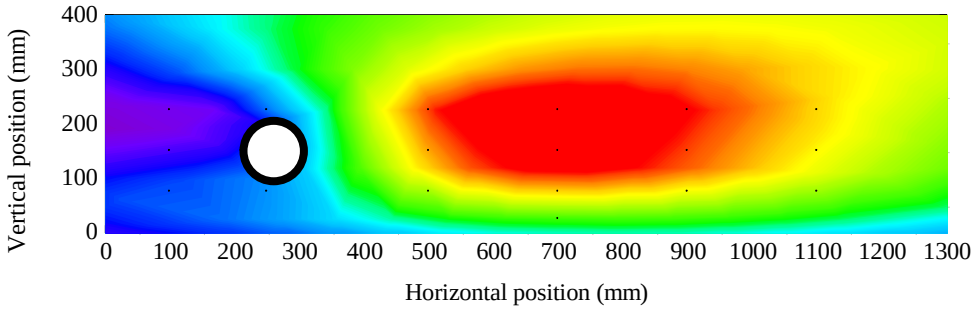

(b)

Figure 4.22 Distribution of excess pore water pressure ratio in Type-B (i = 0.0): (a) 5.0 mm and (b) 10.0 mm

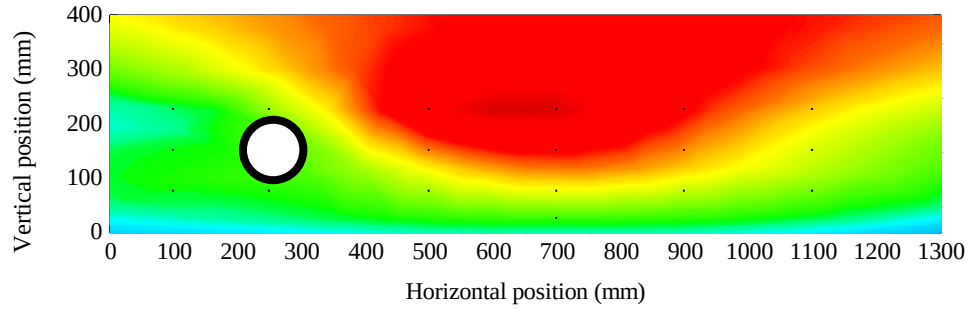

(a)

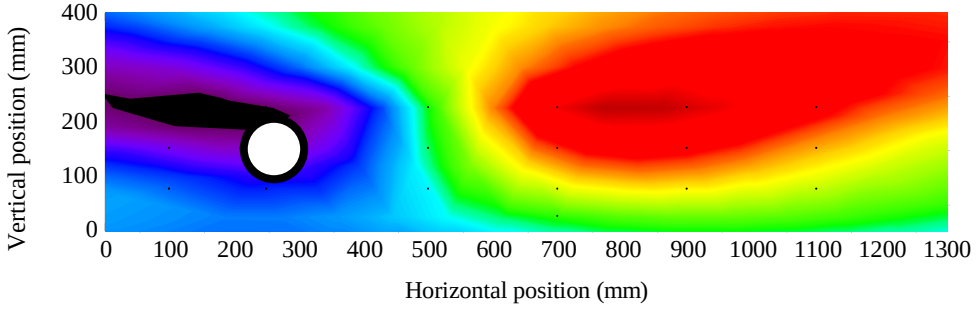

(b)

Figure 4.23 Distribution of excess pore water pressure ratio in Type-W2 (i = 0.0): (a) 5.0 mm and (b) 10.0 mm

toward the gravel area due to its high hydraulic conductivity (good permeability). As the variation of the excess pore water pressure directly relates to the effective stress of the soil, the ratio also affects the increase in the lateral resistive force. Subsequently, the raised excess pore water pressure on the passive side is greatly dissipated (Y = 10.0 mm). By expanding the width of the gravel, the drop in the excess pore water pressure during the lateral displacement becomes larger. There is a possibility that the expanded void in the gravel zone due to the movement of the pipe (positive dilatancy) absorbed the pore pressure from the surrounding sand bed.

4.5.5 Gravel reinforcement

By showing the relationship between the lateral resistive force and the excess pore water pressure ratio instead of the hydraulic gradient, we can compare the resistive force of the soil in the actual stress state. **Figure 4.24** shows the variation of the resistive force with the excess pore water pressure ratio. The resistive force and the ratio at Y = 20.0 mm are plotted. The ratio is calculated from the excess pore water pressure measured at PP9 embedded on the

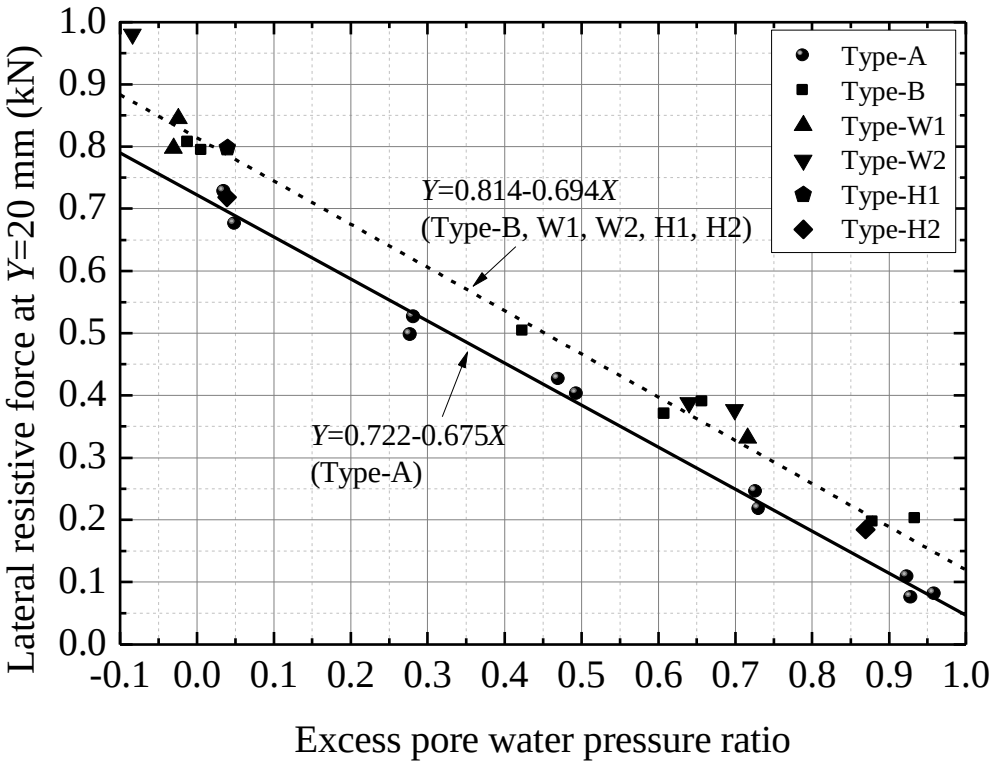

Figure 4.24 Variation of resistive force at Y = 20 mm with excess pore water pressure ratio

passive side of the pipe (see **Figure 4.1**). The solid and dashed line are approximate lines of Type-A and other cases, respectively. This gradient means the reduction rate of the resistive force with the increase in the ratio. From this graph, the following two facts are obvious.

First, the resistive force increases in all cases by using the gravel at any excess pore water pressure ratio. Since this graph has already taken into account the variation of the stress state of the soil bed, it is assumed that the difference between two lines is derived from the shear strength of the gravel. Since the slopes of the approximate lines are the same, the ratio of the two intercepts (12%) is the simple increase in the resistive force due to the shear strength of the gravel.

Second, the results of all cases except Type-A are on the same approximate line. Although the plots move to the upper left of the graph as the dissipation effect increases, its positon is still on the approximate line. This result implies that the range of gravel affects only the dissipation effect of the excess pore water pressure during pipe movement, and the lateral resistive force is determined by the effective stress of the soil on the passive side. The relationship between the width and the dissipation effect is shown in Chapter 6.

4.5.6 Geogrid reinforcement

Figure 4.25 shows the force-displacement curve in Type-B_G (Type-B plus geogrid). In comparison with Type-B, the resistive force in Type-B_G increases after the pipe displaces about 10 mm (normalized displacement Y/D = 0.1). This tendency is observed also at i = 0.9. By integrating the gravel with the geogrid, the resistive force keeps increasing almost linearly without settling to a constant value.

The reinforcement mechanism by the geogrid is investigated by image analysis using PIV. **Figure 4.26** show the distributions of the velocity vector at i = 0.0. The input parameters for PIV analysis are the same as summarized in **Table 4.2**. In comparison with the PIV results of the sand bed (see **Figure 4.10 (d)**), clear differences of the vector distribution cannot be observed by the substitution of the gravel. On the other hand, when integrating the gravel area with the geogrid, we can see the rightward movement of the soil at the active side (especially lower-left corner), at the bottom of the pipe, and at the lower-right of the pipe. These velocity

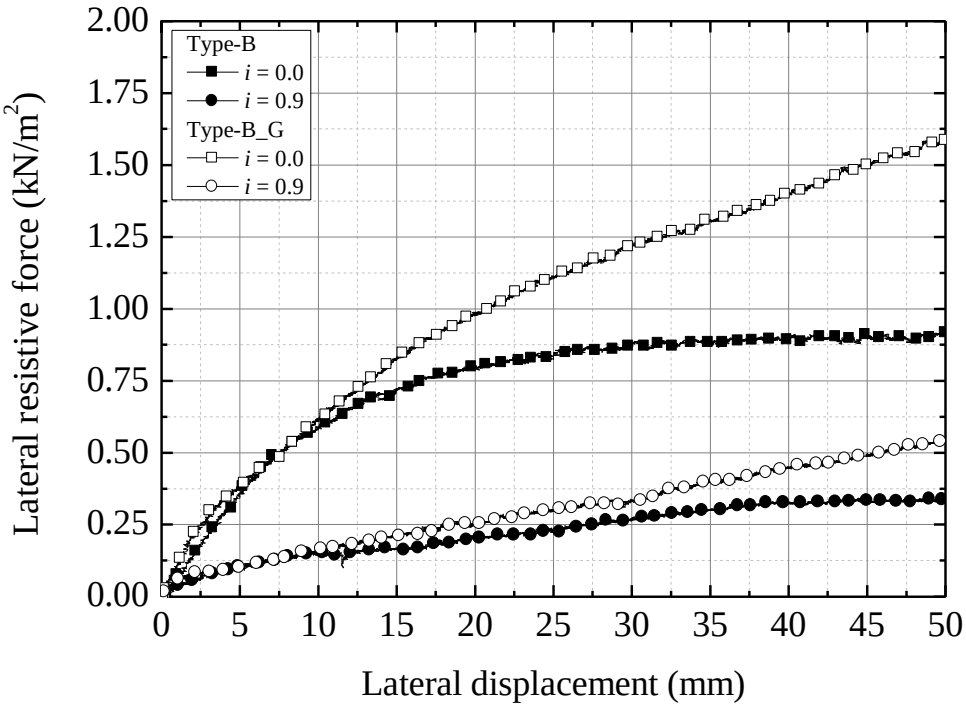

Figure 4.25 Force-displacement curve in Type-B and Type-B_G

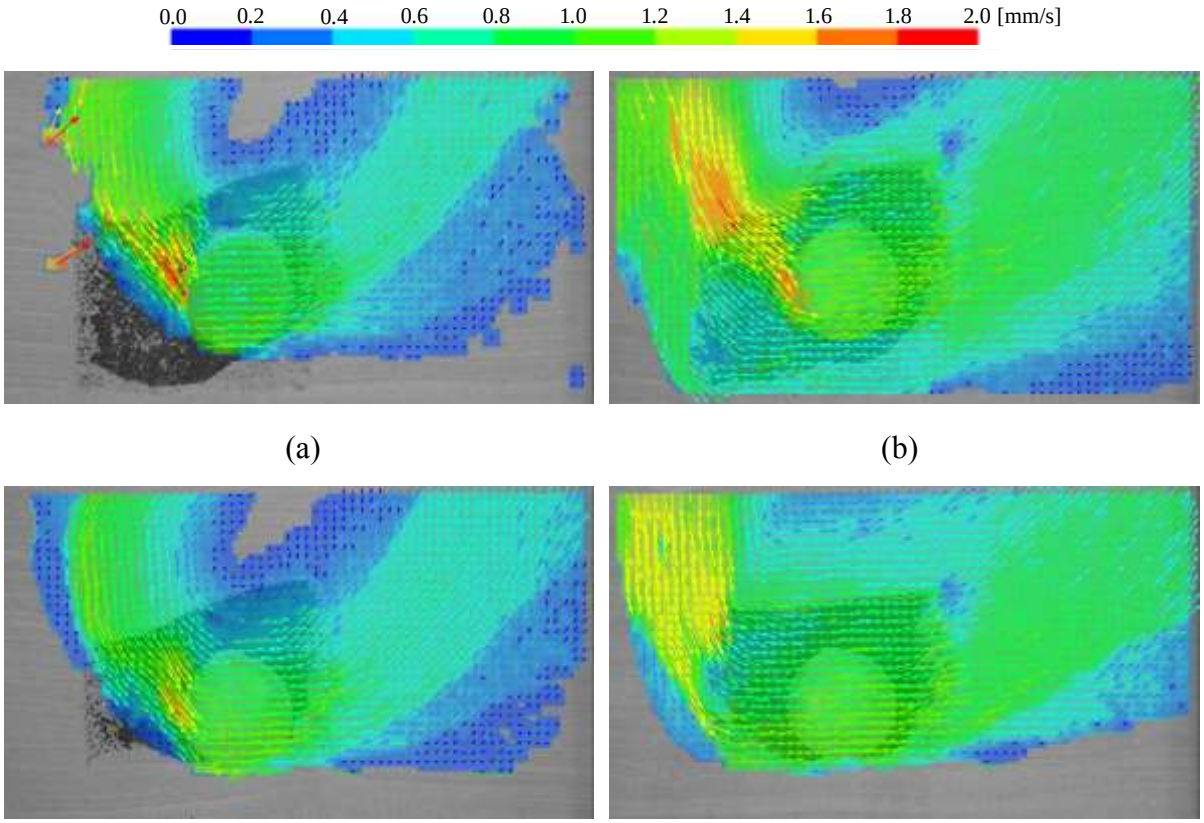

Figure 4.26 Velocity vector at i = 0.0, Y = 50.0 mm:
(a) Type-B, (b) Type-B_G, (c) Type-H2, and (d) Type-H2_G

components of the vector are approximately equal to that of the pipe. These results indicate that the backfill surrounding the pipe displaces together by integrating with the geogrid. Moreover, when focusing on the soil on the passive side of the pipe, the movement range of the soil in the vertical direction is widened. From the comparison between Type-B_G and Type-H2_G, it is clear that this moving range is equal to the integrated height by the geogrid. This fact implies that the passive earth pressure (lateral resistive force) increases because of the expansion of the lateral projected area due to the integration by the geogrid.

Figure 4.27 shows the cross-sectional deformation of the geogrid at i = 0.0 in Type-B_G. Each line represents the shape of the geogrid in the cross section every 6.0 mm lateral displacement of the pipe, e.g. black line and red line shows 0.0 mm and 48.0 mm, respectively. Judging from each line, the geogrid at the upper-left corner does not displace greatly until the pipe displaces 12.0 mm. This result means that the gravel inside the geogrid displaces or compresses repeatedly until the pipe moves 12.0 mm. In this state, no tension acts on the geogrid in spite of the movement of the pipe, and the restraining effect by the integration does not work at all. This displacement (Y = 12.0 mm) is approximately equal to the timing when the geogrid starts to add the resistive force (see **Figure 4.25**), and this means that there is a time delay until the restraining effect works.

Subsequently, the gravel at the upper-left corner starts to inflow into the void formed by the displacement of the pipe, and the geogrid follows its movement. On the contrary, at the lower-left corner, the geogrid starts to move to the right from a displacement of 36.0 mm. Since

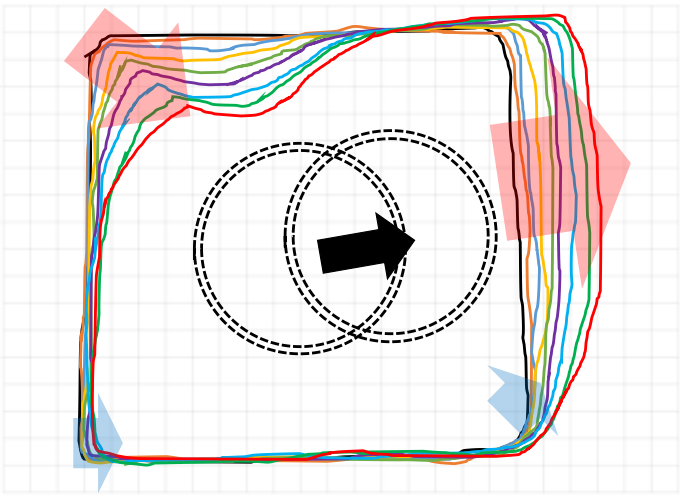

Figure 4.27 Cross-sectional deformation of geogrid at i = 0.0 in Type-B_G

the upper-left corner first moves toward the lower-right direction, transmission of the tension to the geogrid at the lower-left corner takes time. The geogrid on the passive side of the pipe is moving rightward immediately after the displacement starts. The movement of the geogrid at the lower-right corner is small because the pipe is moving with floating subjected to the supporting force from the lower right. The equal interval of each geogrid line after $Y = 36.0$ mm indicates that the pipe and its surrounding gravel continue to move together by integrated.

The PIV results revealed that the pipe and its surrounding gravel integrated by the geogrid displaced together, and the gravel integrated by the geogrid received the passive earth pressure on its vertical plane. From the above results, it is expected that the increase in the resistive force due to the geogrid depends on the burial depth and the area of the pressure receiving surface. Therefore, on the assumption that the integrated range by the geogrid is a single object, the resistive forces in the various cases (Type-B, H2, B_G, and H2_G) with different burial depth and pressure receiving area are investigated. The lateral resistive force can be normalized by the unit weight of the soil, the diameter, the burial depth, and the length of the pipe:

$$P_N = \frac{P}{\gamma'_0 D H_1 L} \tag{4.6}$$

where P is the lateral resistive force (kN), γ'_0 is the effective unit weight of the soil (kN/m^3), D is the diameter (m), H_1 is the depth to the top of the pipe (m), and L is the length of the pipe (m). In Type-B and Type-H2, the diameter and the burial depth are 0.10 m and 0.20 m, respectively. In Type-B_G, considering the integration in the vertical direction, the diameter and the burial depth are set to 0.20 m and 0.15 m, respectively. In the same way, they are 0.10 m and 0.15 m, respectively in Type-H2_G.

Figure 4.28 shows the variations of the dimensionless resistive force with the lateral displacement in each case for $i = 0.0$ and 0.9. At $i = 0.0$, each relationship between the force and the displacement is in good agreement in all cases. A similar tendency is also recognized at $i = 0.9$ although there are some variations. These results mean that the lateral resistive force is approximately proportional to the pressure receiving area of the integrated range. On the other hand, the dimensionless force at $i = 0.9$ is about twice to third larger than that at $i = 0.0$. If the resistive force depends on the earth pressure, a relationship between the force and the

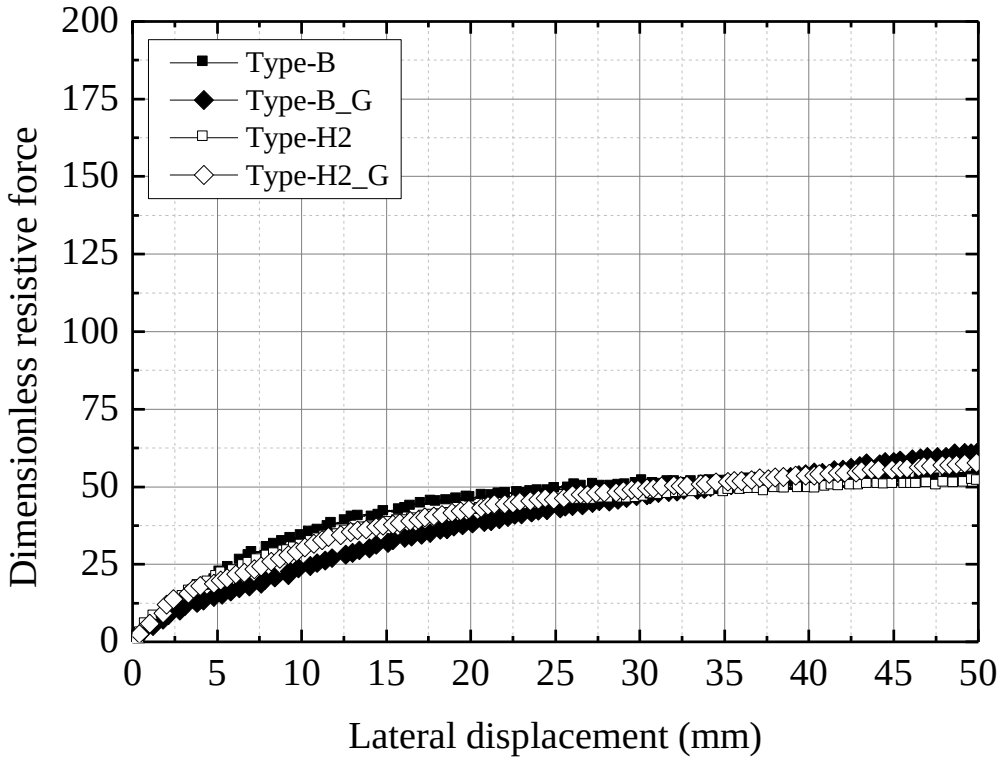

(a)

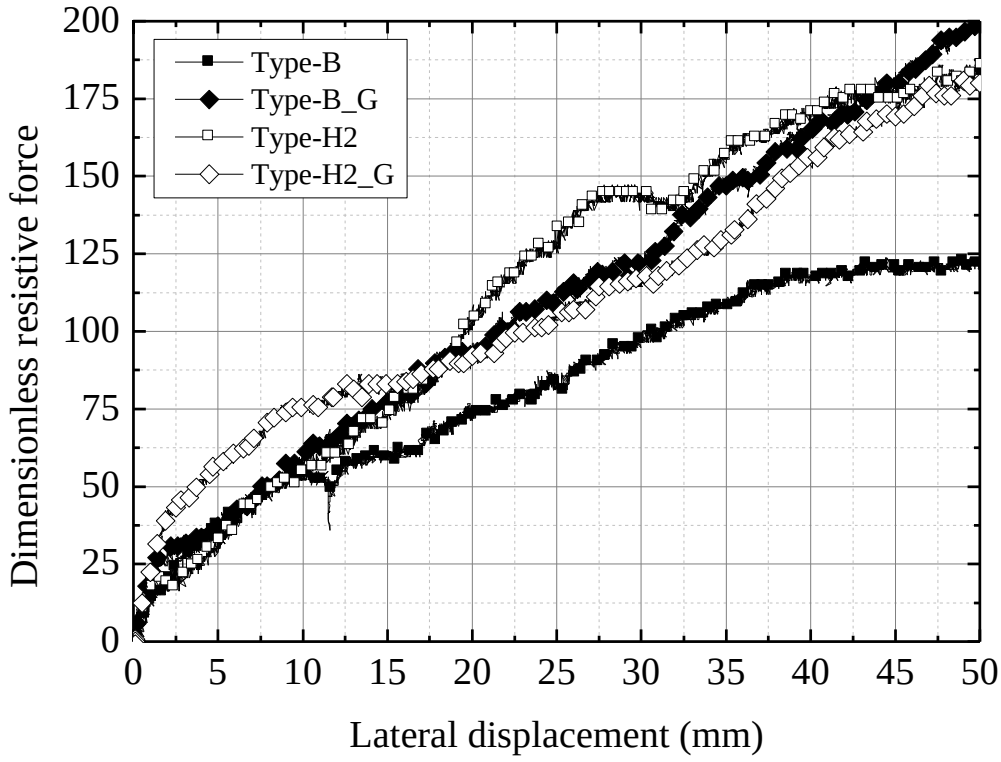

(b)

Figure 4.28 Variation of normalized resistive force with lateral displacement: (a) $i = 0.0$ and (b) $i = 0.9$

displacement should be corresponded under different hydraulic gradient because the difference of the effective stress has been already considered in the effective unit weight in Eq. (4.6). The cause of this is the influence of the dissipation of the excess pore water pressure during the lateral loading. As shown in **Figure 4.4**, the resistive force in the soil under high hydraulic gradient tends to become large due to the dissipation effect. However, in any case, it is an evaluation on the safety side because the dimensionless force was evaluated with a smaller unit weight than actual state.

4.5.7 Comparison of various countermeasures

The effectiveness of the proposed various countermeasures are summarized to examine the superiority against the existing design method. In the design guideline, the resultant force of the passive earth pressure behind the pipe R_H is expected as a resistive force against the thrust force. The resultant force in the saturated soil is calculated by the following equation.

$$R_H = 0.65\frac{1}{2}K_p w' B_p \left(H_2{}^2 - H_1{}^2\right) \tag{4.7}$$

where 0.65 is the reduction correction coefficient of the passive resistance of curved surface, K_p is the coefficient of passive earth pressure, γ'_0 is the submerged unit weight of the soil (kN/m^3), B_p is the width of the back side of the pipe (m), H_1 is the depth to the top of the pipe (m), and H_2 is the depth to the bottom of the pipe (m). The resultant force of the passive earth pressure obtained by substituting the present experimental condition (H/D = 2.0) is about 0.20 kN. When the thrust force acting on the buried pipe exceeds this resistive force, the pipe is judged to start moving. In the present design, installation of a concrete block surrounding the pipe is recommended as a countermeasure. In this case, H_1 and H_2 in Eq. (4.7) are changed according to the size of the block to estimate the resistive force greater. In the present experimental condition, assuming that the square area (2D) surrounding the pipe is concreted, the calculated resultant force is approximately 0.40 kN when ignoring the friction between the bottom surface of the block and the soil.

Figure 4.29 shows the relationship between the lateral displacement of the pipe and the excess pore water pressure ratio of the soil. The horizontal axis shows the lateral

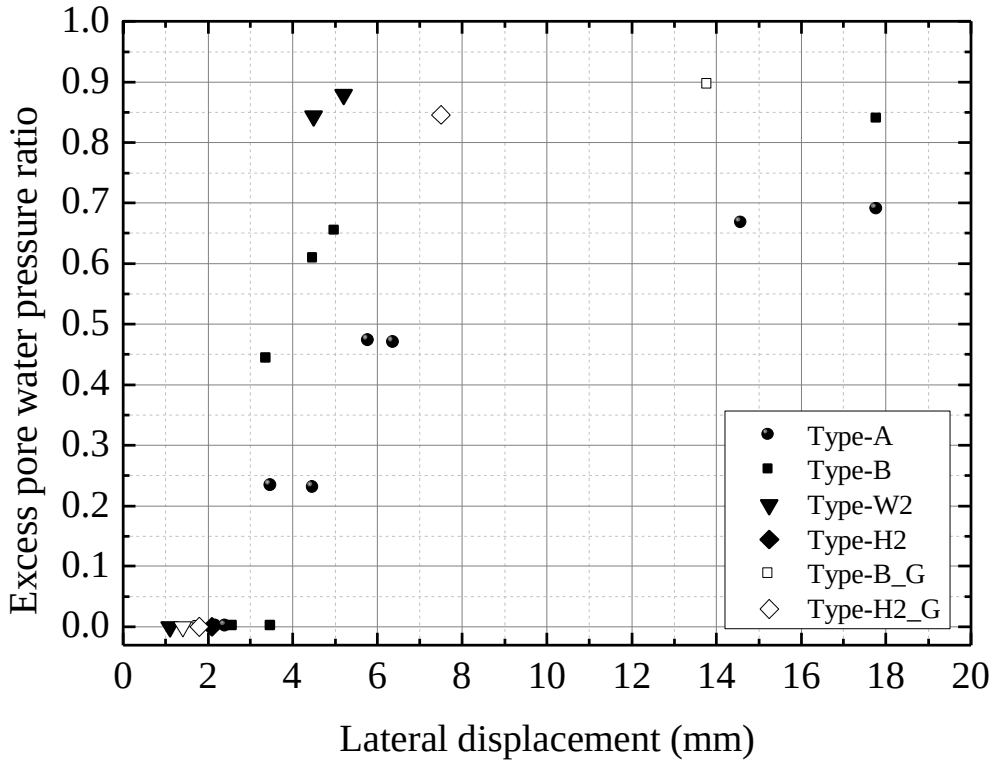

(a)

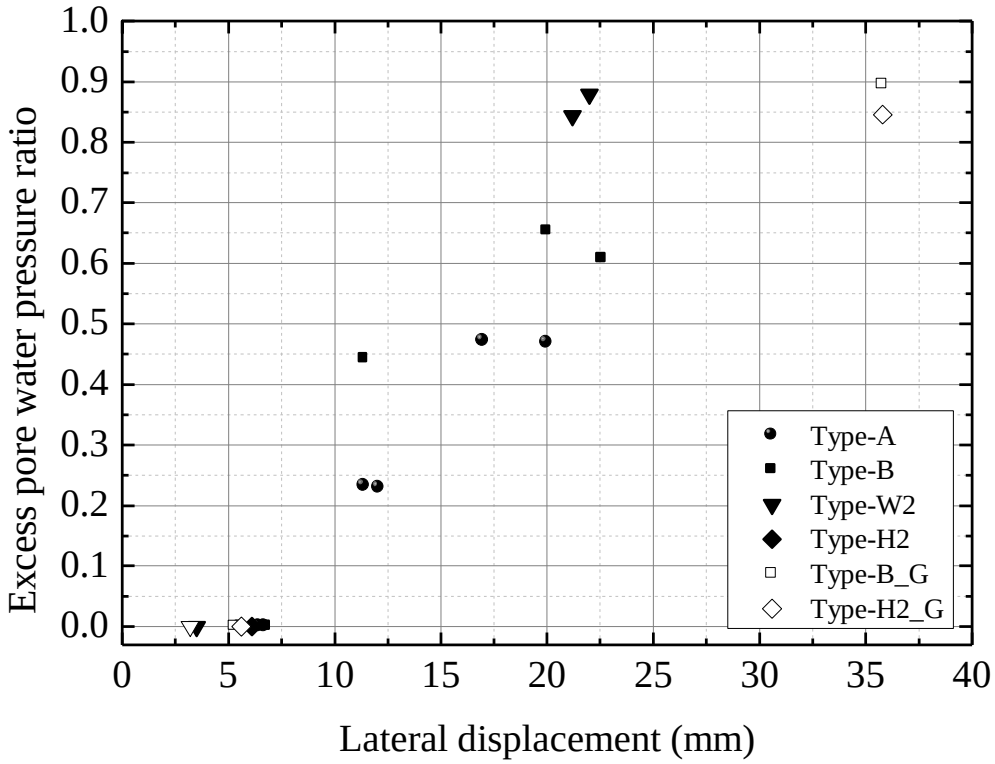

(b)

Figure 4.29 Relationship between lateral displacement and excess pore water pressure ratio: (a) 0.20 kN and (b) 0.40 kN

displacement when the resistive force reaches the resultant force of the passive earth pressure calculated above (0.20 and 0.40 kN), and the vertical axis shows the average of the excess pore water pressure ratio measured before the loading. This graph indicates that the closer the plot approaches to the upper-left corner, the more the resistive force is retained to suppress the lateral displacement even when liquefaction occur. In **Figure 4.29 (a)**, we can confirm that there is no large difference in the lateral displacement in each case when the excess pore water pressure ratio is 0.0 (saturated condition). As the ratio increases, the lateral displacement nonlinearly increases. The lateral displacement in Type-W2 is the smallest of all. The results in the case using geogrid indicate that the displacement of the pipe is so small that the restraining effect by the geogrid has not appeared yet.

On the other hand, larger lateral displacement is required to obtain greater resistive force as shown in **Figure 4.29 (b)**. Especially when the excess pore water pressure ratio is 0.8 ~ 1.0, there are plots of only Type-W2, B_G, and H2_G because the resistive force of 0.40 kN cannot be obtained in the other cases. The graph indicates that the displacement of the pipe is greatly suppressed when the gravel is integrated by the geogrid.

As mentioned above, the current design guideline does not take into account the influence of liquefaction on the stability of the buried pipeline. Chapter 6 proposes the design method considering the variation of the effective stress of the soil.

4.6 Conclusions

In this chapter, lateral loading experiments on a model pipe was conducted to clarify the influence of the initial effective stress on the relationship between the lateral resistive force and the lateral displacement of the pipe subjected to an external force. The following conclusions were made.

1. The force-displacement curve for each hydraulic gradient showed a nonlinear relationship. The lateral resistive force increased appreciably immediately upon loading, after which it increased more moderately. At the critical hydraulic gradient, although the resistive force was almost zero at the very beginning of the loading, the force increased gradually due to the dissipation of the excess pore water pressure with the pipe displacement.

2. The load-controlled experiments revealed that the pipe started to move appreciably when the excess pore water pressure ratio of the soil exceeded 0.8. The relationship between the lateral displacement and the excess pore water pressure ratio in the load-controlled experiments corresponded reasonably well with that in the displacement-controlled experiments.
3. The failure mechanism of the passive-side soil could be visually obtained by PIV analysis. The PIV results revealed that the variation of the resistive force depended on the two deformation mechanisms: compression and shear. The moving vector showed the fluid-like behavior of the soil when the effective stress was low.
4. The effective stress of the soil surrounding the pipe was recovered due to the dissipation of the excess pore water pressure with the pipe movement. The comparison with the PIV results revealed that the distribution of the excess pore water pressure was different around the slip surface.
5. By partially substituting the backfill by the gravel, the increase in the excess pore water pressure during the displacement of the pipe was suppressed, and the lateral resistive force increased. When using the gravel as backfill, the resistive force increased by approximately 12% due to the shear strength of the gravel under any stress condition. Although the dissipation effect of the excess pore water pressure was enhanced with the increase in the width of the gravel range, there was no clear difference in lateral resistive force when the excess pore water pressure ratio.
6. The PIV results revealed that the pipe and its surrounding gravel integrated by the geogrid displaced together, and the integrated gravel received passive earth pressure on its vertical plane. Each lateral resistive forces in different cases normalized by the diameter of the pipe, the pipe length, the burial depth, and the effective unit weight of the soil agreed with each other. The integrating effect by the geogrid could be simply explained as the increases in the pressure receiving area.

References

Audibert, J. M. E. and Nyman, K. J. 1977. Soil Restraint against Horizontal Motion of Pipes, *Journal of the Geotechnical Engineering Division*, 103(10), 1119-1142.

Calvetti, F., Prisco, C. and Nova, R. 2004. Experimental and Numerical Analysis of Soil-Pipe Interaction, *Journal of Geotechnical and Geoenvironmental Engineering*, 130(12) 1292-1299.

Kaga, A., Inoue, Y., and Yamaguti, K. 1994. Pattern Tracking Algorithms for Airflow Measurement Through Digital Image Processing of Visualized Images, *Journal of the Visualization Society of Japan*, 14(53), 108-115. (in Japanese with English summary).

Kimura, I., Yamashita, N., and Kuroe, Y. 1992. Determination of Erroneous Velocity Vectors Using Neutral Networks, *Proceedings of 1992 JSME Fluids Engineering Division*, 310-313. (in Japanese with English summary).

Lamb, H. 1911. On the Uniform Motion of a Sphere through a viscous fluid, *Philosophical Magazine and Journal of Science,* 21(121), 112-121.

Ministry of Agriculture, Forestry and Fisheries of Japan (MAFF). 2009. Planning and Design Criteria of Land Improvement Project (Pipeline), JSIDRE, 321-409. (in Japanese).

Miyajima, M. and Kitaura, M. 1994. Experiments on Force Acting on Underground Structures in Liquefaction-Induced Ground Flow, *Proceedings of 5th US-Japan Workshop on Earthquake Resistant Design of Lifeline Facilities and Countermeasures against Soil Liquefaction*, 445-455.

Towhata, I., Vargas-Monge, W., Orense, R. P. and Yao, M. 1999. Shaking Table Tests on Subgrade Reaction of Pipe Embedded in Sandy Liquefied Subsoil, *Journal of Soil Dynamics and Earthquake Engineering*, 18(5), 347-361.

CHAPTER 5

The contents of this chapter are based on:

Ono, K., Terada, K., Sawada, Y., Ling, H. I., and Kawabata, T. 2017. Fluid Coupled-DEM Simulation of Lateral Loading Experiment for Buried Pipe in Liquefiable Soil, Transportation Infrastructure Geotechnology (submitted)

Chapter 5

Fluid Coupled-DEM Simulation of Lateral Loading Experiment

5.1 Introduction

Many model experiments and numerical analyses have been performed for investigating interactions between underground structures and the surrounding soil. In recent years, the numerical analysis using DEM (Discrete Element Method) has been widely used with the increasing computing capability of computers. The DEM analysis devised by Cundall and Strack (1979) treats the number of spherical elements as assembly to model a soil bed as a granular body. Compared with FEM (Finite Element Method), which has played a central role in geotechnical field, DEM is good at handling simulations in which discrete motion is dominant (e.g. prediction problems for slope failures, falling rocks, large deformation of soil).

In addition, fluid coupled-DEM modeling that combined the conventional DEM with the seepage analysis has been developed for simulating the soil particles subjected to pore water pressures (e.g. Tarumi and Hakuno, 1988, Shimizu, 2006). As stated later, the dynamic behavior of the saturated soil is simulated by applying external forces attributed to the pore water pressure to each soil particle. This kind of coupled analysis between soil and fluid has been used in not only simulating the behavior of the soil mass but also in solving the boundary value problems. Since the greatest feature of DEM is to handle the soil discontinuously as a granular body, enhancing the DEM analysis considering the pore water is valuable in dealing with the interaction problems involving large soil deformation.

The aim of this chapter is to carry out numerical simulations of lateral loading

experiments for a buried pipe shown in Chapter 4. The fluid coupled-DEM is utilized to investigate the lateral pipe-soil interaction under various effective stress conditions. On the basis of the analysis results, displacement mechanism of the buried pipe and its surrounding soil is examined, and the applicability of this analysis method to interaction problems between an underground structure and surrounding soil is verified.

5.2 Algorithm for DEM Analysis

5.2.1 Solid phase

Equation of motion

The basic concept of DEM is easy to understand by considering one-dimensional condition: Moriguchi et al. (2015) or Matsushima et al. (2015) describe details. When an element *A* is in contact with another element *B* and the contact force acts between both elements, the equation of motion of the element *A* is expressed by the following equation.

$$m\frac{d^2u}{dt^2}+c\frac{du}{dt}+ku=0 \tag{5.1}$$

where m is the weight of an element (kg), u is the relative displacement between both elements (m), c is the viscosity coefficient, and k is the spring coefficient (N/m). The first term on the left side is the Newton's second law, the second one means the force generated by the dashpot, and the third one is the force generated by the spring. In Eq. (5.1), when we obtain the second and third term at a certain time, the acceleration of the element at that time can be calculated. By the temporal integration of the acceleration with a difference method, the displacement of the element can be finally obtained.

The most crucial point in expanding to two-dimensional condition is the introduction of the degree of freedom of rotation. The motion of the DEM element is classified into two: the translational motion of the center of gravity and the rotational motion around the center of gravity. Firstly, the translational motion is expressed as

$$m\begin{pmatrix}\ddot{u}_x\\ \ddot{u}_y\end{pmatrix}=m\begin{pmatrix}g_x\\ g_y\end{pmatrix}+\begin{pmatrix}F_x\\ F_y\end{pmatrix} \tag{5.2}$$

where g is the gravitational acceleration (m/s^2), and F is the summation of the external force

(N). The summation of the external force is expressed as follows by the contact force from the other elements:

$$\begin{pmatrix} F_x \\ F_y \end{pmatrix} = \begin{pmatrix} \sum_{j=1}^{N} f_x^j \\ \sum_{j=1}^{N} f_y^j \end{pmatrix} \tag{5.3}$$

where N is the total number of contact points and f^j is the contact force of j-th element (N).

On the contrary, the rotational motion is represented as

$$I_{zz}\dot{\omega}_z = L_z \tag{5.4}$$

where I_{zz} is the moment of inertia in the x-y plane (kg m^2), ω_z is the rotational velocity around the center of the element (rad/s), and L_z is the summation of the moment by the external force from the element surface (kg m^2). When considering only the contact force between the elements:

$$L_z = \sum_{j=1}^{N} (l_x^j f_y^j - l_y^j f_x^j) \tag{5.5}$$

where l^j is the vector component heading from the center of the element to the j-th contact point.

Contact determination

The contact between elements can be determined readily from the geometrical arrangement as shown in **Figure 5.1**. Whether or not two elements: i (center position: $\boldsymbol{x}_i = (x_i, y_i)$ and radius: r_i) and j (center position: $\boldsymbol{x}_j = (x_j, y_j)$ and radius: r_j) are contact is judged from the displacement in the normal direction at the contact point in the local coordinate system:

$$\delta_n = -\left(r_i + r_j - \left\| \boldsymbol{x}_j - \boldsymbol{x}_i \right\| \right) \tag{5.6}$$

When δ_n is equal or smaller than 0.0, both elements are contact.

Contact force

The contact force is calculated by setting the Voigt model in the normal and tangential direction of the local coordinate system along the contact surface. The Voigt model

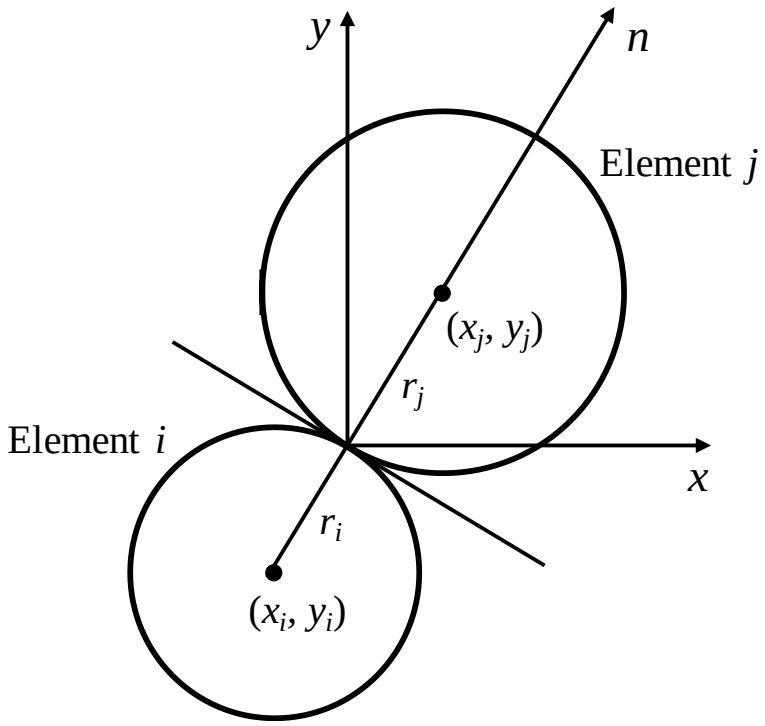

Figure 5.1 Contact determination

is a model in which a spring and a dashpot are coupled in parallel as shown in **Figure 5.2**. In the linear spring model, the contact force is calculated as follows.

$$\begin{pmatrix} f_n \\ f_s \end{pmatrix} = \begin{pmatrix} k_n & 0 \\ 0 & k_s \end{pmatrix} \begin{pmatrix} \delta_n \\ \delta_s \end{pmatrix} - \begin{pmatrix} c_n & 0 \\ 0 & c_s \end{pmatrix} \begin{pmatrix} \dot{\delta}_n \\ \dot{\delta}_s \end{pmatrix} \tag{5.7}$$

where k_n is the normal spring coefficient (N/m), k_s is the tangential spring coefficient (N/m), c_n is the normal viscosity coefficient (Pa s), and c_s is the tangential viscosity coefficient (Pa s), δ_n is the displacement in the normal direction (m), and δ_s is the displacement in the tangential direction (m). In addition, the slider model is added to the Voigt model in series in the tangential direction to model slipping between elements.

The component of the contact force obtained in the local coordinate system is converted to the global coordinate system via the transformation matrix.

$$\begin{pmatrix} f_x \\ f_y \end{pmatrix} = \begin{pmatrix} \cos\theta & -\sin\theta \\ \sin\theta & \cos\theta \end{pmatrix} \begin{pmatrix} f_n \\ f_s \end{pmatrix} \tag{5.8}$$

where θ is the rotation angle (^{o}) from the global coordinate system to the local coordinate system (the angle of the normal vector at the contact point to the x-axis).

For the calculation of the contact force in Eq. (5.7), the calculation method of the

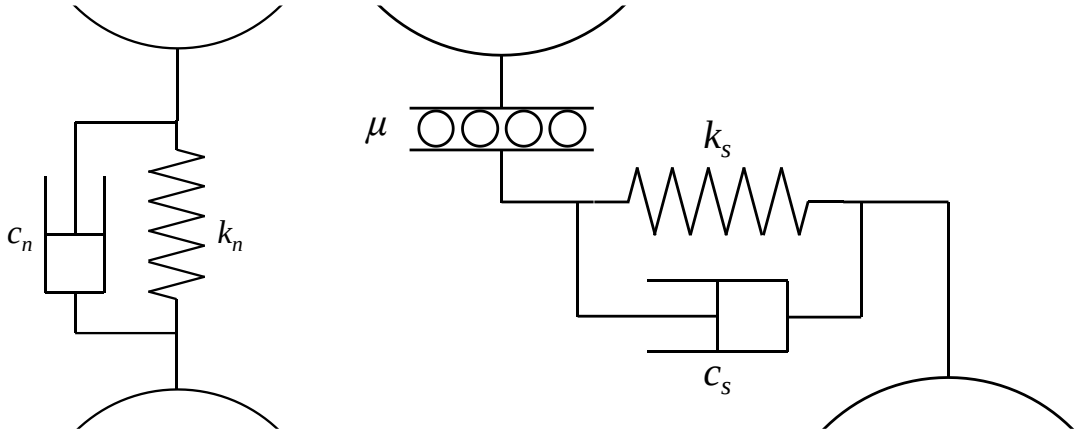

Figure 5.2 Voigt model in DEM: (a) normal direction and (b) tangential direction

angle at the contact surface, the contact point position, and the displacement at the contact point are shown below. The normal vector on the contact surface *n* and the position vector *c* at the contact point are obtained from the coordinate of the center and the radius of each element *i* and *j* as follows.

$$\boldsymbol{n} = \frac{\boldsymbol{x}_j - \boldsymbol{x}_i}{\left\| \boldsymbol{x}_j - \boldsymbol{x}_i \right\|} \tag{5.9}$$

$$\boldsymbol{c} = \boldsymbol{x}_i + \frac{r_j}{r_i + r_j}\left(\boldsymbol{x}_j - \boldsymbol{x}_i \right) \tag{5.10}$$

Furthermore, the summation of the translational velocity and the rotational velocity is regarded as the displacement velocity at the contact point. That is, the relative velocity of the element *j* to the element *i* is

$$\begin{pmatrix} \dot{\delta}_x \\ \dot{\delta}_y \end{pmatrix} = \begin{pmatrix} \dot{x}^j - \dot{x}^i \\ \dot{y}^j - \dot{y}^i \end{pmatrix} + \begin{pmatrix} -\omega_z{}^j l_y{}^j + \omega_z{}^i l_y{}^i \\ \omega_z{}^j l_x{}^j + \omega_z{}^i l_x{}^i \end{pmatrix} \tag{5.11}$$

By converting this relative velocity to the global coordinate system, the contact force can be obtained from Eq. (5.7). It should be noted that the displacement in the tangential direction is calculated by the following equation by accumulation of each time step because it cannot be obtained only by geometrical arrangement.

$$\delta_s^{t+\Delta t} = \delta_s^t + \dot{\delta}_s \Delta t \tag{5.12}$$

where Δt is the time step (s).

5.2.2 Liquid phase

DEM analysis considering the influence of the pore water pressure can be categorized generally into three groups based on the resolution of the interaction between the soil particles and the pore water pressures: coarse fluid-mesh level, pore element level, or direct calculation level (Koyama et al., 2015). The high-resolution model can represent the pore water more directly. Although we can follow the mechanism of the inside of the soil, the calculation cost increases dramatically. In the present study, the fluid coupled-DEM analysis in the coarse fluid-mesh level was adopted because the main aim of the analysis is to simulate the relatively macroscopic interaction between the displacement of the buried pipe and the liquefied soil.

Nakase et al. (1999) developed the fluid coupled-DEM model that reduced the calculation cost by calculating the pore water pressure in the fluid-mesh level. The same kind of models were evolved by Zeghal and Shamy (2004) and Shafipour and Soroush (2008) to reflect the viscosity of the fluid. Since the loading rate in the present analysis is low enough (1.0 mm/s) to ignore the viscous resistance of the liquefied soil, the more primitive model that is based on the Nakase's algorithm was used. In this model, the saturated soil bed is divided into two phase: solid and fluid phases. Detailed procedures of calculations are shown as follows.

Pore volume change

First, the fluid domain is divided into arbitrary-sized cells. The cells in which each element locates is judged from the coordinate of the center of each element. The pore volume change in the cell (i, j) is calculated from the average displacement of the elements in the neighboring four-cells:

$$\Delta v^{(i,j)} = \Delta v^{(i,j)}_{(i-1,j)} + \Delta v^{(i,j)}_{(i+1,j)} + \Delta v^{(i,j)}_{(i,j-1)} + \Delta v^{(i,j)}_{(i,j+1)} \tag{5.13}$$

where $\Delta v^{(i,j)}$ is the pore volume change in cell (i, j) (m^2). In Eq. (5.13), the contribution of each neighboring cells to the volume change in cell (i, j) is calculated from the weighted average displacement of elements in each cell. For example, the contribution of four elements: a, b, c, d in cell (i-1, j) shown in **Figure 5.3** can be obtained from following equation:

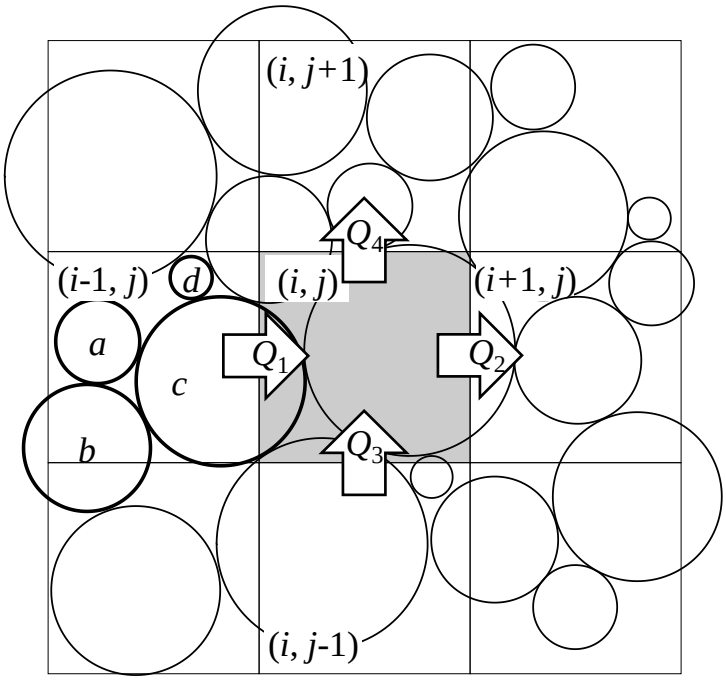

Figure 5.3 Pore volume change in a cell (Nakase et al, 1999; modified by the author)

$$\Delta v_{(i-1,j)}^{(i,j)} = -dy \sum_{k=1}^{4} \Delta x^{(k)} v^{(k)} \Big/ \sum_{k=1}^{4} v^{(k)} \tag{5.14}$$

where $\Delta x^{(k)}$ is the lateral displacement of the k-th element (m), and $v^{(k)}$ is the volume of the k-th element (m^2). Note that the contribution of the elements in cell (i-1, j) is represented as negative because the displacement of the elements in the positive x-direction in cell (i-1, j) contributes to decrease the pore volume in cell (i, j). Similar equations can be written for the other three cells.

Excess pore water pressure

The pore volume change due to the movement of the elements generates the excess pore water pressures. Assuming that the pore is perfectly saturated and the excess pore water pressure increases proportionally with the pore volume change, the increment of the excess pore water pressure is calculated from the volume change and a storage coefficient of fluid. That is,

$$\Delta h^{(i,j)} = \frac{\Delta v^{(i,j)}}{S^{(i,j)} dxdy} \tag{5.15}$$

where $\Delta h^{(i,j)}$ is the pore water pressure in cell (i, j) (m), $\Delta v^{(i,j)}$ is the pore volume change in

cell (i, j) (m^2), $S^{(i,j)}$ is the storage coefficient of fluid (m^{-1}), dx is the width of each cell (m), and dy is the height of each cell (m). The pore water pressure in Eq. (5.15) is expressed as the piezo water head.

Body force acting on elements

Assuming that the fluid flow generates only between neighboring cells (see **Figure 5.3**), the body force acting on the elements in cell (i, j) are calculated from the pressure gradient between the neighboring cells, then

$$B_x^{(i,j)} = \frac{h^{(i+1,j:t)} - h^{(i-1,j:t)}}{2dx} \gamma_w v^{(k)} \tag{5.16}$$

$$B_y^{(i,j)} = \frac{h^{(i,j+1:t)} - h^{(i,j-1:t)}}{2dy} \gamma_w v^{(k)} \tag{5.17}$$

where $B_x^{(i,j)}$ is the body force in x-direction acting on the elements in cell (i, j) (N), $B_y^{(i,j)}$ is the body force in y-direction (N), γ_w is the unit weight of water (N/m^2), and $v^{(k)}$ is the volume of k-th element (m^2). Note that the distance between the neighboring three-cells is the same by doubling the width of a cell because it is defined as the distance between centers of the cells. The body forces are added to the soil particles in the solid phase in the conventional DEM program.

Dissipation of pore water pressure

The dissipation of the pore water pressure is calculated based on both equation of continuity and Darcy's law. Considering water balance in a cell, the difference between inflow and outflow is equivalent to the fluid quantity stored in a certain period, then

$$\sum_{k=1}^{4} Q_k \Delta t = \left(h^{(i,j:t+\Delta t)} - h^{(i,j:t)} \right) S^{(i,j)} dxdy \tag{5.18}$$

where Q_k is the volume of fluid entering into cell (i, j) (m^2/s): inflow is positive and outflow is negative, Δt is the time increment (s), and $\bar{h}^{(i,j:t+\Delta t)}$ is the pore water pressure at time $t+\Delta t$ (m) The time increment in the equation of continuity is the same with that used for the calculation in the solid phase. For example, the fluid flow from cell (i-1, j) to (i, j) is formulated according to Darcy's law, then

$$Q_1 = k_1 \frac{h^{(i,j:t')} - h^{(i-1,j:t')}}{dx} dy \tag{5.19}$$

where k_1 is the hydraulic conductivity in x-direction (m/s) and $h^{(i,j:t')}$ is the pore water pressure at time t' (m). The hydraulic conductivity is a harmonic mean of that in the neighboring cells to express an impermeability of cells in an easy way. Similar equations can be written for the other three cells. Note that Crack-Nicolson method is applied in Eq. (5.19) to improve the calculation accuracy in the time domain. Therefore, $h^{(i,j:t')}$ is the weighted mean of $h^{(i,j:t)}$ and $h^{(i,j:t+\Delta t)}$ as

$$h^{(i,j:t')} = \frac{1}{2}\left(h^{(i,j:t)} + h^{(i,j:t+\Delta t)}\right) \tag{5.20}$$

Substituting Eq. (5.19) into Eq. (5.18) and imposing boundary and initial conditions lead to simultaneous equations for $\bar{h}^{(i,j:t+\Delta t)}$. The excess pore water pressure at $t+\Delta t$ is the sum of the dissipated water pressure and the excess pore water pressure due to the movement of elements during time increment. Thus, the total excess pore water pressure at $t+\Delta t$ is expressed as

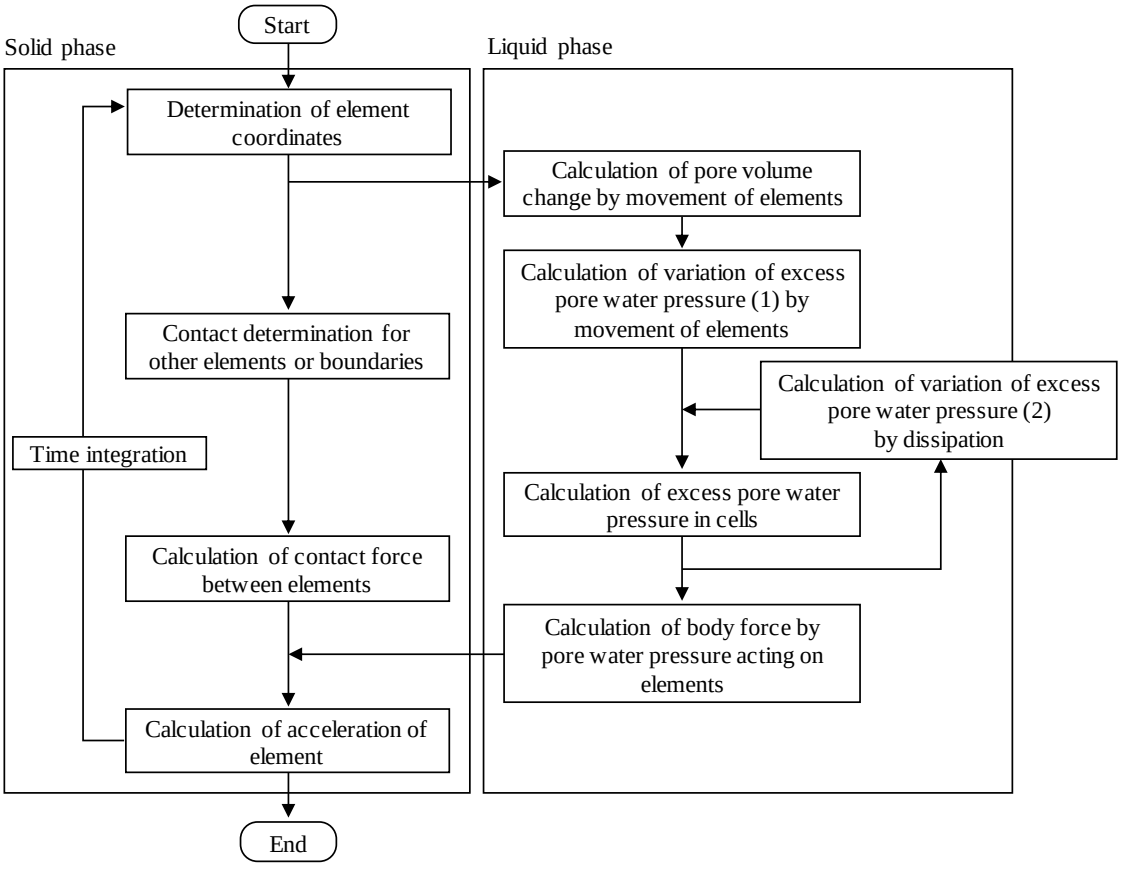

Figure 5.4 Entire algorithm for fluid coupled-DEM

$$h^{(i,j:t+\Delta t)} = \overline{h}^{(i,j:t+\Delta t)} + \Delta h^{(i,j)} \tag{5.21}$$

In summary, the present DEM consists of the following four steps:

1. Pore volume change is calculated from the averaged movement of the elements on the basis of the arbitrary-sized cells.
2. Excess pore water pressure is calculated as the product of the pore volume change and a storage coefficient of fluid.
3. External force is applied to the elements according to the pressure gradient in the neighboring cells. The external forces due to the pore water pressure are added to the soil particles in the solid phase.
4. Fluid flows between neighboring cells are calculated from the equation of continuity and Darcy's law.

The entire algorithm is shown in **Figure 5.4**.

5.3 Outline of DEM Simulation

5.3.1 Soil model

Figure 5.5 shows the analysis model. Each sand particle was modeled as a large spherical element. The mean particle size and the uniformity coefficient were 6.0 mm and 1.94, respectively. The mean particle size was 30 times larger than that of the actual sand used for the model experiment. The container was randomly filled with the particles subjected to gravitational force. The unit weight and the void ratio of the soil model were 13.7 kN/m^3 and 0.18, respectively. The density of the soil particle was adjusted so that the dry unit weight in

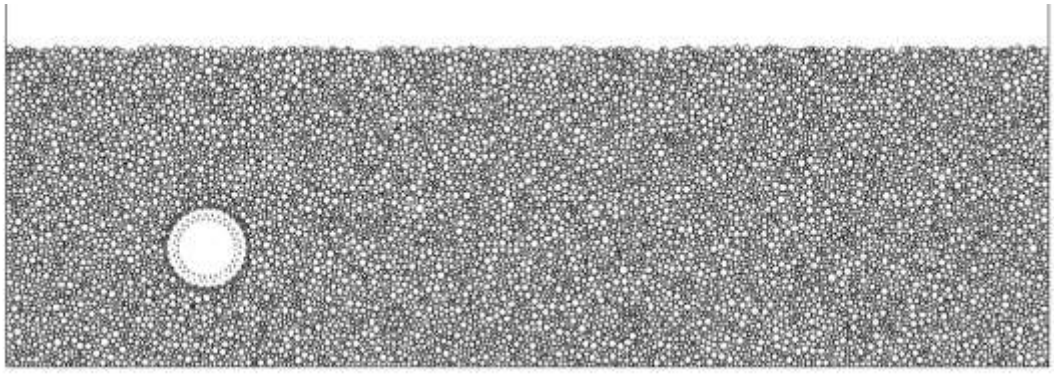

Figure 5.5 Analysis model

Table 5.1 Parameters of soil model

Normal spring coefficient (N/m)	6.0×10^6
Tangential spring coefficient (N/m)	1.0×10^5
Normal damping coefficient	0.8
Tangential damping coefficient	0.8
Inter-particle friction angle (°)	30
Rolling friction angle (°)	20

the analysis equal to that in the experiment. Note that the void ratio of the soil model was much smaller than that of the experiment because this was a two-dimensional simulation.

Table 5.1 summarizes the parameters of the soil model. Since the particle size was very different compared with the real one, the simulations of element tests such as tri-axial test has not been performed for calibration of each soil parameter. Each parameter was determined by trial and error based on the parameters estimated by Nakase et al. (2001) so that the force-displacement curve in DEM coincides with that obtained from the experiment in the dry sand. In addition, the soil model consisted of spherical particles, which exhibited less shear strength than that of actual sand because of the excessive rotation of each spherical particle. Therefore, the rolling friction developed by Sakaguchi et al. (1993) was added to each particle.

5.3.2 Pipe model

A polygon model devised by Nakase et al. (2002) was used to make the pipe model. The polygon model was an assembly of the same-sized particles that were connected with pore springs and was covered with boundaries. The pipe model was a truss structure with regular 32-side polygons consisting of 96 particles as shown in **Figure 5.6**. The normal and tangential spring coefficients of the pipe model were sufficiently high for modeling a rigid pipe. The dimensions of the pipe and the test container were also the same as those of the experiment. **Table 5.2** summarizes the parameters of the pipe model.

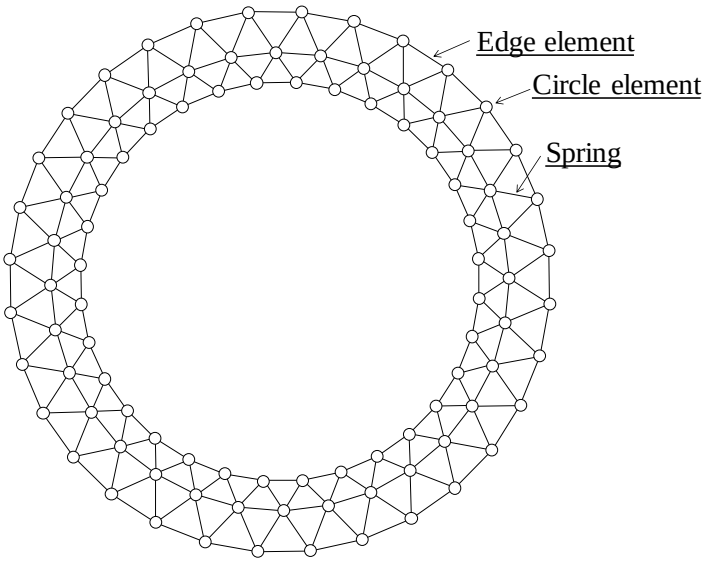

Figure 5.6 Pipe model

Table 5.2 Parameters of pipe model

Density of particle (kg/m^3)	40391
Normal spring coefficient (N/m)	1.0×10^9
Tangential spring coefficient (N/m)	2.5×10^7
Normal damping coefficient	0.5
Tangential damping coefficient	0.1
Friction coefficient of pipe surface	0.54

After making the soil bed, the soil particles located at the desired pipe location were deleted, and the pipe model was placed into the model. The finer soil particles (D_{50} = 3.0 mm) were placed around the pipe model to increase the number of particles in contact with the boundaries of the pipe. After the pipe model was placed, the self-weighted analysis was carried out for 5.0 s until the soil model reached static condition.

5.3.3 Analysis procedures

In the present analysis, liquefaction of the soil bed was simulated by the technique that used the upward seepage, done in the same manner as the model experiment. A constant head difference between the bottom and the top of the fluid mesh reproduced the upward

seepage from the bottom of the container to the ground surface. The saturated soil bed under different hydraulic gradients was simulated by giving the head difference corresponding to the hydraulic gradient. **Figure 5.7** shows the schematic diagrams of boundary and initial conditions for the fluid mesh. The hydraulic conductivity was obtained from the experiment on the basis of the Darcy's law from the hydraulic gradient and the measured flow rate. The dimension of the fluid mesh was determined by the mean size of the particles. Zeghal and Elshamy (2004) indicated that 3-4 times of the mean particle diameter was appropriate for the mesh dimension. In the present analysis, the rectangle fluid mesh: dx = 20 mm and dy = 25 mm was set to calculate the lateral fluid flow in more detail.

As stated above, the void ratio in two-dimensional DEM is much smaller than that of the model experiment. Therefore, the submerged unit weight of the soil and the critical hydraulic gradient are also smaller than the actual values. Thus, when considering saturation, the submerged density was raised by reducing the buoyancy acting on the particles, and the saturated unit weight was adjusted to be equal to that of the experiment.

After stabilizing the soil model for 5.0 s again under prescribed hydraulic gradient, the pipe model was displaced in the lateral direction with a loading rate of 1.0 mm/s. The degree of freedom in the pipe model was not restricted; lateral and vertical displacements and rotating motion were all allowed. Although the excess pore water pressure due to the

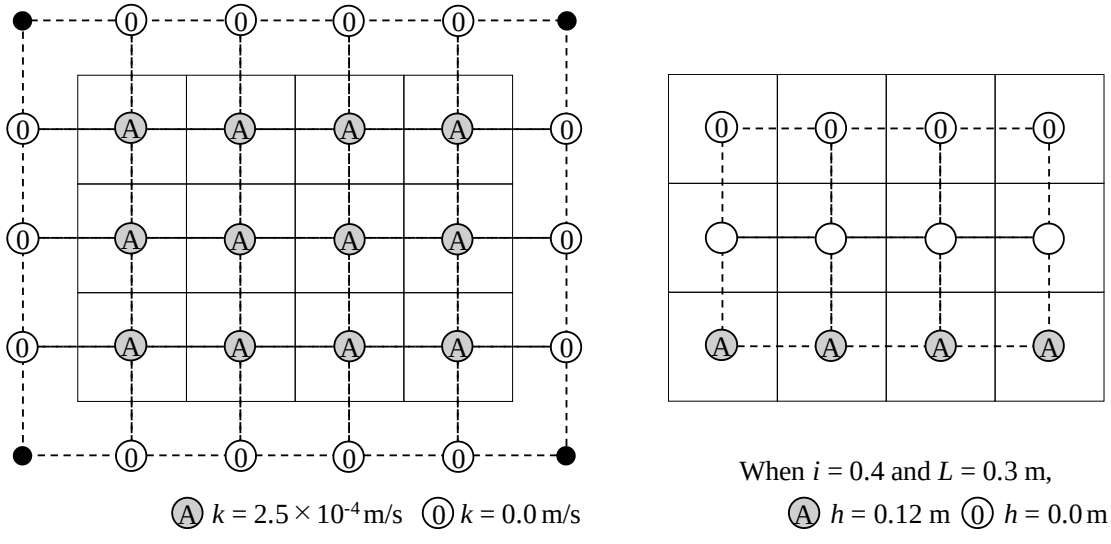

Figure 5.7 Schematic diagram of fluid mesh: (a) hydraulic conductivity and (b) water head

movement of the particles is calculated as written above, the water pressure due to the movement of the pipe needs a different algorithm. To calculate the excess pore water pressure, the displacement of the pipe is converted to the pore volume change in reference to Suehiro et al. (2003) as follows. Each fluid mesh including no particles is discriminated as an area where the pipe model is located, and the hydraulic conductivity of the meshes is changed to 0.0. The pore volume change is calculated as the product of the averaged displacement of the pipe and the dimension of the fluid mesh. Finally, the pore volume change is added to the mesh next to the pipe model, and the excess pore water pressure is calculated using Eq. (5.15).

In summary, the simulation of the lateral loading experiments consists of the following five steps:

1. The container was filled with the particles subjected to gravitational force, and then the soil model was stabilized for 1.0 s.
2. The soil particles located at the desired pipe location were deleted, and the pipe model was placed into the model. The soil model was stabilized for 5.0 s.
3. The density of each particle of the sand was adjusted to correspond to the submerged unit weight of the soil in the model experiment.
4. Constant head difference was applied to the fluid mesh between the top and the bottom for reproducing the upward seepage. The soil model was stabilized for 5.0 s again.
5. The pipe model was displaced laterally with a loading rate of 1.0 mm/s.

5.4 Simulation of Lateral Loading Experiment for Pipe

5.4.1 Calibration of soil parameters

Force-displacement relationship in dry condition is firstly examined. **Figure 5.8** shows the comparison of force-displacement curves with the experimental results of the dry sand. The lateral resistive force is obtained from the sum of the lateral components of the contact force acting on total 32 beams covering the pipe model. Note that the unit of the resistive force is expressed by force per unit length because of a two-dimensional analysis. As stated above, the soil parameters were determined by trial and error. We can confirm that the variation of the lateral resistive force with the displacement is generally well simulated in the

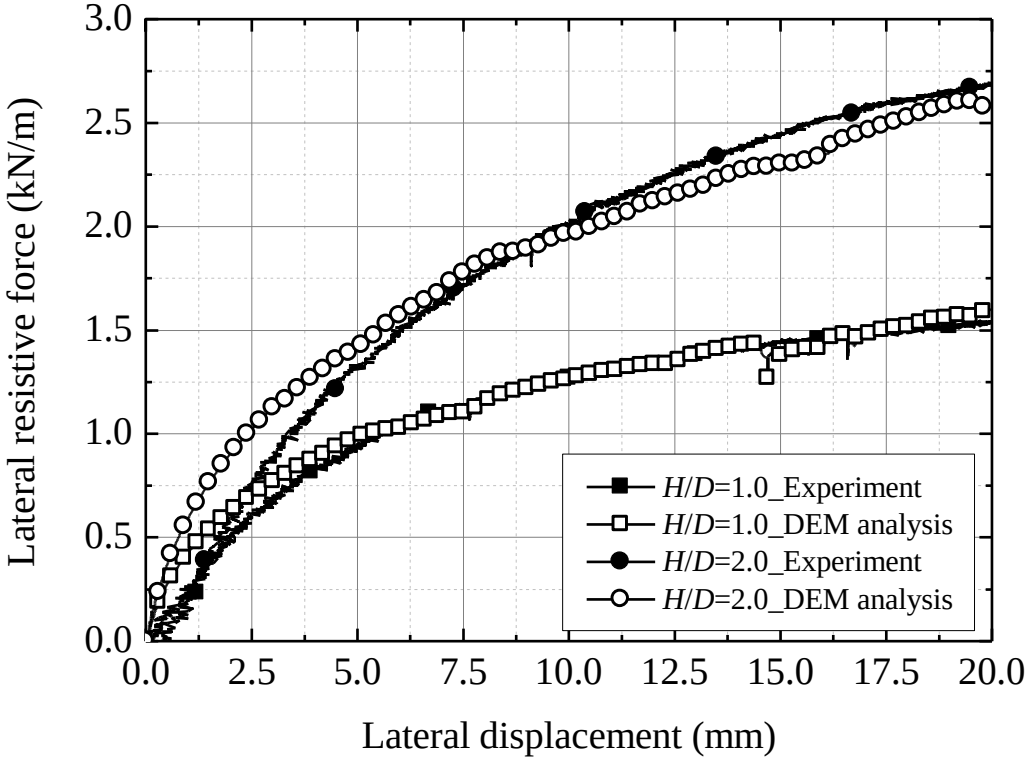

Figure 5.8 Comparison of force-displacement curve with experimental result of dry sand

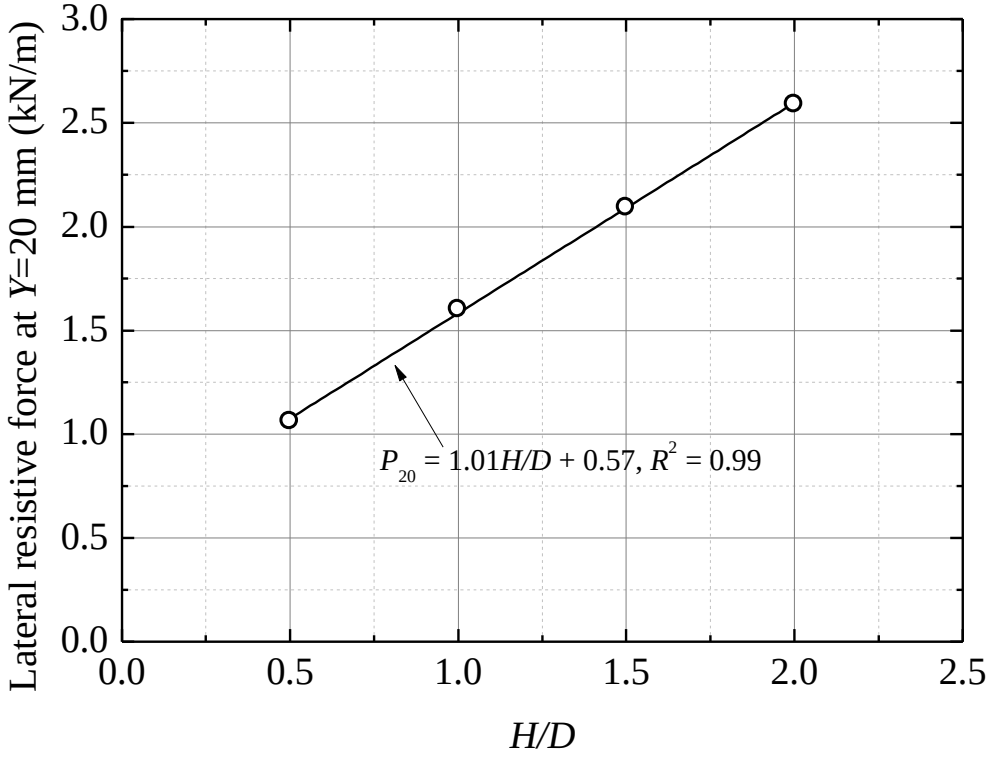

Figure 5.9 Variation of resistive force at Y = 20.0 mm with normalized depth

analysis. Although the resistive force in the DEM is slightly larger in the early stage of the lateral loading, and then it shows a gradual increase trend similar to the experiment.

Figure 5.9 shows the relationship between the resistive force at Y = 20.0 mm and the depth of soil cover normalized by the pipe diameter. Note that the parameters of soil model (e.g. spring coefficients) were not modified according to the depth of soil cover, and only confining pressure according to the burial depth is changing. The relationship shows that the resistive force varies linearly with the increase of the depth of soil cover, at least in the low stress state where the H/D is 2.0 or less. This result is attributed to the increase of the confining pressure of the soil in proportion to the depth. Note that a similar result was obtained in the DEM analysis performed by Yimsiri et al. (2006).

5.4.2 Upward seepage

Prior to the simulation of the lateral loading experiment in the saturated and liquefied soil, the influence of the upward seepage on the contact force between particles (effective stress) is examined. **Figure 5.10** shows the time history of the total number of contacts and the contact force in the vertical direction at i = 0.4 and 0.88 (critical hydraulic gradient). Note that the vertical contact force is the average of the force per mass (N/kg) calculated by dividing the sum of the vertical contact force acting on each particle by the mass of each particle. Assuming that the dry soil model is in a stable static state, the contact force per mass converges to the gravitational acceleration (9.8 N/kg) because the total of the vertical contact force acting on each particle is balanced with its own weight. The graph shows that both the number of contacts and the contact force start to decrease immediately after the upward seepage is applied. In both cases, the contact force is continuously changing and stabilizes after approximately 2.0 s. The number of contacts at the critical hydraulic gradient is reduced to approximately 80% of that of the saturated sand bed due to the influence of the fluid force.

Figure 5.11 shows the variation of the contact force in the vertical direction with the unit weight of the soil bed in the stable state after 5.0 s since the upward seepage is applied. The horizontal axis shows the effective unit weight calculated from the submerged unit weight and the hydraulic gradient. The vertical contact force decreases almost linearly from

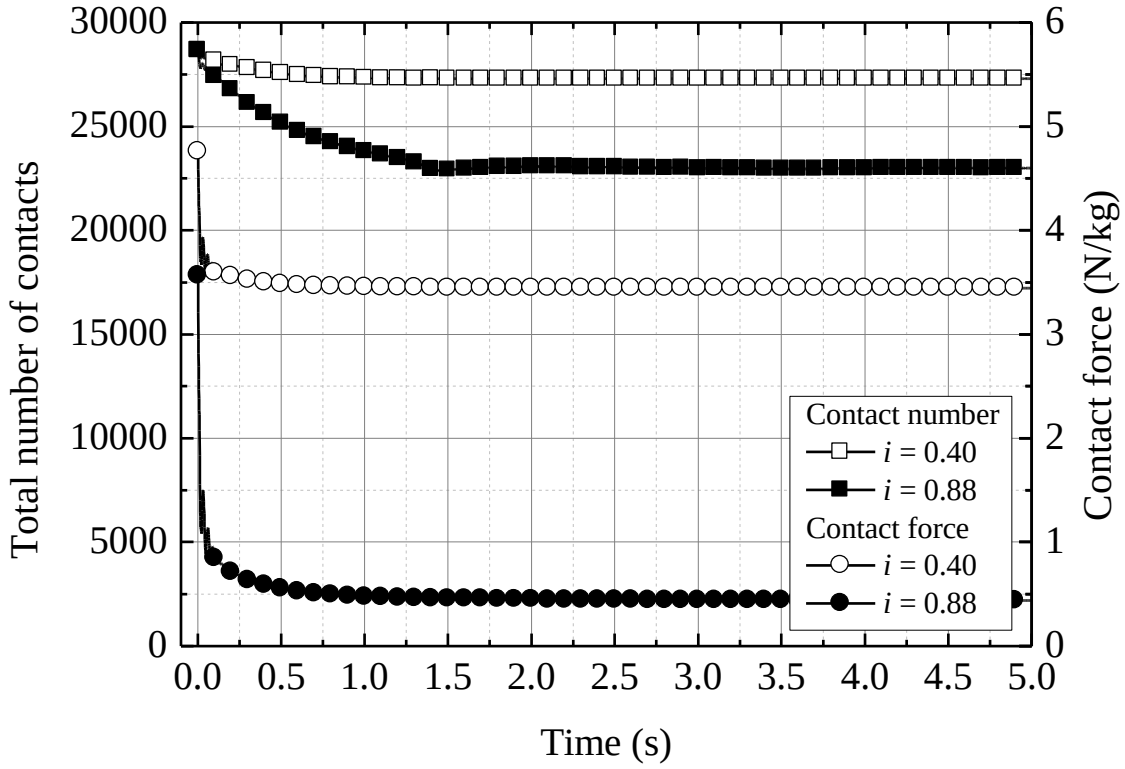

Figure 5.10 Time history of total number of contacts and contact force

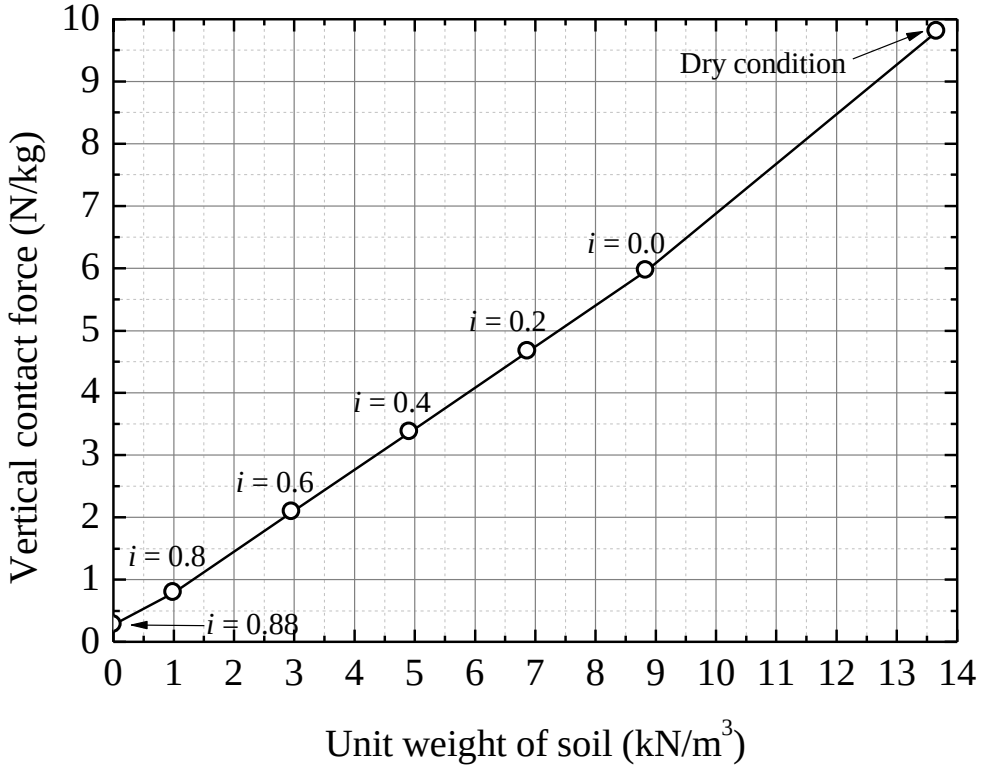

Figure 5.11 Variation of vertical contact force with effective unit weight

9.8 N/kg as the effective unit weight of the soil decreases. Although the contact force does not completely drop to zero even at i = 0.88 due to the friction with the wall of the container and the relatively large size of the fluid mesh, the gradual variation of the contact force is well represented by the upward seepage pressure that is expressed by the hydraulic gradient between fluid meshes.

5.4.3 Force-displacement relationship

After stabilizing the soil model under prescribed hydraulic gradient, lateral loading was carried out for the pipe model. **Figure 5.12** shows the comparison of force-displacement curves with the experimental results of the saturated sand at i = 0.0, 0.4, and 0.88. In any case, the variation of the nonlinear force-displacement relationship according to the hydraulic gradient is well simulated. Regardless of the depth of soil cover, each force-displacement curve shows very good agreement with the experimental result although the resistive force in DEM is slightly larger than that of the experiment in the early stage of loading. As with the experimental results, the lateral resistive force at the critical hydraulic gradient is extremely small: it decreases to 10% or less of that of the saturated sand. By reducing the contact force between particles due to the action of the upward seepage, it is possible to accurately reproduce the decrease of the lateral resistive force of the saturated sand.

5.4.4 Contact force and earth pressure

Figures 5.13 and **5.14** show the distributions of the normal contact force between the soil particles surrounding the pipe at i = 0.0 and 0.88, respectively. The normal contact force is calculated as the product of the overlapped length between the contacted particles and the normal spring coefficient. The figures show that the contact force develops radially toward the displacement direction of the pipe (rightward). The contact force increases with the lateral displacement of the pipe, and its range of influence is also expanding. On the other hand, the contact force at i = 0.88 drops much more than that of i =0.0. Although the range of influence is also sharply reduced, the development of the resistive force can still be visually recognized

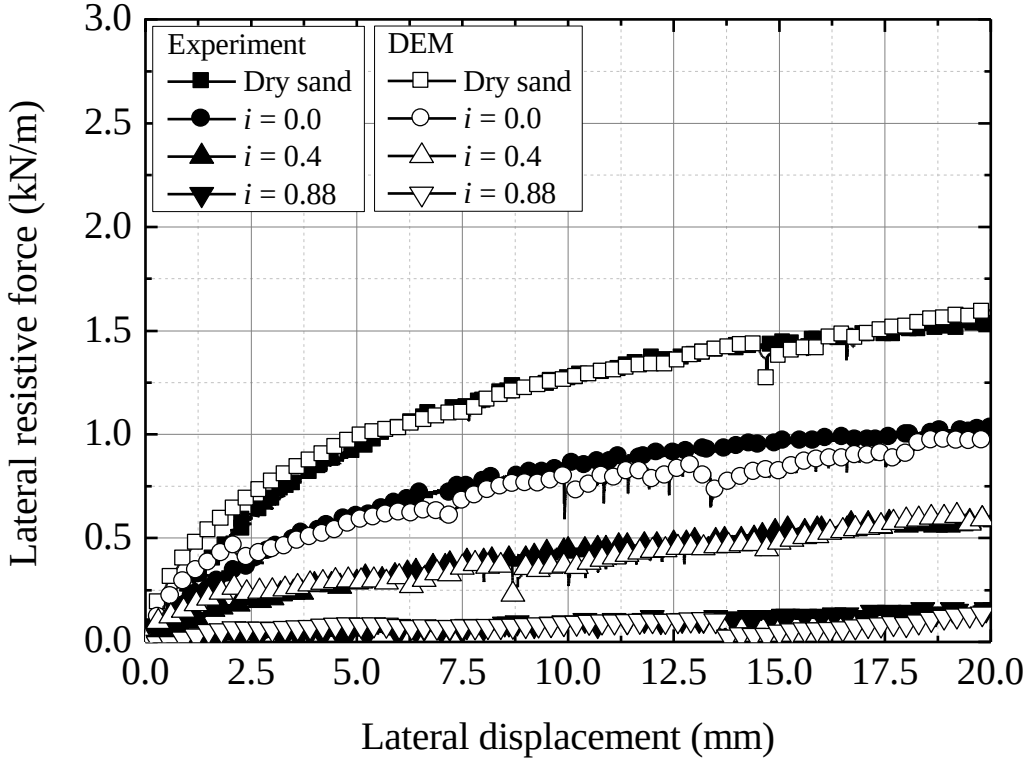

(a)

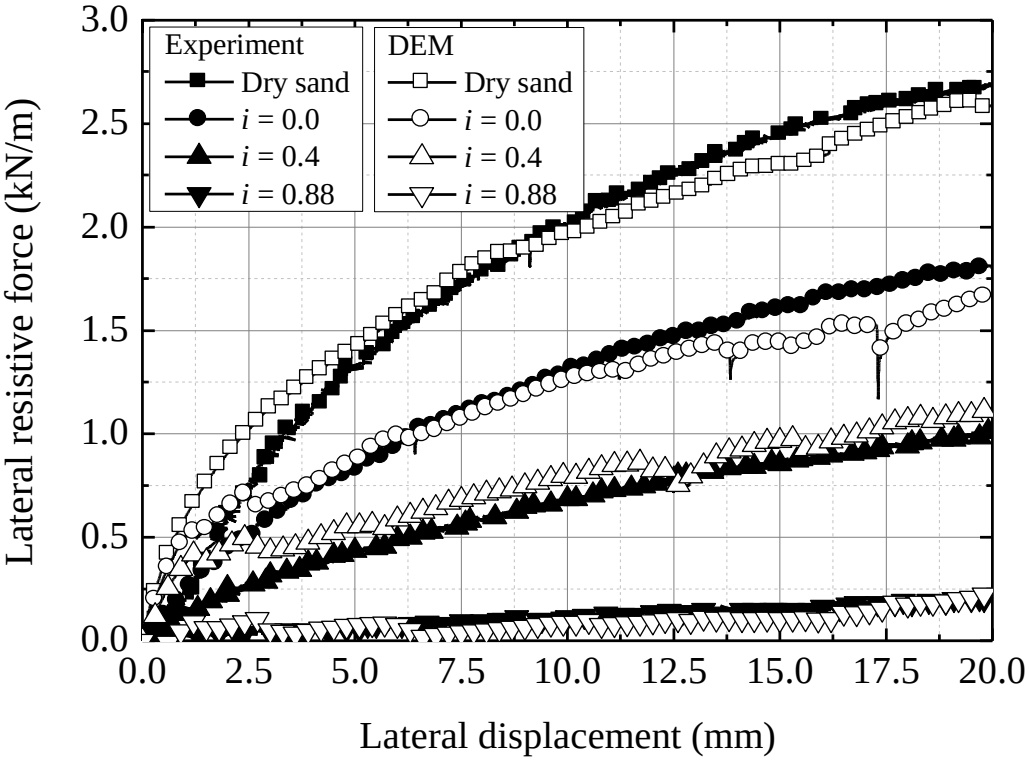

(b)

Figure 5.12 Comparison of force-displacement curve with model experiment in saturated sand:
(a) *H/D* = 1.0 and (b) *H/D* = 2.0

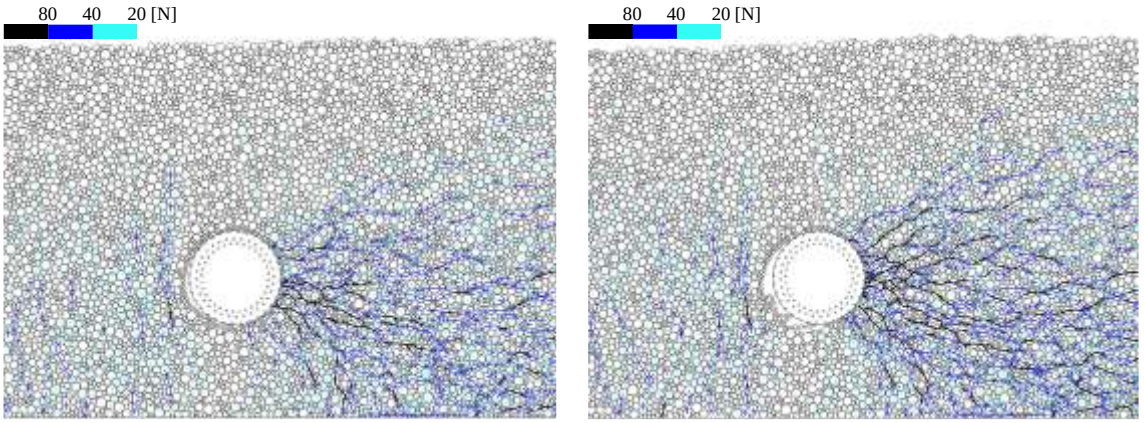

(a) (b)

Figure 5.13 Normal contact force at $i = 0.0$: (a) $Y = 10.0$ mm and (b) $Y = 20.0$ mm

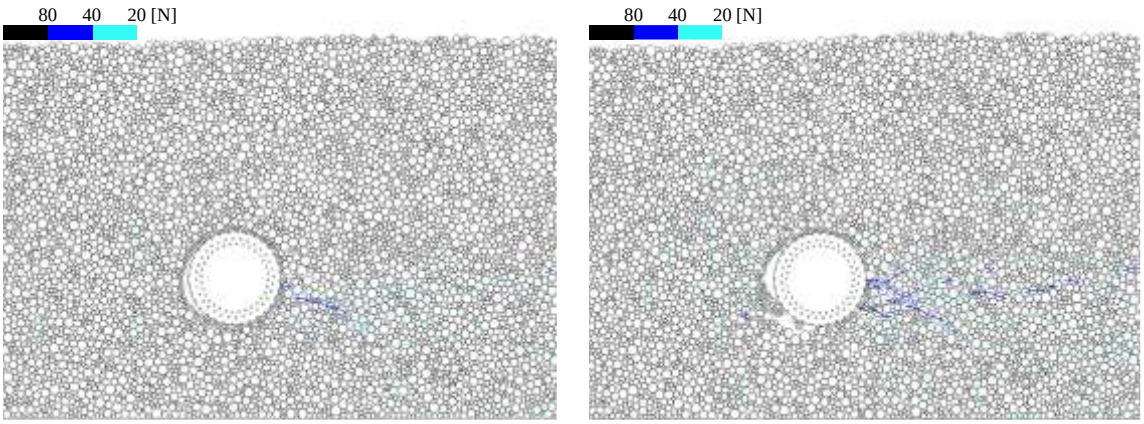

(a) (b)

Figure 5.14 Normal contact force at $i = 0.88$: (a) $Y = 10.0$ mm and (b) $Y = 20.0$ mm

on the side of the pipe. In both cases, the contact force develops slightly downward from the spring line of the pipe.

Figure 5.15 shows the horizontal component of the earth pressure acting on the right half of the pipe model. The lateral earth pressure is calculated by dividing the sum of the lateral force acting on each beam of the pipe by each horizontal projected area. The vertical axis of the graph represents the vertical height; 0.0 m in the graph represents the height of spring line of the pipe. The earth pressure at $Y = 0.0$ mm is regarded as the earth pressure at rest because the pipe model is rigid enough not to deform. Even though there is a slight irregularity depending on the contact condition between the particles and the pipe model, the earth pressure shows an almost uniform distribution. The earth pressure near the bottom of the pipe is quite large because the horizontally projected area close to this point is extremely

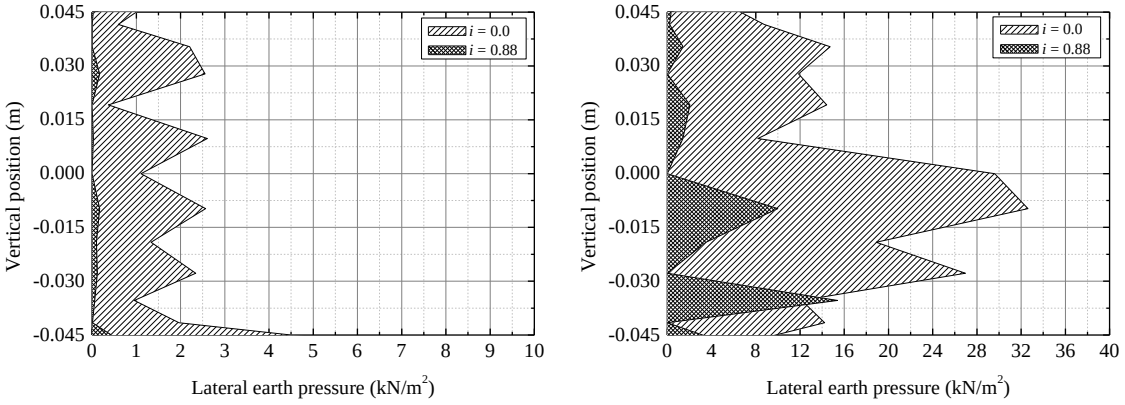

(a) (b)

Figure 5.15 Horizontal component of passive earth pressure acting on pipe model: (a) Y = 0.0 mm and (b) Y = 20.0 mm

small. The lateral earth pressure does not vary in the depth direction because of the relatively low confining pressure. The lateral earth pressure at the height of spring line in saturated condition calculated based on the Jaky's equation is approximately 1.0 kN/m^2 that is roughly equal to the analysis result.

On the contrary, the lateral passive earth pressure during lateral loading (Y = 20.0 mm) shows approximately a convex distribution. This largely differs from the trapezoid distribution based on Rankine's passive earth pressure proposed in the current design guideline in Japan (M.A.F.F., 2009). The lateral earth pressure at the side of the pipe is the largest and the one near the top and the bottom of the pipe is remarkably small because the frictional force at these positions decreases due to slippage. Therefore, the current design anticipates the excessive earth pressure that cannot be expected in practice. Kawabata et al. (2002) also obtained a similar convex distribution of the earth pressure from their model experiments. Moreover, the lateral passive earth pressure is somewhat larger under the spring line of the pipe. This distribution is determined from the confining pressure that depends on the burial depth. Although the earth pressure at i = 0.88 is much smaller than that of i = 0.0, the distribution shape is qualitatively the same.

5.4.5 Displacement of soil particles

Figures 5.16 and **5.17** show the distributions of the displacement of the soil particles

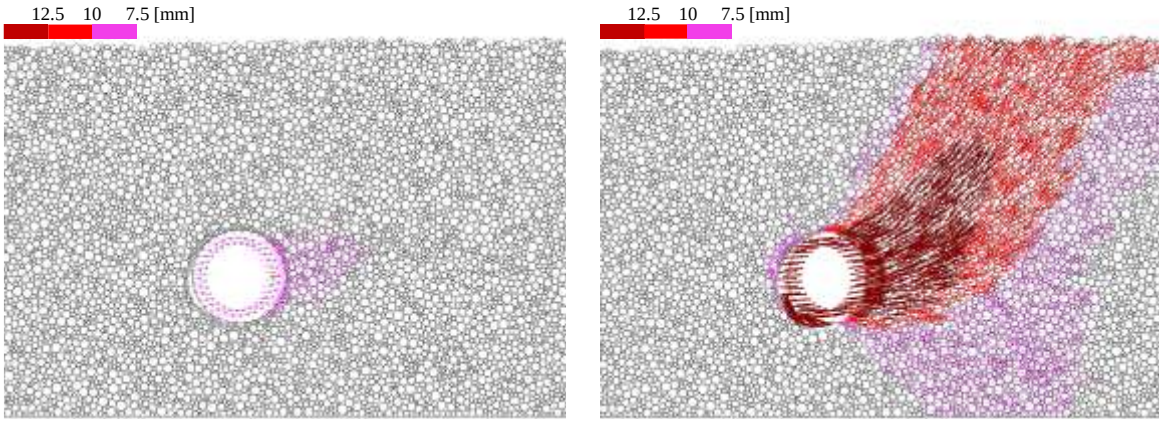

(a) (b)

Figure 5.16 Displacement of soil particles at i = 0.0: (a) Y = 10.0 mm and (b) Y = 20.0 mm

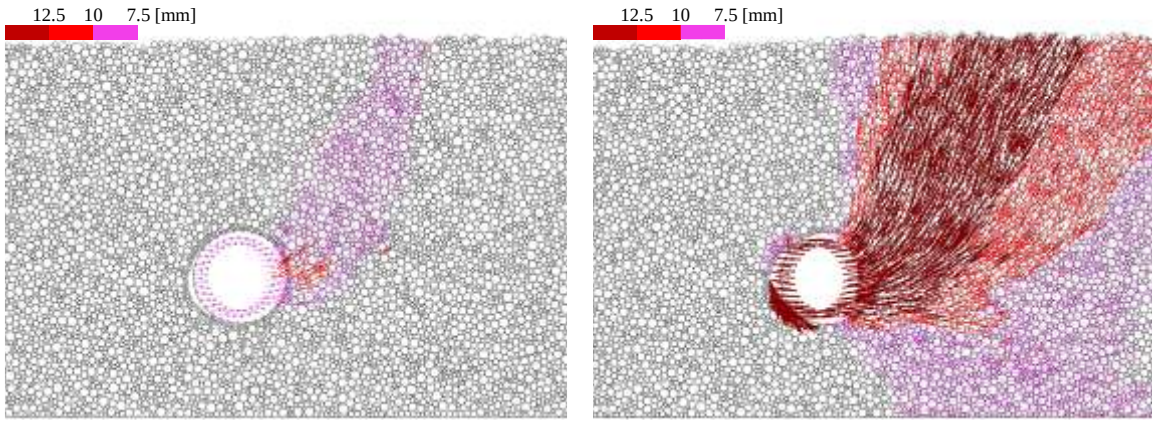

(a) (b)

Figure 5.17 Displacement of soil particles at i = 0.88: (a) Y = 10.0 mm and (b) Y = 20.0 mm

at i = 0.0 and 0.88, respectively. Each particle displacement is the variation from the initial position (Y = 0.0 mm). The distribution map shows that the soil particles on the passive side of the pipe are displaced and lifted up by the movement of the pipe. We can see a clear slip surface on the passive side toward the ground surface. The pipe is also floating with lateral displacement by receiving the support of the sand bed from the lower right as shown in **Figure 5.15**. The comparison between both cases indicates that the soil particles at i = 0.88 move more widely at any displacement although the displacement pattern does not show a complete fluid-like behavior. These are seemingly caused by the fluid force acting on the particles by the upward seepage and the excess pore water pressure generated by the movement of the particles.

5.4.6 Void ratio

Figures 5.16 and **5.17** qualitatively indicated that the movement characteristics of soil particles are different depending on the hydraulic gradient of the soil bed. Therefore, we calculate the void ratio of the soil around the pipe from the arrangement of the particles. **Figure 5.18** shows the variation of the void ratio with the lateral displacement of the pipe. The calculated range is within a semicircle on the passive side of the pipe with a radius of 100 mm from the center of the pipe (see **Figure 5.19**). At i = 0.0 and 0.4, the void ratio decreases at the beginning of the lateral loading by approximately 10%. This volume shrinkage is due to the occurrence of the negative dilatancy accompanying the pipe displacement. The volumetric strain calculated from the change in the void ratio is approximately 1.6%, indicating that the passive-side soil firstly displaces with a considerably large volume change. Subsequently, the variation of the void ratio turns to an increasing trend. This variation indicates that shear displacement occurs with volume expansion. This is the same as the trend generally observed during shear deformation of dense sand. Comparing the cases with different hydraulic

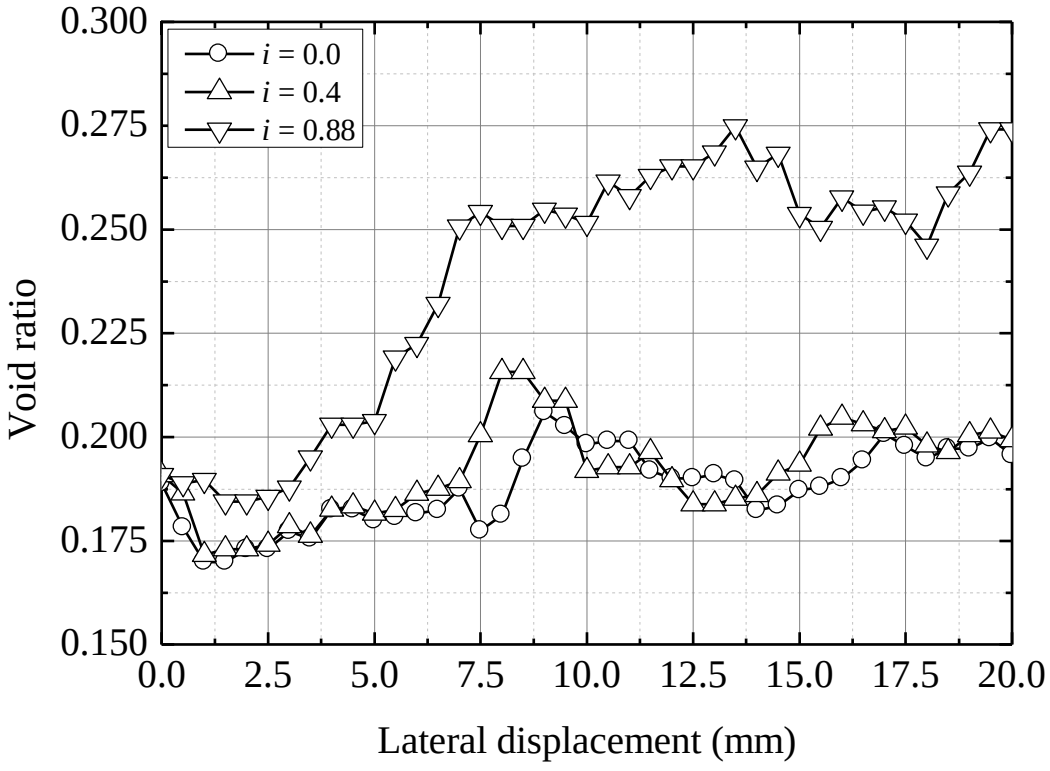

Figure 5.18 Variation of void ratio on passive side with lateral displacement

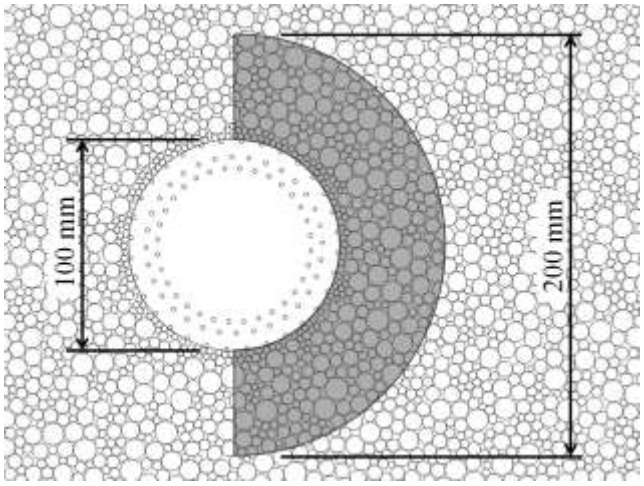

Figure 5.19 Radius of influence for calculation of void ratio

gradient, the void ratio at the critical hydraulic gradient increases by approximately 20% from that of the saturated sand. This difference seems to have been caused by the generation of the excess pore water pressure that prevents the movement of the soil particles.

5.4.7 Excess pore water pressure ratio

Figure 5.20 shows the variation of the excess pore water pressure ratio with the lateral displacement of the pipe and compares it with the experimental results. The excess pore water pressure ratio is calculated by dividing the pore water pressure of the fluid mesh by the initial effective overburden pressure before loading. Similar calculation is performed on the measured pore water pressure. The measurement position is 200 mm away from the right side of the pipe to the passive side. At $i = 0.0$, the excess pore water pressure ratio of the DEM shows a similar variation with that of the experiment. The ratio rises immediately after the displacement starts and then gradually decreases until it almost dissipates at $Y = 20.0$ mm. Although the calculated position is different, when compared with the variation of the void ratio, the excess pore water pressure rises when the passive-side soil is compressed. In the subsequent shear displacement process, the pore water pressure gradually dissipates with the volume expansion of the soil. Although the dissipation of the excess pore water pressure along the slip surface is expected, it was impossible to obtain a clear relationship between them in this analysis due to the size of the fluid mesh.

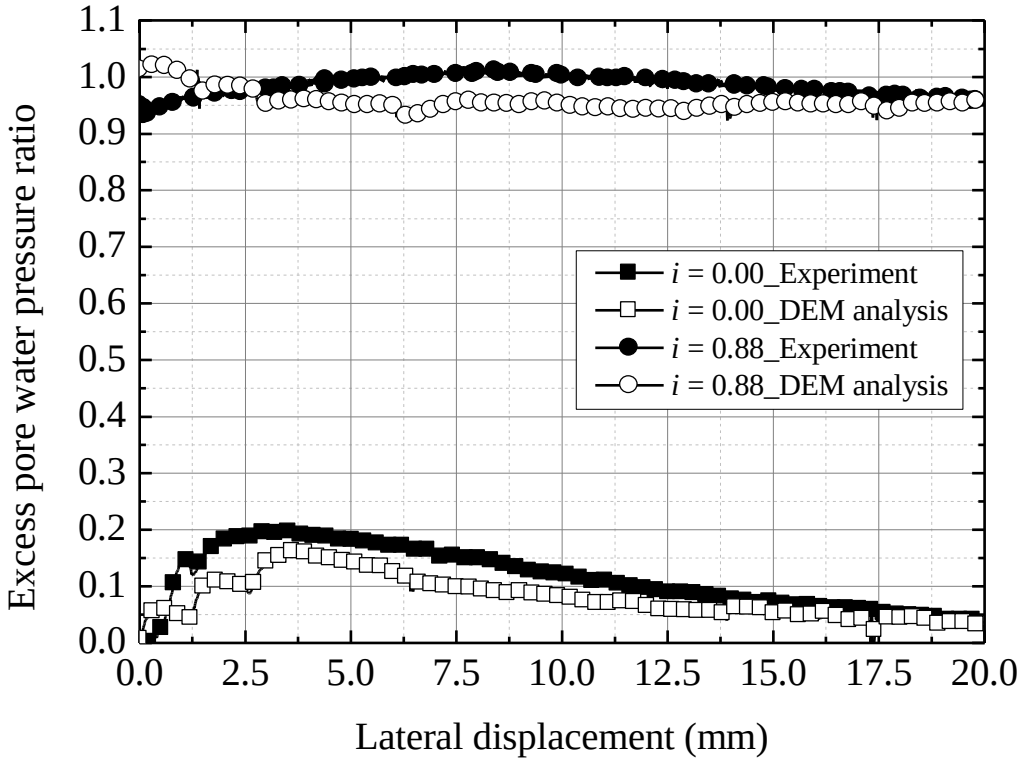

Figure 5.20 Comparison of excess pore water pressure ratio with model experiment

On the other hand, at $i = 0.88$, the variation of the excess pore water pressure ratio is slightly different between the experiment and the analysis. In the experiment, the excess pore water pressure increases until it reaches 1.0 and gradually decreases to 0.95 because there is an initial residual (effective stress) to raise the pore water pressure. In contrast, in the analysis, the water pressure decreases to approximately 0.95 immediately after slight rising, and then it remains constant. It can be considered that these water pressure changes include both the influence of the excess pore water pressure (volume shrinkage) and the upward seepage from the bottom of the soil model. Therefore, it is inferred that the reason why the water pressure change has settled down to a certain value is that these influences are balanced with each other.

5.5 Conclusions

In this chapter, two-dimensional DEM simulation was carried out on lateral loading experiments for a pipe buried in liquefiable sand. The fluid coupled-DEM program was

utilized to examine the lateral pipe-soil interaction under various effective stress conditions. The following conclusions were drawn.

1. The force-displacement curve of the pipe in dry sand was accurately simulated by adjusting the parameters of soil particles through trial and error. In the low stress state where *H/D* was 2.0 or less, the resistive force increased almost linearly with the increase of the depth of soil cover.
2. The upward seepage in the soil bed was reproduced by a constant head difference between the bottom and the top of the fluid meshes. The contact force between the soil particles decreased almost linearly as the effective unit weight of the soil model decreased. Although the contact force did not completely drop to zero even at critical hydraulic gradient, it was possible to reproduce the gradual variation of the contact force by the upward seepage.
3. The force-displacement curves obtained from the lateral loading simulation carried out in the soil bed with reduced contact force showed very good agreement with the experimental results. As with the experiments, the lateral resistive force at the critical hydraulic gradient decreased to 10% or less of that of the saturated sand.
4. The contact force between the soil particles developed radially toward the displacement direction of the pipe. At the high hydraulic gradient, both the contact force and its range of influence decreased. The horizontal earth pressure acting on the pipe during lateral displacement showed approximately a convex distribution that largely differed from a trapezoidal distribution proposed in the current design guideline.
5. The distribution map of the soil particles showed a clear slip surface on the passive side of the pipe. The soil particles moved more widely at high hydraulic gradient due to the action of the upward seepage and the excess pore water pressure.
6. At the beginning of the lateral loading, the void ratio of the soil on the passive side decreased by approximately 10% due to the negative dilatancy. Subsequently, the variation of the void ratio turned to an increasing trend. The void ratio at the critical hydraulic gradient increased by approximately 20% from that of the saturated sand due to the action of the excess pore water pressure.

7. The rise and dissipation of the excess pore water pressure with the pipe movement was observed on the passive side of the pipe. The variation of the water pressure was generally explained by the change of the void ratio.

References

Cundall, P. A. and Strack, O. D. L. 1979. A Discrete Numerical Model for Granular Assemblies, *Geotechnique*, 29(1), 47-65.

Kawabata, T., Mohri, Y., and Ling, H. I. 2002. Earth Pressure Distribution for Buried Pipe Bend Subject to Internal Pressure, *Proceedings of ASCE Pipeline Division Specialty Conference 2002*, CD-ROM.

Koyama, T., Moriguchi, S., Nakata, Y., and Matsushima, T. 2015. Discrete Element Method for Geoengineering 5, *Geotechnical Engineering Magazine*, 63(7), 49-56. (in Japanese).

Nakase, H., Takeda, T., and Oda, M. 1999, A Simulation Study on Liquefaction Using DEM, *Proceedings of 2nd International Conference of Earthquake Geotechnical Engineering*, 637-642.

Nakase, H., Honda, A., and Nishino T. 2001. Simulation of Torsional Shear Test for Setting Frictional Parameters in DEM, *Proceedings of 36th Japan National Conference on Geotechnical Engineering*, 503-504.

Nakase, H., Miyata, M., Nagao, T., Honda, A., Kyono T., Yasuda, K., and Sugano, T. 2002. Application of DEM to Deformation Analysis for Caisson Type Breakwater, *Journal of Applied Mechanics*, 5, 461-472. (in Japanese with English summary).

Matsushima, T., Maeda, K., Moriguchi, S., and Nakata, Y. 2015. Discrete Element Method for Geoengineering 4, *Geotechnical Engineering Magazine*, 63(6), 55-62. (in Japanese).

Ministry of Agriculture, Forestry and Fisheries of Japan (MAFF). 2009. Planning and Design Criteria of Land Improvement Project (Pipeline), JSIDRE, 321-409.

Moriguchi, S., Maeda, K., Matsushima, T., and Nakata, Y. 2015. Discrete Element Method for Geoengineering 3, *Geotechnical Engineering Magazine*, 63(5), 52-60. (in Japanese).

Sakaguchi, H., Ozaki, E., and Igarashi, T. 1993. Plugging of the Flow of Granular Materials during the Discharge from a Silo, *International Journal of Modern Physics B*, 7(9-10), 1949-1963.

Shafipour, R. and Soroush, A. 2008. Fluid Coupled-DEM Modeling of Undrained Behavior of Granular Media, *Computers and Geotechnics*, 35, 673-685.

Suehiro, T., Nakase, H., Mohri, Y., and Yasuda, S. 2003. Shaking Table Test to Underground Structures and

Simulation Study on Mechanism of Uplifting Using Distinct Element Method, *JSCE Journal of Earthquake Engineering*, 27, 1-8. (in Japanese with English summary).

Suzuki, Y. 2006. Three-Dimensional Simulation Using Fixed Coarse-Grid Thermal-Fluid Scheme and Conduction Hear Transfer Scheme in Distinct Element Method, *Powder Technology*, 165, 140-152.

Tarumi, Y. and Hakuno, M. 1988. A Granular Assembly Simulation for the Dynamic Liquefaction of Sand, *Natural Disaster Science*, 10(1), 45-59.

Yimsiri, S. and Soga, K. 2006. DEM Analysis of Soil-Pipeline Interaction in Sand under Lateral and Upward Movements at Deep Embedment, *Journal of Southeast Asian Geotechnical Society*, 37, 83-94.

Zeghal, M. and Shamy, U. E. 2004. A Continuum-Discrete Hydromechanical Analysis of Granular Deposit Liquefaction, *International Journal for Numerical and Analytical Methods in Geomechanics*, 28, 1361-1383.

CHAPTER 6

The contents of this chapter are based on:

Ono, K., Yokota, Y., Sawada, Y., and Kawabata, T. 2017. Lateral Force-Displacement Prediction for Buried Pipe under Different Effective Stress Condition, *International Journal of Geotechnical Engineering* (published online).

Ono, K., Yokota, Y., Ohta, Y., Sawada, Y., and Kawabata, T. 2017. Lateral Loading Experiment for Pipe-Soil Interactions in Liquefied Sandy Soil, *Proceedings of Pipeline 2017*, ASCE (submitted).

Chapter 6

Design for Thrust Restraint during Liquefaction

6.1 Introduction

In the present design guideline for agricultural pipelines, the safety factor for the displacement of the buried pipeline is defined as the ratio of the thrust force to the resultant force of the Rankin's passive earth pressure acting on the pipe bend. Although it is clear that the passive earth pressure varies according to the displacement of the buried pipe, the equilibrium between the thrust force and the passive earth pressure is only evaluated, and the displacement of the buried pipe is not considered at all. Therefore, the present design is not very rational. Furthermore, we should also consider the dramatic variation of the resistive force due to the decrease of the effective stress at the site where liquefaction potential is sufficiently high.

This chapter verifies more rational design method considering the variation of the passive earth pressure with the displacement of the buried pipe. First, a force-displacement curve that takes into account the variation of the effective stress is formulated based on hyperbolic approximation. Subsequently, a limit-state design method considering the relationship with the thrust force and the variation of the effective stress is proposed based on the allowable displacement of the pipe. The entire design flow and the calculation examples are shown.

6.2 Lateral Force-Displacement Prediction

6.2.1 Normalized force-displacement relationship

Force-displacement relationships are often approximated by hyperbolic curves to predict the peak resistive force mathematically (e.g. Audibert and Nyman, 1977). The normalized force-displacement relationships were fitted by the following equation:

$$\frac{P}{P_u} = \frac{Y/Y_u}{a + bY/Y_u} \tag{6.1}$$

where P is the lateral resistive force (kN), P_u is the ultimate resistive force (kN), Y is the lateral displacement (m), and Y_u is the ultimate lateral displacement (m). Coefficients a and b are the parameters that determine the curve of the hyperbola. Their inverses, $1/a$ and $1/b$, represent the initial tangential gradient and the asymptotic value, respectively.

As shown in **Figure 4.7**, the peak forces in the medium-density soil were difficult to determine because the lateral resistive force was gradually increasing with the lateral displacement. Trautmann and O'Rourke (1985) investigated the influence of the depth of soil cover on the ultimate displacement by means of 1*g* model tests on three types of ground density, and suggested the following empirical equations:

$$\begin{cases} Y_u = 0.13H' & (\textit{for loose}) \\ Y_u = 0.08H' & (\textit{for medium}) \\ Y_u = 0.03H' & (\textit{for dense}) \end{cases} \tag{6.2}$$

where *H'* is the depth to the center of the pipe (m). In the present study, the second formula was selected to determine the ultimate displacement of the medium soil. The ultimate displacements calculated from Eq. (6.2) were 12.0 mm and 20.0 mm for H/D = 1.0 and 2.0, respectively. The lateral resistive force measured at the ultimate displacement was defined as the ultimate resistive force.

Figure 6.1 shows the normalized hyperbolic force-displacement curves. The normalized force-displacement relationships differ widely depending on the hydraulic gradient. The initial resistive force decreases in accordance with the increase of the hydraulic gradient. It is well known that normalized force-displacement relationships result in similar hyperbolic curves without depending on the ground density, the diameter of the pipe or the

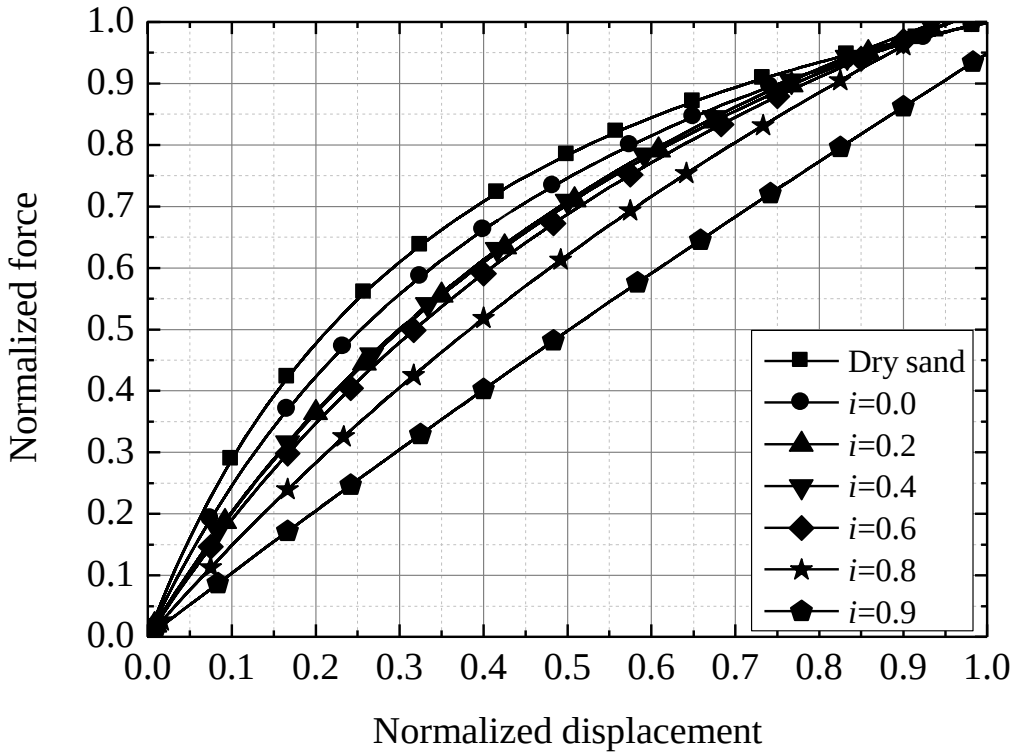

(a)

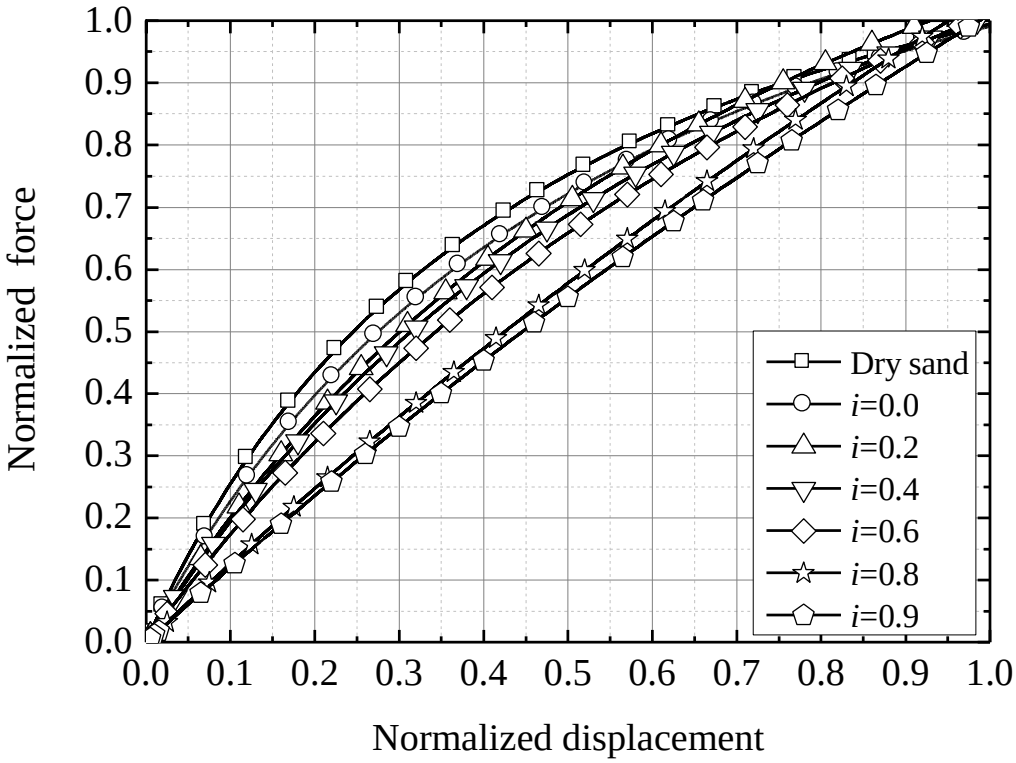

(b)

Figure 6.1 Normalized hyperbolic force-displacement curve:
(a) H/D = 1.0 and (b) H/D = 2.0

depth of soil cover (Audibert and Nyman, 1977). Therefore, the obtained normalized hyperbolic curves imply that the excess pore water pressure influences the ultimate displacement.

As stated above, the ultimate resistive force was difficult to determine with the present soil density. Thus, rather than looking directly at the influence of the excess pore water pressure on the ultimate displacement, its effect was attempted to see on the coefficients *a* and *b*. The decrease in submerged unit weight due to excess pore water pressure is given as

$$\gamma' = \gamma'_0 - i_{cr} \frac{\Delta u}{\gamma'_0 z} \gamma_w \tag{6.3}$$

where γ' is the submerged unit weight of the soil taking into account the excess pore water pressure ratio (kN/m^3), γ'_0 is the initial submerged unit weight of the soil (kN/m^3), i_{cr} is the critical hydraulic gradient, Δu is the increment of the excess pore water pressure (kN/m^2), z is the depth from the ground surface (m), and γ_w is the unit weight of water (kN/m^3).

Figure 6.2 shows the variations of the coefficients *a* and *b* with unit weight of the soil. The graphs indicate that coefficient *a* increases as the unit weight of the soil decreases. In other words, the initial lateral resistive force decreases as the effective stress of the soil decreases. In contrast, coefficient *b* decreases as the unit weight of the soil decreases because the force-displacement relationship approaches a linear one as the hydraulic gradient is increased, as can be seen in **Figure 6.1**. Moreover, it should be noted that the depth of soil cover had no influence on either coefficient, judging from a comparison of the plots in both cases. The relationships between each coefficient and the unit weight of the soil were also approximated nonlinearly as following hyperbolic curves:

$$a = 1 - \left(\frac{\gamma'}{2.36 + 1.25\gamma'} \right) \tag{6.4}$$

$$b = \frac{\gamma'}{2.68 + 1.22\gamma'} \tag{6.5}$$

6.2.2 Bearing capacity factor

Figure 6.3 shows direct proportional relationships between the unit weight of the soil

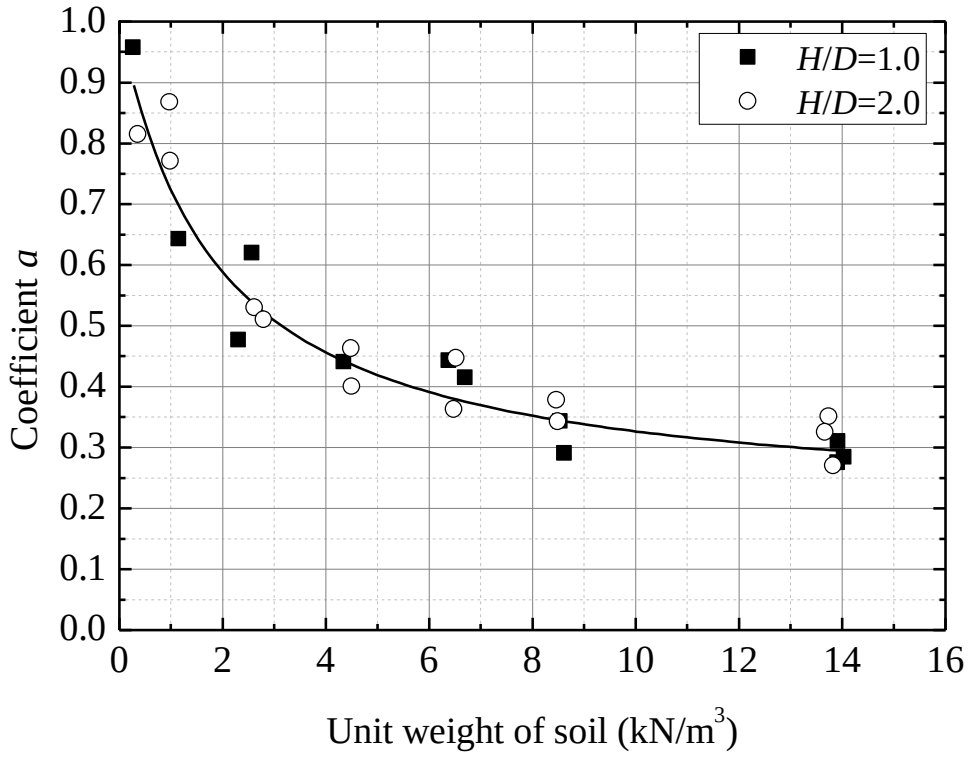

(a)

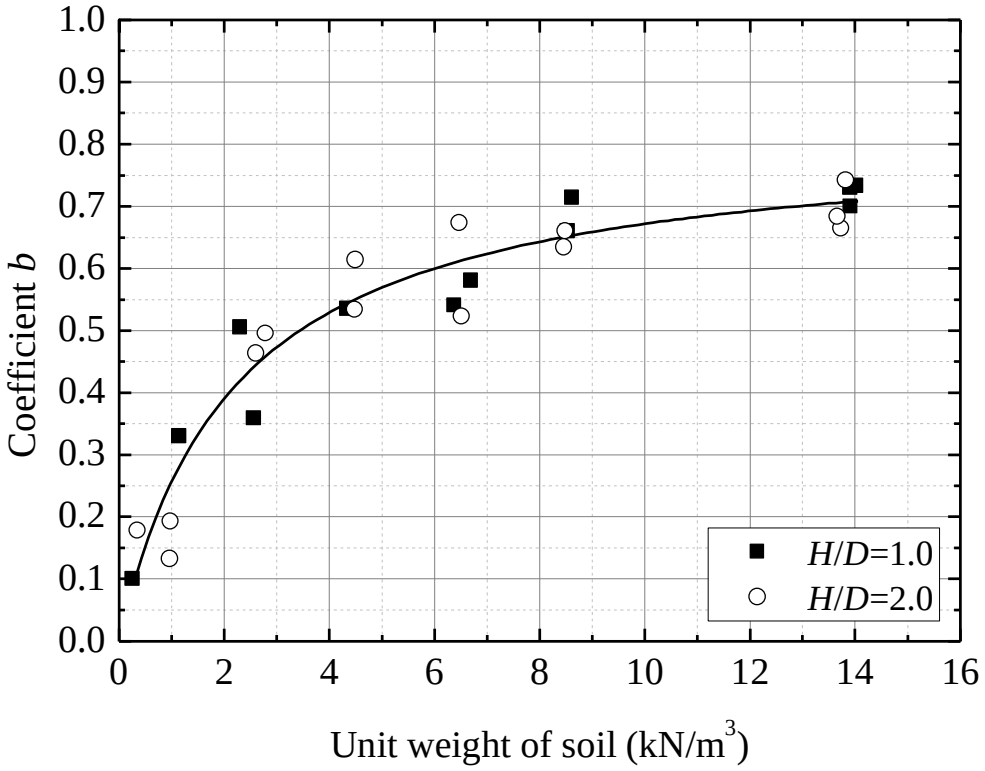

(b)

Figure 6.2 Variation of coefficients (a) *a* and (b) *b* with effective unit weight of soil

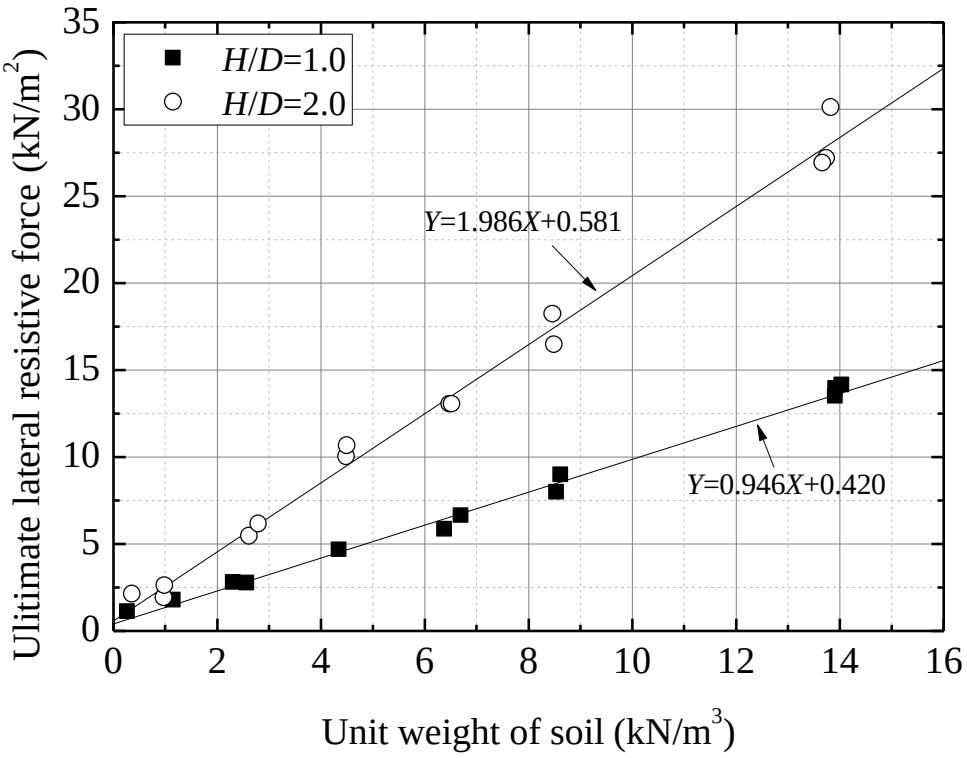

Figure 6.3 Variation of ultimate lateral resistive force with effective unit weight of soil

and the ultimate lateral resistive force. The ultimate resistive force in the case of H/D = 2.0 is roughly twice that of H/D = 1.0, judging from the gradient of the fitted lines. This result is attributed to the increase in the confining pressure of the soil bed in proportion to the depth of soil cover.

The bearing capacity factor is a dimensionless quantity that is calculated from the ultimate lateral resistive force. The bearing capacity factor defined as follows is well known to vary with the internal friction angle, the diameter of the pipe and the depth of soil cover (e.g. Hansen, 1961):

$$N_h = \frac{P_u}{\gamma' DH'L} \tag{6.6}$$

where P_u is the ultimate lateral resistive force (kN), γ' is the submerged unit weight of the soil taking into account the excess pore water pressure ratio (kN/m^3), D is the diameter of the pipe (m), H' is the depth to the center of the pipe (m), and L is the length of the pipe (m).

Figure 6.4 shows the variations of the bearing capacity factor with the unit weight of the soil. The graph indicates that the bearing capacity factor is effectively constant except for

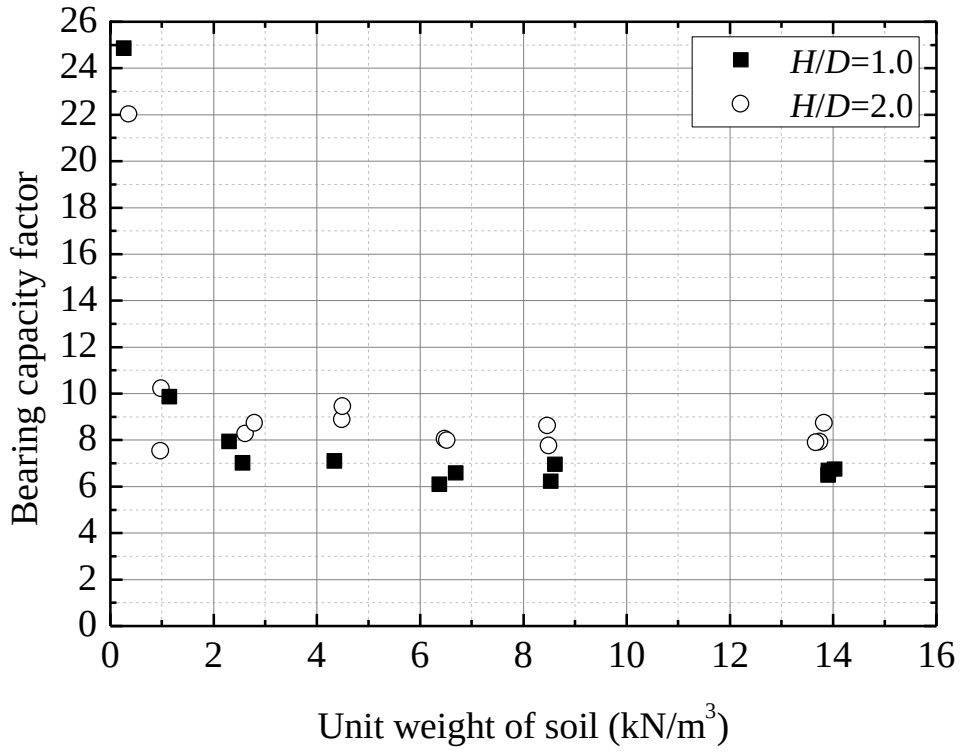

Figure 6.4 Variation of bearing capacity factor with effective unit weight of soil

the smallest unit weights, for which the ultimate resistive force is directly proportional to the unit weight as shown in **Figure 6.3** and the other parameters in Eq. (6.6) are constant. The average bearing capacity factors (excluding the excessively large values) were approximately 6.5 and 8.0 for H/D = 1.0 and H/D = 2.0, respectively.

Figure 6.5 shows the chart of bearing capacity factor obtained theoretically by Ovesen (1964), in which the bearing capacity factor is determined by selecting the internal friction angle and the normalized depth. When selecting an internal friction angle (40.0^o) that was roughly equal to the angle obtained by the triaxial compression tests, the bearing capacity factors calculated in the experiment were in very good agreement with the theoretical factors.

6.2.3 Prediction of force-displacement curve

Finally, the following force-displacement relationship can be obtained by substituting Eqs. (6.2) – (6.6) into Eq. (6.1):

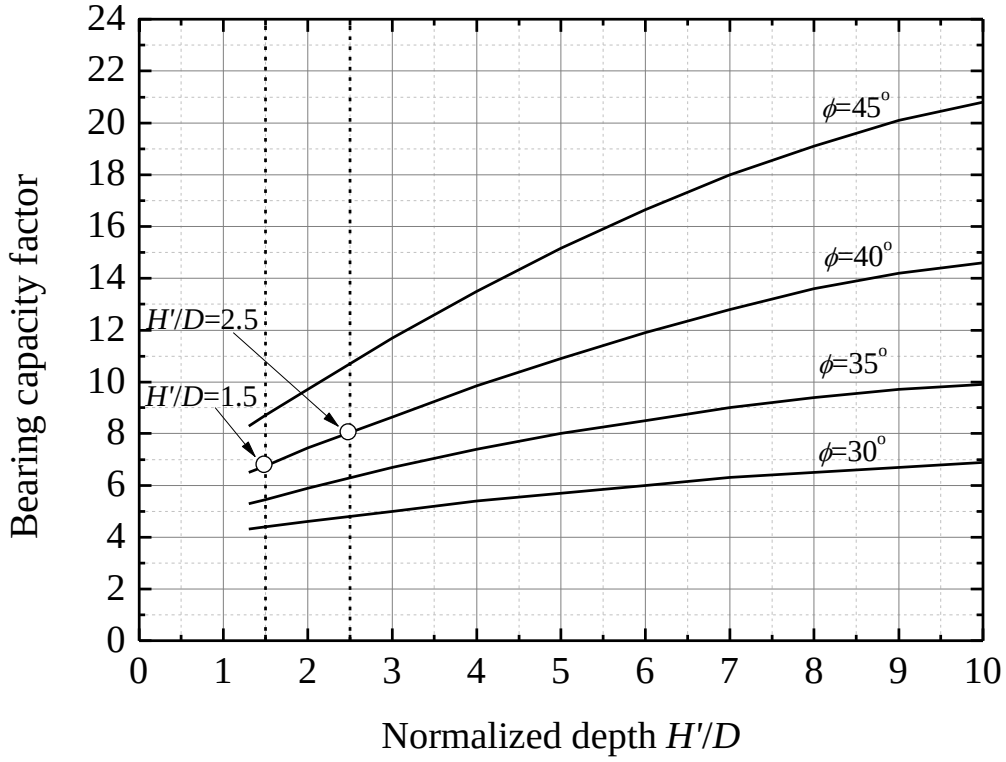

Figure 6.5 Variation of bearing capacity factor with normalized depth for different values of internal friction angle (Ovesen, 1964; modified by the author)

$$\frac{P}{DL}=\frac{N_h\gamma' H' Y}{\left(1-\frac{\gamma'}{(2.36+1.25\gamma')}\right)Y_u+\left(\frac{\gamma'}{2.68+1.22\gamma'}\right)Y} \tag{6.7}$$

Note that Eq. (6.7) takes into account the variation in the unit weight of the soil with the excess pore water pressure ratio, the depth of soil cover, the diameter and the length of the pipe.

Figure 6.6 compares the experimental results with the values predicted from Eq. (6.7). The solid lines and the symbols represent the predicted values and the experimental results, respectively. The predicted values fit relatively well to the experimental results, although the formers are slightly smaller when the displacement of the pipe is large. This difference is attributed to the fact that the hyperbolic curves of Eq. (6.1) were normalized within a limited range based on the ultimate lateral displacement obtained in Eq. (6.2). Although Eq. (6.7) was based on very limited experimental results, the force-displacement relationship can help us to predict the displacement of the pipe even in a soil bed with a different effective stress.

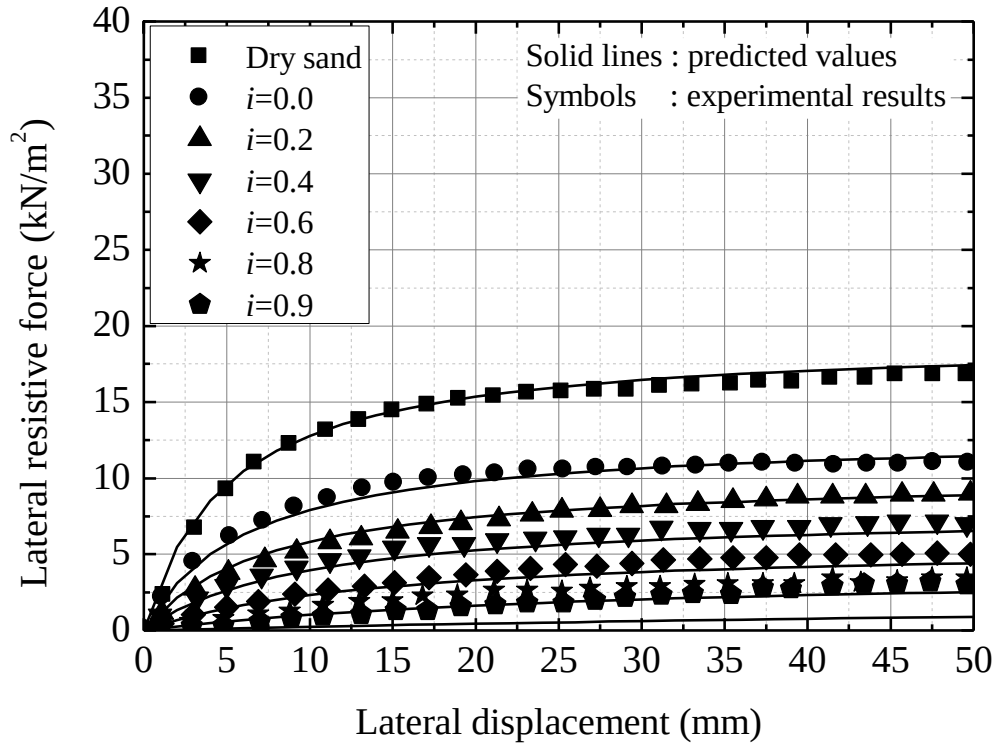

(a)

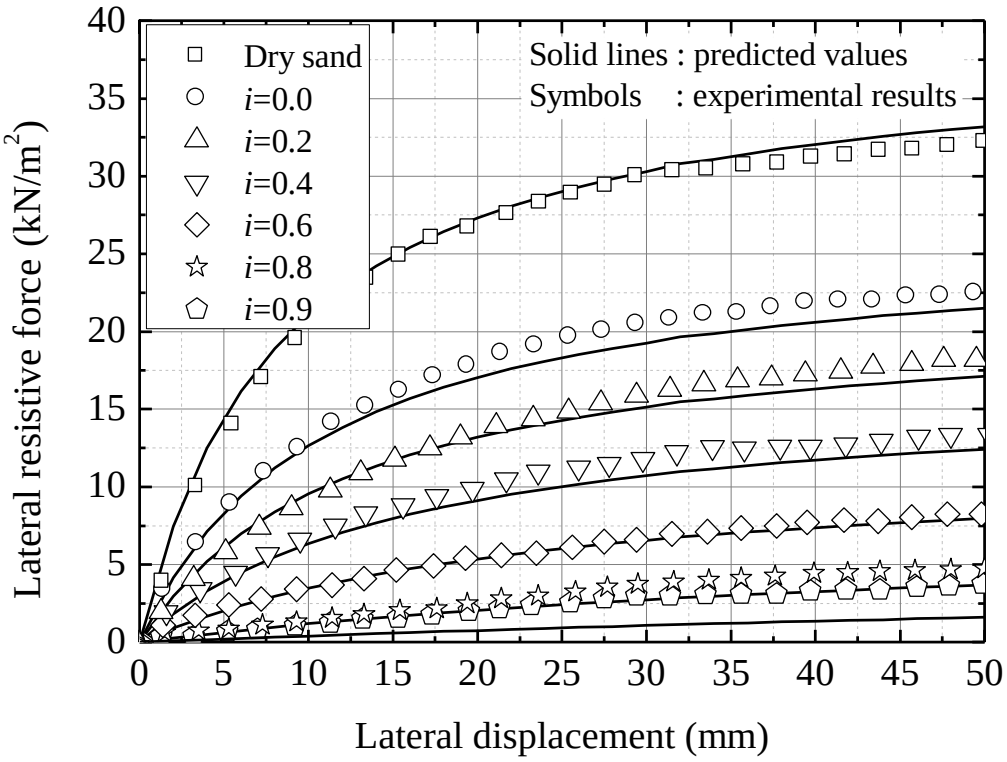

(b)

Figure 6.6 Comparison of predicted values with experimental results: (a) H/D = 1.0 and (b) H/D = 2.0

6.3 Proposal for Design Method

6.3.1 Design flow

Figure 6.7 shows the design flow. First, the thrust force P_t and the allowable lateral displacement of the pipe Y_{max} are calculated to verify the pipeline stability against the thrust force. The allowable displacement is calculated from the maximum elongation of each joint. By substituting the thrust force into the force-displacement curve determined from the backfilling condition, the displacement of the pipe bend generated by the thrust force Y_t is obtained. After considering the safety factor, it is judged whether the displacement of the pipe bend by the thrust force is less than the allowable displacement. In case the displacement exceeds the allowable one, the thrust restraint method is applied and recalculation is performed.

Subsequently, the pipeline stability considering the reduction of the resistive force due to liquefaction is verified. By substituting the thrust force and the allowable displacement including the safety factor into the force-displacement curve, the minimum effective unit weight of the soil γ'_{min} is obtained. As long as the effective unit weight of the soil is kept, the displacement due to the thrust force is less than the allowable displacement. After classifying the ground conditions according to the liquefaction potential, it is judged whether the effective unit weight exceeds the minimum effective unit weight. In case the effective unit weight is not satisfied, the thrust restraint using gravel or geogrid is applied. Each examination item is described in detail below.

6.3.2 Allowable displacement of pipe bend

The pipeline stability during earthquake depends on whether the joint is detached or not. Therefore, it is necessary to establish a design in consideration of the maximum (allowable) elongation of the joint so as not to cause the detachment. The specific calculation procedure is shown below.

First, the maximum elongation of the joint is converted into the lateral displacement of the pipe bend, and this is defined as the allowable lateral displacement. Subsequently, the

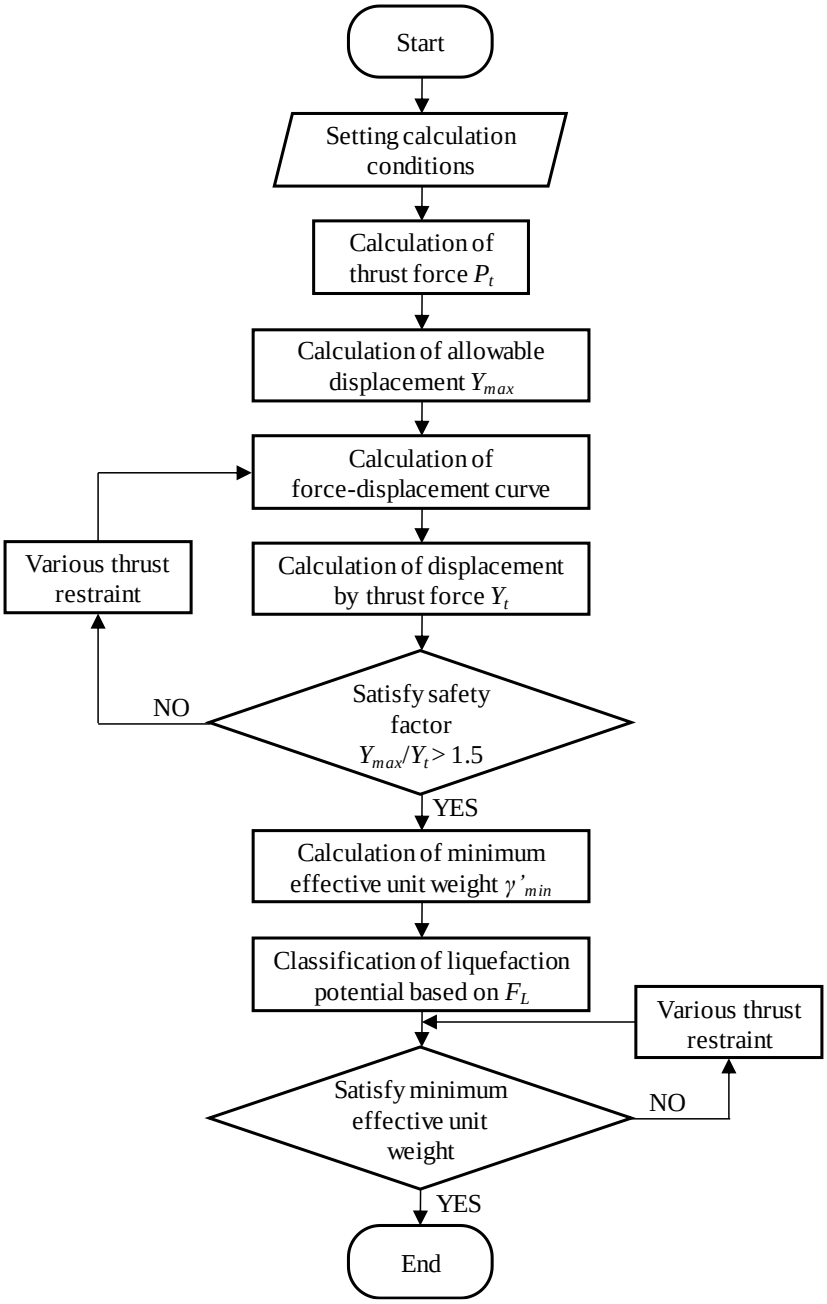

Figure 6.7 Design flow

displacement of the pipe bend generated by the thrust force is calculated and is compared with the allowable displacement. The allowable displacement is calculated based on a line model for a general flexible jointed pipeline as shown in **Figure 6.8** in reference to Itani et al. (2016). According to the earthquake damage investigation (e.g. Mohri et al., 1995) or model experiments with flexibly jointed pipe (e.g. Itani et al., 2015), it is clear that the detachment of the pipeline is likely to occur at a joint with a straight pipe connected to a pipe bend (see **Figure 6.8**). Therefore, this model assumes that the joint elongates on the neutral axis of the

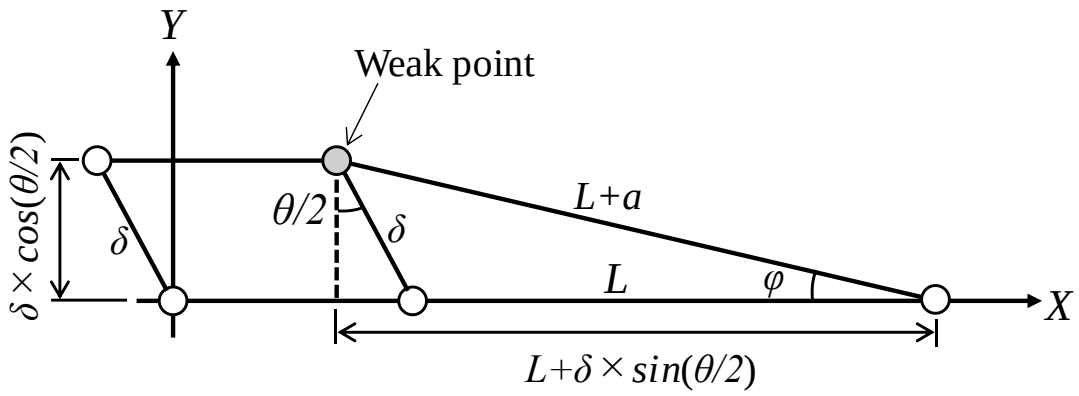

Figure 6.8 Line model for calculation of allowable displacement of pipe bend

pipe due to the displacement of the pipe bend. Moreover, assuming that this elongation is equally shared by two joints on both sides of the straight pipe and the length of the pipe bend does not change. The formulation of the elongation of the joint E_j is shown as

$$E_j = \sqrt{\left(L_s + \delta \sin\frac{\theta}{2}\right)^2 + \left(\delta \cos\frac{\theta}{2}\right)^2} - L_s \tag{6.8}$$

where L_s is the length of the straight pipe (m), δ is the displacement of the pipe bend (m), and θ is the angle of the pipe bend (^{o}).

Furthermore, the elongation of the joint needs to be corrected according to the detachment on the back side of the pipe depending on the opening at the joint. The bending angle of the joint φ is determined geometrically by the following formula:

$$\varphi = \cos^{-1}\left(\frac{L_s + \delta \sin\frac{\theta}{2}}{L_s + E_j}\right) \tag{6.9}$$

Since the opening at the joint is determined from the diameter and the bending angle of the joint, the maximum elongation of the joint E_{max} is expressed as

$$E_{\max} = \frac{E_j}{2} + \frac{D}{2}\sin\varphi \tag{6.10}$$

where D is the diameter of the pipe (m). After deforming Eqs. (6.8) – (6.10) for the displacement of the pipe bend, the allowable lateral displacement of the pipe bend Y_{max} can be obtained by substituting the maximum elongation of the joint (design value), the length of the pipe, the angle of the pipe bend, and the diameter into them.

6.3.3 Concept of thrust restraint during liquefaction

A concept diagram of thrust restraint during liquefaction is shown in **Figure 6.9**. The horizontal and vertical lines represent the thrust force and the allowable displacement, respectively. The important thing is that the force-displacement curve varies depending on the effective stress of the soil. For instance, even though the displacement of the pipe at the excess pore water pressure ratio of 0.0 is less than the allowable displacement, the displacement at the ratio of 0.6 exceeds the allowable one in this diagram. This means that it is necessary to take some countermeasures to increase the resistive force for keeping the displacement of the pipe within the allowable one when liquefaction occurs.

As shown in Eq. (6.7), the variation of the effective stress of the soil is reflected only by the effective unit weight of the soil. Thus, in case the resistive force becomes insufficient due to liquefaction (the pipe displaces a lot until sufficient resistive force is obtained), some countermeasures to increase the effective unit weight should be applied. By substituting the thrust force and the allowable displacement including the safety factor into Eq. (6.7), the effective unit weight for drawing a curve passing through the intersection *A* of two straight lines (see **Figure 6.9**) can be obtained. This thesis defines it as the minimum unit weight of

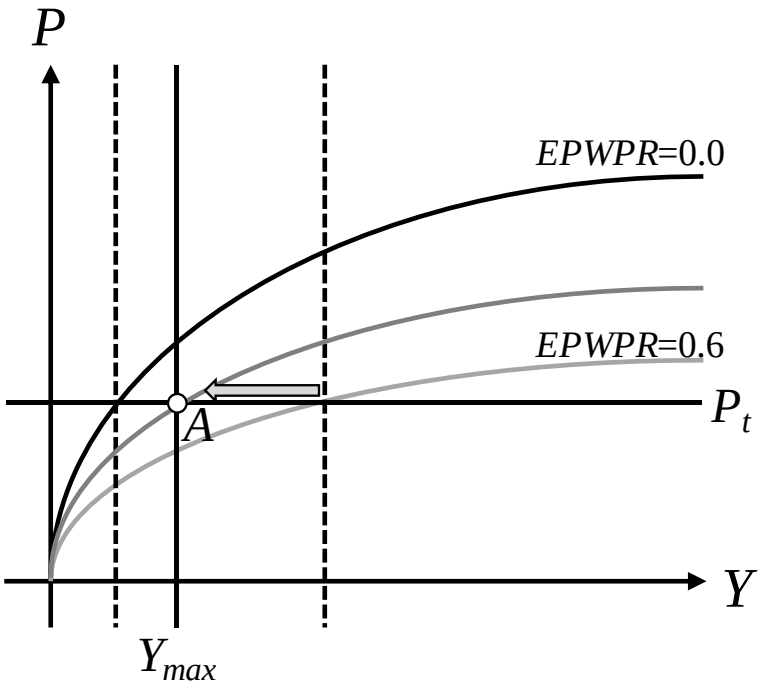

Figure 6.9 Relationship between thrust force and allowable displacement of pipe

the soil. This unit weight is a boundary for determining whether or not the degree of liquefaction of the ground is safe against the thrust force. In other words, when the larger effective unit weight that than the minimum unit weight is secured, the safety against the detachment of the joint is ensured.

To design more rationally, classifying the reduction rate of the effective stress of the soil according to the liquefaction potential. For instance, when the construction site mainly consists of clayey soil and the ground water level is sufficiently low, the liquefaction potential is extremely low and it is sufficiently safe to secure the minimum unit weight in the saturated condition. The present seismic design in the guideline for buried pipeline (M.A.F.F., 2009) shows a simple method using F_L value to determine the reduction rate D_E of the soil constants. F_L is a resistivity to liquefaction: when F_L is 1.0 or less, the soil has a sufficient potential of liquefaction. In the guideline, the constants of soil to be reduced are the following three: coefficient of subgrade reaction, upper limit of the ground reaction force, and maximum friction force. The range of F_L is classified into three levels of $F_L < 1/3$, $1/3 < F_L < 2/3$, and $2/3 < F_L < 1$ to determine each reduction rate. In a similar way, consider a method to verify the stability of buried pipelines against thrust force during liquefaction on the basis of the liquefaction potential as follows.

- $2/3 < F_L < 1$

Whether the effective unit weight at the excess pore water pressure ratio of 0.33 is larger than minimum unit weight.

- $1/3 < F_L < 2/3$

Whether the effective unit weight at the excess pore water pressure ratio of 0.66 is larger than minimum unit weight.

- $F_L < 1/3$

When the excess pore water pressure ratio is raised up to 1.0, the resistive force is calculated as zero since the effective unit weight of the soil is zero. Therefore, when liquefaction potential is very high, judgment concerning the minimum unit weight is carried out after several countermeasures are applied using gravel or installing geogrid.

6.3.4 Thrust restraint during liquefaction

Substitution of gravel

Chapter 4 revealed that the gravel substitution could suppress the rise of the excess pore water pressure during pipe movement. The dissipation effect of the excess pore water pressure depended on the width of the substitution range. The excess pore water pressure on the passive side of the pipe decreased greatly by widening its width to the passive side. Moreover, higher shear strength of the gravel was also added to the lateral resistive force. This section shows the design concept to reflect the above effects on the design.

In the design guideline, the standard excavation-width B_s is determined according to the diameter of the pipe. This width is not linear with the diameter, and is empirically determined for the purpose of securing sufficient workability. For instance, the standard excavation width of 500 mm in diameter is 1,600 mm (B_s/D = 3.2), the width of 1,000 mm in diameter is 2,200 mm (B_s/D = 2.2), and the width of 2,000 mm in diameter is 3,500 mm (B_s/D = 1.75). Unnecessary expansion of the excavation width undesirably increases the construction cost. When the width of the gravel is defined as B, the ratio of the width to the diameter B/D in the three experimental conditions in Chapter 4 is B/D = 2.0, 2.5, 3.0. Compared with the standard excavation width in the design, these substituting ranges of the gravel are reasonable.

Figure 6.10 shows the relationship between the horizontal distance (substitution width) from the side of the pipe and the reduction rate of the excess pore water pressure ratio. The width and the reduction rate is normalized by the diameter of the pipe and the excess pore water pressure measured when B is 0.0 mm (homogeneous sand), respectively. The graph shows that the excess pore water pressure ratio drops approximately linearly as the gravel width increases. A dissipation effect up to 30% can be expected. By substituting the standard excavation-width determined according to the diameter into the relationship of this approximate line, it is possible to calculate the reduction rate of the excess pore water pressure ratio F_R. This reduction rate is taken into account by multiplying the boundary values of the excess pore water pressure ratio: 0.33, 0.66, and 1.0 determined by F_L value.

Subsequently, the reinforcing effect by the shear strength of the gravel as shown in

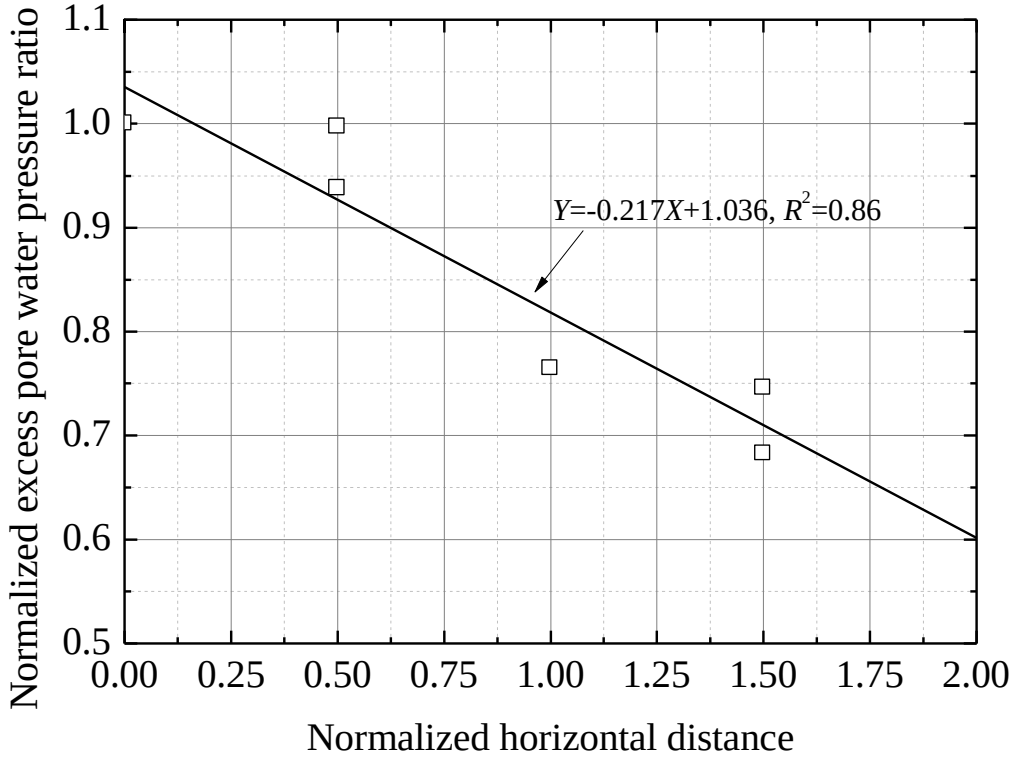

Figure 6.10 Relationship between normalized horizontal distance and reduction rate

Figure 4.24 is described. The ratio of the intercept of the straight lines showed that the shear reinforcing effect was approximately 12%. This is an effect to be reflected after the resistive force is calculated by correcting the effective unit weight. This effect is not reflected on the design because this acts on the safety side.

Integration effect by geogrid

As shown in Chapter 4, geogrid could integrate the gravel around the pipe due to constraining effect. The experimental results elucidated that its effect contributed to expand the pressure receiving area of the gravel in the vertical direction (see **Figure 4.26**). It was also revealed that the reinforcement effect by the geogrid did not depend on the effective stress of the soil and maintained a constant increase rate (see **Figure 4.29**). From the above experimental results, when reflecting the reinforcement effect by geogrid, the diameter of pipe D in Eq. (6.7) is simply extended according to the vertical height of the integrated range. Note that as the diameter extends, the depth of soil cover H' becomes shallow and the bearing capacity factor N_h also changes.

6.4 Calculation Example

6.4.1 Input parameter

On the basis of the proposed design flow, trial calculation is performed for a pipe with a diameter of 1,000 mm. The burial depth is 2.0*D*, and the unit weight of the soil and the internal friction angle is 20.0 kN/m^3 and 40^o, respectively. The bearing capacity factors of this condition is 8.0 that can be obtained from the chart in **Figure 6.5**. The internal water pressure is assumed to be 0.2 MPa, which is common as the water supply pressure of irrigation water, and the angle of the pipe bend is supposed to be 45^o. The thrust force is calculated from the internal water pressure, the angle of the pipe bend, and cross-sectional area of the pipe according to Eq. (4.1). The calculated thrust force is approximately 120 kN.

The allowable lateral displacement of the pipe bend is calculated from Eq. (6.10). The length of the straight pipe connected to the pipe bend is supposed to be 5,000 mm. The maximum elongation of the joint is set to 44 mm from the catalog value of FRPM pipe. The calculated allowable lateral displacement is 152 mm. In consideration of the safety factor of 1.5, this is modified as 101 mm. **Table 6.1** summarizes a list of calculation parameters.

6.4.2 Calculation result

The relationship between the displacement, the resistive force, and the effective unit weight under the above conditions is as follows:

$$P = \frac{20.0\gamma' \cdot Y}{\left(1 - \frac{\gamma'}{2.36 + 1.25\gamma'}\right)0.075 + \left(\frac{\gamma'}{2.68 + 1.22\gamma'}\right)Y} \tag{6.11}$$

Table 6.1 Parameters for calculation example

H: Burial depth (mm)	2,000	ϕ: Internal friction angle (^{o})	40
γ: Unit weight of soil (kN/m^3)	20.0	A_c: Water pressure (MPa)	0.2
L: Length of pipe (mm)	1,000	θ: Angle of pipe bend (^{o})	45
E_{max}: Maximum elongation of joint (mm)	44	N_h: Bearing capacity	8.0
Y_{max}: Allowable lateral displacement (mm)	152	P_t: Thrust force (kN)	120

Figure 6.11 shows the force-displacement curves for the excess pore water pressure ratio of 0.0, 0.2, 0.4, 0.6, and 0.8. The calculated thrust force and the allowable lateral displacement are shown as straight lines. The graph indicates that the displacement of the pipe due to the thrust force is within the allowable displacement until the excess pore water pressure is about 0.4. Subsequently, the stability of the pipeline against liquefaction is verified. Trial calculations are performed according to classified three-liquefaction potentials. The minimum unit weight of the soil calculated from both the thrust force and the allowable lateral displacement is 5.31 kN/m^3.

First, when the liquefaction potential is low (excess pore water pressure is 0.33), it is obvious from the graph that the lateral displacement is within the allowable displacement. Second, when the liquefaction potential is middle (excess pore water pressure is 0.66), the calculated effective unit weight is 3.47 kN/m^3, which is below the minimum unit weight. Therefore, the reduction rate of the excess pore water pressure ratio due to the gravel substitution is calculated. The reduction rate calculated according to the standard excavation-width is approximately 0.9. Although the effective unit weight recovers to 4.14

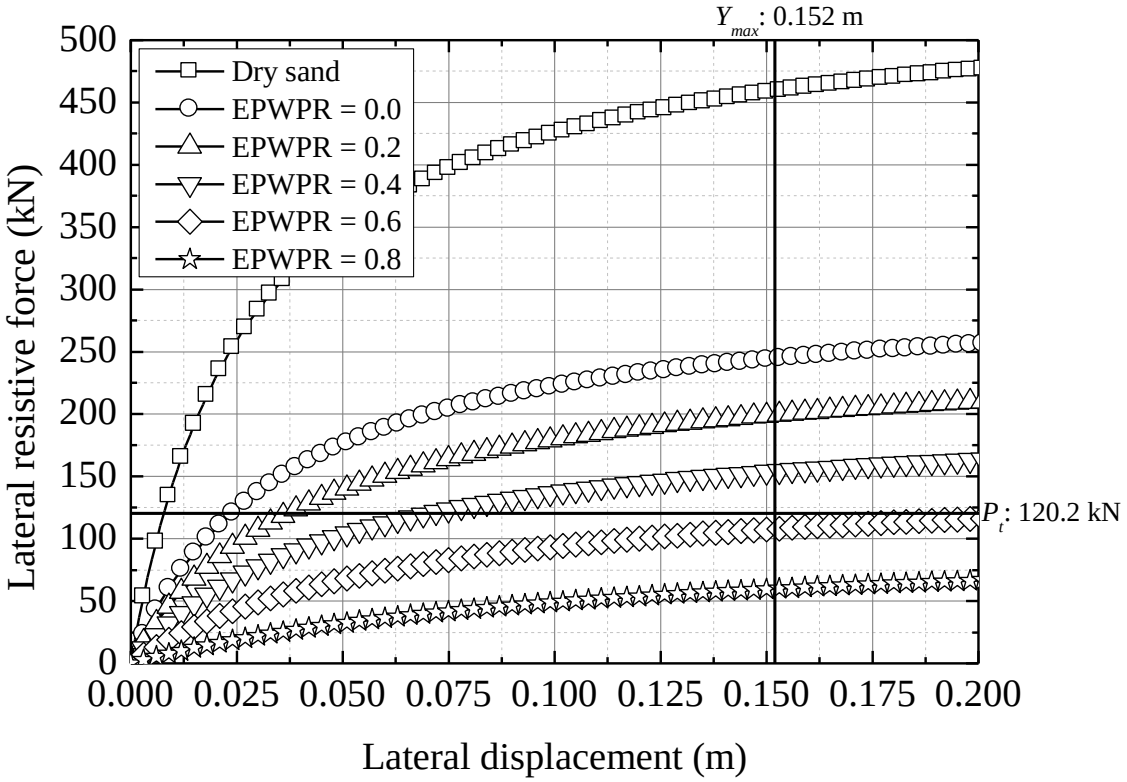

Figure 6.11 Calculation example: force-displacement curve (ϕ 1,000 mm)

kN/m^3, it is not sufficient. When the distance from the side of the pipe is extended to 1,500 mm, the effective unit weight recovers to 5.42 kN/m^3, which is slightly exceeds the minimum unit weight. Finally, when the liquefaction potential is high, the effective unit weight recovers only to 4.06kN/m^3, even if the gravel width is extended to 2,000 mm. Therefore, recalculation of the minimum effective unit weight is performed after applying the integration effect by the geogrid. Recalculating the diameter and N_h with integrated vertical height set to 2,000 mm results in a decrease in the minimum effective unit weight to 3.16 kN/m^3. Therefore, we can confirm that the corrected effective unit weight exceeds the minimum unit weight.

6.5 Conclusions

In this chapter, after formulating a force-displacement curve that took into account the variation of the effective stress based on hyperbolic approximation, more rational limit-state design method considering the variation of the effective stress was proposed. The following conclusions were made.

1. The normalized force-displacement curves showed hyperbolic relationships for each case under different hydraulic gradients. Differences between the curves, which were attributed to the initial effective stress of the soil, were reflected in the unit weight of the soil. The two coefficients of the hyperbolic curves also showed a hyperbolic dependence on the unit weight.
2. The ultimate lateral resistive force increased proportionally with the unit weight. It was also proportional to the depth of soil cover because of the increase in the confining pressure of the soil bed.
3. The bearing capacity factors calculated from the ultimate resistive force were in very good agreement with the theoretical factors. By substituting the bearing capacity factors, a force-displacement relationship was formulated that took into account the variation of the unit weight of the soil depending on the excess pore water pressure ratio, the depth of soil cover, the diameter and the length of the pipe.
4. The design flow based on the limit-state design was proposed. The allowable displacement was calculated from the maximum elongation of each joint. This

displacement was compared with the lateral displacement obtained by substituting the thrust force into the force-displacement curve determined from the backfilling condition, and the necessity of the installation of the countermeasure was judged.

5. Subsequently, the pipeline stability considering the reduction of the resistive force due to liquefaction was verified according to the liquefaction potential of the soil. The displacement of the pipe was judged based on the minimum unit weight of the soil calculated from the thrust force and the allowable displacement. When the sufficient effective unit weight of the soil was not satisfied, the thrust restraint using gravel or geogrid was applied.

References

Audibert, J. M. E. and Nyman, K. J. 1977. Soil Restraint against Horizontal Motion of Pipes, *Journal of the Geotechnical Engineering Division*, **103**(10), 1119-1142.

Hansen, J. B. 1961. The Ultimate Resistance of Rigid Piles against Transversal Forces, *Bulletin 12*, Danish Geotechnical Institute, Copenhagen, Denmark, 5-9.

Itani, Y., Fujita, N., Yokota, Y., Ariyoshi, M., Mohri, Y., and Kawabata, T. 2015. Mechanical Behavior of Flexibly Jointed Pipeline with a Bend on Lateral Loading Tests, *IDRE Journal*, **83**(6), 177-183. (in Japanese with English summary).

Itani, Y., Fujita, N., Ariyoshi, M., Mohri, Y., and Kawabata, T. 2016. Dynamic Behavior of Flexibly Jointed Pipeline with a Bend in Liquefied Ground, *IDRE Journal*, **84**(1), 1-8. (in Japanese with English summary).

Ministry of Agriculture, Forestry and Fisheries of Japan (MAFF). 2009. Planning and Design Criteria of Land Improvement Project (Pipeline), JSIDRE, 356-361. (in Japanese).

Mohri, Y., Yasunaka, M., and Tani, S. 1995. Damage to Buried Pipeline due to Liquefaction Induced Performance at the Ground by the Hokkaido-Nansei-Oki Earthquake in 1993, *Proceedings of 1st International Conference on Earthquake Geotechnical Engineering*, IS-Tokyo, 31-36.

Ovesen, N. K. 1964. Anchor Slab, Calculation Methods and Model Tests, *Bulletin 16*, Danish Geotechnical Institute, Copenhagen, Denmark, 5-39.

Suzuki, N., Yano, T., and Matsuyama, E. 1993. Deformation of buried pipeline subjected to lateral displacement of liquefied soil, *Proceedings of the JSCE Earthquake Engineering Symposium*, **22**, 663-666. (in Japanese)

Trautmann, C. H. and O'Rourke, T. D. 1985. Lateral Force-Displacement Response of Buried Pipe, *Journal of the Geotechnical Engineering*, **111**(9), 1077-1092.

CHAPTER 7

Chapter 7

Conclusions and Perspectives

7.1 Introduction

The aim of the present study was to elucidate lateral displacement characteristics of buried pipeline during liquefaction considering interaction with surrounding soil and to propose a rational design method. To accomplish the aim of the study, this thesis focused on following issues:

1. Displacement characteristic of buried pipe under various effective stress conditions
2. Prediction of lateral displacement of buried pipe subjected to external force
3. Effectiveness of thrust restraint during liquefaction

The above issues were addressed by means of lateral loading experiments and two-dimensional simulation using fluid coupled-DEM. This chapter reviews the conclusions of each chapter and shows the perspectives.

7.2 Conclusions

Chapter 3 described the small-scale model experiments for a model pipe to examine the lateral displacement characteristic of the buried pipe when the effective stress of the soil decreased due to liquefaction. The model pipe was pulled laterally under displacement control in the saturated sand bed where the effective stress was adjusted by the upward seepage. The experimental results indicated that the lateral resistive force decreased almost linearly as the excess pore water pressure ratio increased.

From the experiments under various lateral loading rate, the rate dependence on the

lateral resistive force was investigated. In the saturated sand, the excess pore water pressure on the passive side of the pipe raised rapidly due to the pipe movement and the resistive force decreased. The excess pore water pressure reached upper limit when exceeding the certain loading rate, and its upper limit roughly agreed with the initial effective stress of the soil bed. In other word, the possibility that the saturated sand temporarily liquefied by the movement of the pipe was shown.

Chapter 4 treated the lateral loading experiments in a larger scale. In this experiment, the lateral loading was applied to the model pipe under either displacement or load control. Comparison of the experimental results indicated that the relationship between the effective stress of the soil bed, the lateral displacement, and the lateral resistive force does not depend on the control method of the lateral loading. The moving vector of the sand particles calculated by PIV analysis visually clarified the movement characteristics of the passive-side soil against the lateral displacement of the buried pipe. The variation of the resistive force depended on the two deformation mechanisms: compression and shear, and the moving vector showed the fluid-like behavior of the soil when the effective stress was low.

The effectiveness of the liquefaction countermeasure using gravel and the thrust restraint using geogrid were experimentally verified. By partially substituting the backfill by the gravel, the increase in the excess pore water pressure during the displacement of the pipe was suppressed, and the lateral resistive force increased. The PIV results clarified the integrating effect by the geogrid, the lateral resistive force was increased even when the excess pore water pressure ratio was high.

In Chapter 5, two-dimensional simulation of the lateral loading experiments was carried out using a fluid coupled-DEM analysis. The interaction between soil and pore water was reproduced by dividing the model into solid and fluid phases. The variation of the excess pore water pressure was calculated on a fluid mesh based on the pore volume change, and was then given to the soil particles in the solid phase. Liquefaction was reproduced by the decrease of the contact force between the soil particles due to the upward seepage induced by the head difference between the fluid meshes.

The force-displacement curves obtained from the lateral loading simulation carried out in the soil bed with reduced contact force showed very good agreement with the

experimental results. The deformation mechanism of the soil bed due to the pipe movement was clarified from the distribution diagrams of the contact force and the movement of the soil particles. The horizontal earth pressure acting on the pipe during lateral displacement showed approximately a convex distribution that largely differed from a trapezoidal distribution proposed in the current design guideline. The variation of the void ratio and the excess pore water pressure with the pipe displacement could be reproduced to some extent, and the applicability of this analysis method to interaction problems has been verified.

In Chapter 6, the relationships between the lateral displacement and the resistive force obtained from the model experiments was formulated by hyperbolic approximation. The ultimate resistive force could be calculated using both the bearing capacity factor proposed in the past study and the effective unit weight of the soil considering the excess pore water pressure. A force-displacement curve that took into account the variation of the effective stress was formulated. Furthermore, limit-state design method considering the relation with the thrust force and the variation of the effective stress was proposed based on the force-displacement curve.

7.3 Perspectives

Scale effect

It is well known that the behavior of underground structures depends on the restraint pressure of soil. Although several model experiments were conducted in the present study, any size is quite small compared to the actual size. In Chapter 6, the force-displacement relationship was formulated considering the influence of the diameter of the pipe and the burial depth. However, it is unknown whether it really fits the actual burial condition. As an experiment to consider the scale effect, centrifuge modeling is desirable. By performing a similar experiment in the centrifugal field, the stress level of the target scale is reproduced and the influence of the scale effect can be verified.

Dissipation effect of excess pore water pressure by gravel

In the present study, the effective stress of the soil bed was decreased by boiling

using the upward seepage, and liquefaction was experimentally reproduced. Regarding the liquefaction countermeasure using gravel, although the dissipation effect of the excess pore water pressure could be confirmed, examination only by this method is not sufficient for the following reasons. First, in general, the excess pore water pressure immediately rises during earthquake. There is a big difference from the actual phenomenon because the excess pore water pressure ratio increases gradually increased in the present method using upward seepage. Since liquefaction is reproduce over a long period of time, the instantaneous dissipation of the excess pore water pressure could not be obtained, and it seems to be underestimating the dissipation effect. The concentrated flow of the upward seepage toward the gravel area was also observed due to the gradual increase of the excess pore water pressure.

In order to verify whether the above phenomenon can actually occur, shaking table tests are suitable. By applying the seismic wave to the experimental model, it is possible to observe the variation of the excess pore water pressure on the actual time scale. Combination with the centrifuge modeling described above are more suitable.

Design for thrust restraint during liquefaction

The design method considering liquefaction proposed in this thesis is based on many assumptions. In addition to the scale effect, the difference of the soil material, soil density, or the stiffness of the pipe have not been examined. In addition to conducting additional experiments, field tests is crucial to reflect the findings on practical design. It is necessary to solve issues related to workability and economy through field tests.